

UNIVERSITY OF BLIDA 1

Institute of Aeronautics and Space Studies

DOCTORAL THESIS

(Aeronautics)

Specialty: Aeronautics

DYNAMIC PROPERTIES ESTIMATION OF A WEATHER RADAR SIGNAL USING RECENT SPECTRAL APPROACHES

By

TIKHEMIRINE Mohamed

Doctoral committee:

A. GUESSOUM	Professor, University of Blida 1	Chairman
M. LAGHA	Professor, University of Blida 1	Adviser
S. BERGHEUL	Professor, University of Blida 1	Co-Adviser
A. ADANE	Professor, USTHB, Alger	Reviewer
D. BERKANI	Professor, ENP, Alger	Reviewer
K. SCHNEIDER	Professor, Univ. Aix Marseille/ France	Reviewer

Blida, 2016

ملخص

أساليب مختلفة لتقدير طيف دوبلر، من أجل الحصول على معلمات الطقس والميزات أقرب ممكن للمعلومات الحقيقية، قد تم فحصها ومناقشتها.

ويستند هذا المبدأ على إزالة أي شوائب في إشارة الرادار. وقد تم تصميم أسلوب الكلاسيكية الأكثر شهرة من قبل الثنائي هيلدبراند وسيخون لإزالة الضوضاء لطيف دوبلر. في هذا العمل، يتم استخدام تحويل الموجات على أساس رفع خطة المرتبطة بتكيف العتبة. ويتم مقارنة ما بين الإجراءين، واتضح أن تحويل الموجات على أساس رفع خطة المرتبطة بتكيف العتبة يتفوق أسلوب الكلاسيكية.

RESUME

Des méthodes variées pour l'estimation du spectre Doppler, dans le but d'obtenir des paramètres météorologiques les plus proches possibles des vrais, ont été examinées et discutées.

Le principe est basé sur l'extraction de toute impureté du signal radar. La méthode classique connue est conçue par le duo Hildebrand et Sekhon. Dans ce travail, la méthode de la transformée en ondelettes basée sur les schémas de lifting associée à un seuillage adaptif est utilisée.

Une comparaison est réalisée entre les deux procédures et il s'est avéré que la méthode de la transformée en ondelettes basée sur les schémas de lifting associée à un seuillage adaptif suclasse la procédure classique.

ABSTRACT

Various methods for Doppler spectrum estimation, in order to obtain weather parameters and features as close as possible to the true ones have been examined and discussed.

The principle is based on removing any impurity in the radar signal. The most known classical method was designed by the duo Hildebrand and Sekhon to denoise Doppler spectrum. In this work, the lifting scheme based wavelet transform and adaptive threshold is proposed and implemented.

A comparison is carried out between the two procedures and it turned out that the lifting scheme based wavelet transform method associated with an adaptive thresholding outperforms the classical one.

ACKNOWLEDGEMENT

First, I would like to express my thanks to my supervisor Dr. M. Lagha for constance in encouraging and guiding me through this thesis.

I am sincerely grateful of Dr. Robert D. Palmer and Tian-you Yu who accepted me as an Exchange Student in their Advanced Radar Research Center (ARRC), in the University of Oklahoma, where they both gave me valuable guidance and allowed me to use their facilities for my research.

Finally, I would like to express my gratitude and love to my family who encouraged and supported me in these last and long years of doctorate.

Table of Contents

Chapter 1 : Introduction.....	1
1.1. Motivation.....	1
1.2. Literature review of weather radar signal processing.....	2
1.3. Scope of this thesis.....	5
Chapter 2 :Fundamentals of weather radar.....	6
2.1. Introduction.....	6
2.1.1. Frequencies and wavelengths.....	6
2.1.2. Antenna.....	7
2.1.3. Transmitter.....	7
2.1.4. Transmission.....	7
2.1.5. Reception.....	8
2.1.6. Duty cycle.....	8
2.1.7. Pulse volume.....	8
2.1.8. Receiver.....	8
2.2. Doppler weather radar.....	9
2.2.1. Doppler effect.....	10
2.2.2. Phase shift.....	10
2.2.3. Radial velocity.....	11
2.2.4. Ambiguous velocity.....	11
2.2.5. Doppler dilemma.....	11
2.3. Doppler weather radar products.....	12
2.4. Weather radar equations.....	13
2.4.1. Equivalent radar reflectivity.....	15
2.4.2. Radar equation.....	16
2.5. Signal processing.....	17
2.6. Statistical parameter estimation.....	19
2.6.1. Estimation of received mean power.....	22
2.7. Dual polarization Doppler weather radar.....	23
Chapter 3 :Doppler weather radar signal processing.....	25
3.1. Introduction.....	25
3.2. Base data estimation.....	26
3.2.1. Time domain estimators.....	27
3.2.1.1.Signal power.....	27
3.2.1.2.Mean Doppler velocity.....	27
3.2.1.3.Spectrum width.....	28
3.2.2. Frequency domain estimators.....	29
3.2.2.1.Windowing effects on spectrum estimation.....	29
3.2.2.2.Mean Doppler Velocity.....	31
3.2.2.3.Spectrum width.....	31
3.2.3. Enhancing spectra estimators performance.....	32

3.2.3.1. Autoregressive Modeling.....	32
3.2.3.2. ARMA modeling.....	35
3.2.4. Artifacts removal.....	37
3.2.4.1. Noise removal.....	37
3.2.4.2. Ground clutter removal.....	38
Chapter 4 :Lifting-based wavelet transform in Doppler spectrum estimation.....	40
4.1. Introduction.....	40
4.1.1. Example.....	46
4.2. Motivation.....	48
4.3. Wavelet choice.....	49
4.4. Thresholding strategy choice.....	50
4.4.1. Minimax threshold.....	50
4.4.2. Universal threshold.....	51
4.4.3. SURE threshold.....	51
4.4.4. Hard thresholding.....	52
4.4.5. Soft thresholding.....	52
4.4.6. Other thresholds.....	52
4.5. Algorithm for spectrum estimation.....	53
4.5.1. Spectral moments dependence with noise.....	54
4.5.2. Procedure course.....	55
4.6. Case study.....	57
4.6.1. Available sources.....	57
4.6.2. Synthetic data.....	58
4.6.3. Real data.....	60
Chapter 5 :Results and comments.....	62
5.1. Synthetic signals.....	62
5.1.1. Generation of weather sequences.....	62
5.1.2. Statistical properties of weather sequences.....	64
5.1.3. Denoising using lifted wavelets and optimum threshold.....	65
5.1.4. Denoising using Hildebrand and Sekhon algorithm.....	69
5.1.5. Comparison.....	73
5.2. Actual data.....	77
5.2.1. Representation of weather sequences.....	77
5.2.2. Statistical properties of real radar signals.....	80
5.2.3. Denoising using lifted wavelets and optimum threshold.....	82
5.2.4. Global view of real data.....	85
Chapter 6 :Conclusion and recommendations for future work.....	90
6.1. Summary and conclusions.....	90
6.2. Recommendation for future work.....	92

Index of Tables

Table 2.1 Summary of operational radar frequencies. S, C and X bands are commonly used by operational ground based weather radars.....	7
Table 2.2 Reflectivity span in correspondence to the type of precipitation.....	17
Table 2.3 Differential reflectivity (Z_{DR}) is a good indicator of the mean drop shape of the dominant hydrometeor within the resolution volume.....	24
Table 4.1: Technical specifications of the weather phased array radar testbed located in Norman (Oklahoma, USA).....	58

Illustration Index

Figure 2.1: Illustration of the Doppler dilemma for a frequency.....	13
Figure 2.2: Volume resolution at range r.....	15
Figure 2.3: Doppler spectrum depicting the received power from a simulated weather perturbation, the mean radial velocity and spectral width of velocity.....	18
Figure 2.4: Set of random particles for which the instantaneous positions are described by vectors relative to the radar.....	21
Figure 2.5: The resultant phasor is where I refers to the in-phase component and Q refers to the quadrature-phase component.....	22
Figure 3.1: Typical windows behavior in the spectral domain. The rectangular window has the narrowest main lobe and the Blackman window has the lowest side lobes. The Von Hann window is the best bargain between the three windows.....	30
Figure 4.1: Discrete wavelet transform (one level).....	41
Figure 4.2: Wavelet transform via lifting scheme.....	42
Figure 4.3: Inverse wavelet transform via lifting scheme.....	43
Figure 4.4: DWT: (Low pass) and (High pass) are the analysis filters of the forward transform; (Low pass) and (High pass) are the synthesis filters of the inverse transform.....	44
Figure 4.5: Forward wavelet transform using lifting scheme.....	45
Figure 4.6: Inverse wavelet transform using lifting scheme.....	46
Figure 4.7: Inverse wavelet transform through lifting scheme using D4 wavelet.....	47
Figure 4.8: Forward wavelet transform through lifting scheme using D4 wavelet.....	47
Figure 4.9: Computational complexity vs number of samples: Lifted wavelet transform is faster than DWT and FFT.....	49
Figure 4.10: Output of hard and soft thresholds nonlinearities.....	53
Figure 4.11: Evolution of radial velocity estimate and spectrum width estimate with noise level. In the present case, true radial velocity is 4 m/s and true spectrum width is 2m/s.....	55
Figure 4.12: First step of weather radar spectrum denoising using lifted wavelet transform.....	57
Figure 4.13: Second step of weather radar spectrum denoising using lifted wavelet transform.....	58
Figure 4.14: Signal features distributions: a) Rayleigh distribution for amplitude. b) Uniform distribution for phase. c) Exponential distribution for power.....	61
Figure 5.1: Simulated time series of 40 samples and the corresponding spectrum for , and	63
Figure 5.2: Simulated time series of 40 samples and the corresponding spectrum for , and	63
Figure 5.3: Simulated time series of 40 samples and the corresponding spectrum for , and	64
Figure 5.4: Bimodal signal composed of weather centered at 10 m/s and ground clutter centered at zero Doppler. The red curve (Bottom) depicts the ideal spectrum whereas the blue curve is the actual spectrum.....	64
Figure 5.5: Statistical properties of a simulated sequence.....	65
Figure 5.6: Scatter plot of quadratic-phase vs in-phase of a simulated weather sequence.....	66
Figure 5.7: Doppler Radial velocity: Denoising of simulated signals (throughout Nyquist interval) for , , using the standard LWT in green and the proposed algorithm in red.....	67
Figure 5.8: Spectrum width: Denoising of simulated signals (throughout Nyquist interval) for , , using the standard LWT in green and the proposed algorithm in red.....	67
Figure 5.9: Doppler Radial velocity: Denoising of simulated signals (throughout Nyquist interval) for , , using the standard LWT in green and the proposed algorithm in red.....	68
Figure 5.10: Spectrum width: Denoising of simulated signals (throughout Nyquist interval) for , , us-	

ing the standard LWT in green and the proposed algorithm in red.....	68
Figure 5.11: Doppler Radial velocity: Denoising of simulated signals (throughout Nyquist interval) for , , using the standard LWT in green and the proposed algorithm in red.....	69
Figure 5.12: Spectrum width: Denoising of simulated signals (throughout Nyquist interval) for , , using the standard LWT in green and the proposed algorithm in red.....	69
Figure 5.13: Hildebrand & Sekhon algorithm performance.....	70
Figure 5.14: Doppler Radial velocity: Denoising of simulated signals (throughout Nyquist interval) for , , using the Hildebrand & Sekhon algorithm in red.....	71
Figure 5.15: Spectrum width: Denoising of simulated signals (throughout Nyquist interval) for , , using the Hildebrand & Sekhon algorithm in red.....	71
Figure 5.16: Doppler Radial velocity: Denoising of simulated signals (throughout Nyquist interval) for , , using the Hildebrand & Sekhon algorithm in red.....	72
Figure 5.17: Spectrum width: Denoising of simulated signals (throughout Nyquist interval) for , , using the Hildebrand & Sekhon algorithm in red.....	72
Figure 5.18: Doppler Radial velocity: Denoising of simulated signals (throughout Nyquist interval) for , , using the Hildebrand & Sekhon algorithm in red.....	73
Figure 5.19: Spectrum width: Denoising of simulated signals (throughout Nyquist interval) for , , using the Hildebrand & Sekhon algorithm in red.....	73
Figure 5.20: Doppler Radial velocity: Comparison in denoising of simulated signals (throughout Nyquist interval) for , , using the proposed algorithm in red and the Hildebrand & Sekhon algorithm in green.....	74
Figure 5.21: Spectrum width: Comparison in denoising of simulated signals (throughout Nyquist interval) for , , using the proposed algorithm in red and the Hildebrand & Sekhon algorithm in green.....	74
Figure 5.22: Doppler Radial velocity: Comparison in denoising of simulated signals (throughout Nyquist interval) for , , using the proposed algorithm in red and the Hildebrand & Sekhon algorithm in green.....	75
Figure 5.23: Spectrum width: Comparison in denoising of simulated signals (throughout Nyquist interval) for , , using the proposed algorithm in red and the Hildebrand & Sekhon algorithm in green.....	76
Figure 5.24: Doppler Radial velocity: Comparison in denoising of simulated signals (throughout Nyquist interval) for , , using the proposed algorithm in red and the Hildebrand & Sekhon algorithm in green.....	76
Figure 5.25: Spectrum width: Comparison in denoising of simulated signals (throughout Nyquist interval) for , , using the proposed algorithm in red and the Hildebrand & Sekhon algorithm in green.....	77
Figure 5.26: Time series: Real radar signal corresponding to range cell #380 from the radial #109.....	78
Figure 5.27: Spectrum of time series: Real radar signal corresponding to range cell #380 from the radial #109.....	78
Figure 5.28: Time series: Real radar signal corresponding to range cell #432 from the radial #109.....	79
Figure 5.29: Spectrum of time series: Real radar signal corresponding to range cell #432 from the radial #109.....	79
Figure 5.30: Spectrum of time series: Real radar signal corresponding to range cell #432 from the radial #109.....	80
Figure 5.31: Real phased array radar signal and the corresponding spectrum (Range bin #380 from radial #109).....	81
Figure 5.32: Scatter plot of a real signal corresponding to range bin #380 from radial #109.....	81
Figure 5.33: Statistical properties of a selected range bin sequence from the radial #109.....	82
Figure 5.34: Performance of the proposed algorithm on real data to estimate the spectrum, radial Doppler velocity and spectrum width of the range bin #380 (radial #109).....	83
Figure 5.35: Performance of the proposed algorithm on real data to estimate the radial Doppler velocity from range bin #70 to range bin #249.....	84
Figure 5.36: Performance of the proposed algorithm on real data to estimate the corresponding spectrum width from range bin #70 to range bin #249.....	84
Figure 5.37: Performance of the proposed algorithm on real data to estimate the radial Doppler ve-	

locity from range bin #350 to range bin #549.....	85
Figure 5.38: Performance of the proposed algorithm on real data to estimate the corresponding spectrum width from range bin #350 to range bin #549.....	85
Figure 5.39: Sectorial view of real data from the phased array weather radar located in Norman, OK (USA).....	86
Figure 5.40: Filtered real data from the phased array weather radar located in Norman, OK (USA).	86
Figure 5.41: Location of the phased array radar (Norman, OK) relatively to the WSR-88D KTLX radar (S.W. of Oklahoma City).....	87
Figure 5.42: View of the same weather perturbation by KTLX radar.....	88
Figure 5.43: Gridded and labeled view of the sector corresponding to the phased array radar sight for the storm.....	88
Figure 5.44: Reconstruction of the shade of the storm in conjunction of Google Earth and NOAA Weather and Climate Toolkit.....	89
Figure 6.1: Biorthogonal 9/7 wavelet: Decomposition wavelet and its scaling function and their corresponding filters (Top). Reconstruction wavelet and its scaling function and their corresponding filters (Bottom).....	98

Chapter 1 : Introduction

1.1. Motivation

Weather radar plays a vital role in improving early severe storm detection and warning [1]. Weather radar can provide important information such as rainfall, snow and hail rates as well as wind shear and tornadoes with high temporal and spatial resolutions over a large area including those region where a weather station can not be built or can't get access to (because of high and steep mountains).

Research on weather radar systems and technologies is dictated by the society's need to improve the prediction quality (lead time warning, accuracy,...) of weather events. Research is oriented according to the inherent capabilities (whether there is Doppler function? Polarimetry? Phased array antenna?...) of the available weather radar system.

Furthermore, with the precious help of the new radar systems, research is focussing on understanding weather phenomena. This is the case of the dual polarization (dual-pol) weather radar providing very significant and more accurate information on classification of precipitation types as well as on precipitation rates.

These new radar systems can also help saving human lives. This is the case of rapid scanning radars (Phased array radars) which improve detection and forecast of fast weather phenomena such as thunderstorms, downbursts and tornadoes that can take lives in a few minutes. Conventional systems, rotating mechanically are inherently limited by the huge spinning dish at relatively low scan rates.

With the advent of low cost electronic components and powerful computing systems, it became possible to use algorithms and approaches that used to be impractical to implement in the past. Several algorithms and works in advanced signal processing

have been designed for these emerging radar technologies.

Indeed, research and development is continuously performing to improve data quality and explore new radar applications, new information and new capabilities. Using Doppler weather radar, we could estimate spectral moments that are reflectivity (Z_e), mean radial velocity (V_r), and spectrum width (σ_v) that are considered base data. Recently, radar systems are provided with dual polarization capability in weather applications. This new capability allow detection of new weather information. In addition to base data, polarimetric (dual-pol) weather radar can also provide polarimetric variables including differential reflectivity (Z_{DR}), cross correlation coefficient at lag zero ($\rho(0)_{HV}$), differential phase (Φ_{DP}). For some system, the linear depolarization ratio (LDR) is also available.

Moreover, currently, spectral processing is one of the important parts in weather radar signal processing [2]. As a reason, spectral processing helps improving accuracy and sensitivity of meteorological information.

More recently, spectral polarimetry (some authors refer to it by Doppler polarimetry [3][4][5]) has been added in the field of advanced signal processing. It was developed to combine Doppler and polarimetric measurements to consider polarimetric variables as a function of Doppler velocity within a range bin using spectral processing. This is used in order to improve data quality and gain more knowledge about the microphysics of precipitations.

1.2. Literature review of weather radar signal processing

The bulk of recent work on weather radar spectral processing focusing on parameter estimation such as the base data (first three spectral moments) or polarimetric variables (obtained with a polarimetric radar), or designing techniques and algorithms to identify and remove noise and clutter from received signals in order to enhance data quality or to gain more information about the microphysics of precipitation or obtain some more information about the environment such as turbulence, is achieved in spectral domain and therefore based on spectrum estimation.

The main reason to choose spectral approaches is to gain more accuracy in estimates. This is known since ever but the other reason that has contributed to this option is the processing power which is in constant increase for lower cost.

As a statistical inference problem, the estimation of spectral moments can be classified as parametric or nonparametric approach.

Spectrum estimation of a stochastic process is typically performed using the Fast Fourier Transform (FFT) [6]. This procedure to spectrum analysis produces reasonable results for a large number of signal types and processes. Despite of its advantages, the FFT approach has several performance limitations. Due to the huge variety of spectra, that one can find in practical applications, estimates are usually designed for a restricted subclass of spectra and consequently can show poor performance in other classes [7]. The prominent assumption for this technique is that all the useful information is contained in the data window, which is unrealistic.

For the current approach, indeed, the FFT presents a prominent limitation in frequency resolution [6][8][9] especially when the data set is short. In weather radar application, the limited number of samples corresponding to the number of pulses may cause leakage of power from stronger frequencies to weaker ones. Particularly when clutter power is very strong, its power leakage may overwhelm the weather signal and thus bias the weather spectrum estimate [8].

A second limitation is due to the implicit windowing of the data while executing the FFT. The application of tapered windows skillfully selected can greatly reduce the power leakage when power spectrum is being estimated [6][8] knowing that a window function may smear and broaden the spectrum. We need to consider the tradeoff between side lobe level and spectrum broadness.

In order to alleviate the inherent limitations to the FFT approach, which is classified as a nonparametric fashion, several alternative spectral estimation methods have been designed. Some of them have already been implemented and are operational on real weather radar applications.

By modeling the random process in a parametric way, we may obtain better spectral estimates with lower uncertainty than those obtained by nonparametric procedures [10][9][11]. The reason is that parametric methods don't assume that the process is zero outside the length of the data set. This removes the smearing effect of the spectrum caused by the window in nonparametric ones.

The major drawback of parametric approaches is that they have higher complexity and therefore, they need more computational resources than nonparametric ones.

Moreover, selecting parameters of a model so as the parameterized model can fit the true spectrum with accuracy is another issue [11][10].

A newer alternative method is gaining terrain in signal processing field. It is based on wavelets. Several works have attempted to solve the spectrum estimation problem

using different wavelets techniques [12][13][14][7].

Wavelet techniques applied to spectra estimation are smoothing spectra techniques by the use of skillful choice of threshold to apply on the empirical wavelet coefficients. The procedure consists of four basic steps.

1. Calculation of the periodogram of the given raw signal.
2. Decomposition: Apply a discrete wavelet transform (DWT) out to a specified level J_0 .
3. Threshold processing: Apply a thresholding procedure to the empirical wavelet coefficients.
4. Reconstruction: Invert the DWT to produce a smoothed estimate of the periodogram representing the spectrum.

The last step is common to all the different works that have been done. Some authors decide to deal with the periodogram [15][16] while others act on log periodogram [14][13] and multitaper estimators [7].

Technically, the second step of the procedure can be applied to a level $J_0 > 1$ only if the data set is many times longer than the filter (wavelet) length. Weather radar signals are typically short. They range from 40 samples or less, if the weather perturbation is fast, to 128 samples if the weather event is slower, in a horizontal sweeping.

In the case of atmospheric radar applications (wind profilers), signal can be very long and therefore, one can apply a multilevel DWT.

In more recent works, instead of using the classical DWT, we can find the lifting-based wavelet transform (LWT) as in [17][15].

The third step is the widest area for research where strategies of thresholding can vary from the simplest ones (soft or hard) to complicated ones as in [18] (p.561). Indeed, Mallat has shown that we can apply a thresholding strategy between the soft one and the hard one called diagonal attenuation function.

Moreover, many classical thresholds can be applied to the empirical wavelet coefficients containing noise components. In 1994, Donoho and Johnstone [19] proposed a universal threshold where the risk of thresholding, no matter soft or hard, is small enough to satisfy the requirements of most applications. The duo also proposed in 1998 [20] the minimax threshold such that the maximal risk of the estimator is minimal among all estimators.

1.3. Scope of this thesis

Globally, this work deals with various spectral methods in use with spectra estimation and spectral moment estimation leading to enhance the quality of weather radar products helping weather forecast operators to better interpret current weather conditions shown on their screen.

Chapter 2 is devoted to fundamentals of weather radar. In the first section, common features of radars are introduced. The next sections are related to Doppler weather radar specific features like mean radial velocity, Doppler dilemma between maximum velocity and maximum range resolved without ambiguity, output products. It also deals with the specific weather radar equation, signal processing and statistical parameter estimation. The last section of the chapter is an outline on dual polarization weather radar and its commonly used variables.

Chapter 3 is about base data estimation in both time and frequency domains using classical methods, in the first section. In the next section, enhancing spectra estimation methods are presented and discussed (AR and ARMA modeling). In the last section, noise and ground clutter removal is examined.

Chapter 4 is devoted to the contribution of this work in Doppler spectrum estimation based on lifted wavelet transform associated with an adaptive threshold (LWT-AT). Motivation, wavelet choice and non-linear functions for thresholding are discussed in detail. The proposed algorithm is examined and followed by a case study to test the performance using synthetic and real data.

In chapter 5, synthetic data are generated. Both synthetic and real data have been analyzed and results have been discussed. Circumstances of the selected real data are presented. A comparison between performances of lifting-based wavelet transform algorithm and Hildebrand & Sekhon procedure is presented.

In chapter 6, a summary of this work is presented and future work is proposed.

Chapter 2 : Fundamentals of weather radar

2.1. Introduction

With the advent of technological advances, the current features of the Doppler weather radar, like the US Weather Surveillance Radar (WSR-88D), far exceed those of the oldest Doppler systems. These features include a better velocity detection, greater power and sensitivity, and integration of advanced computers. This automation provides forecasters a wealth of information. The WSR-88D radar not only detects motions and target velocity, but also may consider internal storm circulations as well as detecting atmospheric motions in clear air. The WSR-88D excels in detecting severe weather events, and more importantly, increased advance-warning time.

2.1.1. Frequencies and wavelengths

Weather radars use the frequency bands S, C and X.

The S-band radars signals are not easily attenuated. For this, they are used for near and far meteorological observations. The disadvantage of this type of radars is that they require large antennas (over 8m diameter). They also require a large transmission power (> 750 kW).

C-band radars are more easily attenuated than the previous ones. They are used for meteorological observations at short distances. They do not require larger antennas than those of S-band radars. The required power is up to 270 KW.

As for the X-band radars, they are used for meteorological observations at shorter distances. They are used to detect very small water particles in clouds. They are also used in airborne applications.

The following table shows the different frequency bands of electromagnetic signals that can be used by radars.

Band	Frequency (f)	Wavelength (λ)	Maximum observable range
S	2 – 4 GHz	8 – 15 cm	At least 200 km
C	4 – 8 GHz	4 – 8 cm	Around 200 km
X	8 – 12 GHz	2.5 – 4 cm	Around 60 km
Ku	12 – 18 GHz	1.7 – 2.5 cm	Satellite-borne
Ka	27 – 40 GHz	.75 – 1.2 cm	Around 30 km
W	40 – 300 GHz	1 – 7.5 mm	Around 10 km

Table 1 Summary of operational radar frequencies. S, C and X bands are commonly used by operational ground based weather radars.

2.1.2. Antenna

Typically, the radar is monostatic: the same antenna is used for both transmitting and receiving signals. It can be a parabolic dish or a phased array antenna. This latter can be flat or cylindrical (as made in ARRC at Oklahoma University).

2.1.3. Transmitter

The transmitter of radar provides the power for the microwave pulses emitted in the form of radio frequency energy.

- Stores energy during the time interval between two pulses.
- Uses a series of timing pulses (trigger) at a rate establishing the PRT (Pulse Repetition Frequency).
- The timing pulse excites the modulator to deliver energy for a short time (pulse width) in a high voltage and high power.
- The pulse is amplified and plugged into the circulator in the form of a sine wave along the pulse.

2.1.4. Transmission

- The pulse travels through a waveguide to the feed-horn.
- This sends the pulse to the reflector of the antenna.
- The reflector concentrates the pulse in a narrow beam.
- The shape of the reflector determines the shape of the beam.

2.1.5. Reception

- The reflector intercepts the energy backscattered from targets.
- The energy is collected and conducted to the receiver through the circulator.
- The size of the reflector affects the amount of received energy.

2.1.6. Duty cycle

- The duration of the pulse is: τ [μsec]
- The length of the pulse is: h [m]
- The pulse repetition time is: T_s [ms]

The duty cycle is $\frac{\tau}{T_s}$ and relates the peak and average power in the determination of total energy output.

2.1.7. Pulse volume

- The angular resolution is particularly good as the width of the antenna beam is small.
- When the beam width is smaller, the required time to scan a volume is longer.
- The antenna is even larger when the beam width is smaller.
- Most weather radars (NexRad) use beam widths of about 1° .

Example: To sweep 360° and 20° elevation, $360 \times 20 = 7200$ elements should be addressed. The dwell time is around 0.05 sec.

The time required to scan the entire volume is

$$T = 7200 \times 0.05 = 360 \text{ sec} = 6 \text{ min.}$$

If a convective storm (rapidly changing) is considered, then 6 minutes is too long!

2.1.8. Receiver

The receiver is the most important organ of the entire composition of the radar, without neglecting the roles of the other components. It is mainly used to:

- Lower the frequency of the received signal to an intermediate frequency (IF).

- Amplify the IF signal.
- Filter the signal from the noise and other interferences.
- Amplify the desired signal to a level where the target information can be used by the signal processor.

2.2. Doppler weather radar

The Doppler weather radar is an active remote sensing instrument for a short term. It generates and emits pulses of electromagnetic waves of a given frequency.

Its purpose can be summarized by:

- Observation of clouds,
- Estimation of rainfall, hail, snow,
- Measurement of the wind velocity.

The pulsed Doppler weather radar consists mainly: [21]

- Radar: composed of an antenna, a transmitter, a receiver.
- Signal processing system: reflectivity, velocity and spectrum width of velocities estimation. Cancellation of ground clutter, data formatting.
- Analysis and data visualization system: weather analysis processors, associated colors display and different communication ports.

The modulator instructs the transmitter to transmit a pulse of a short duration (typically 1 microsecond). The transmitter generates the high amount of energy needed for sending. The antenna focuses this beam-shaped energy directed to a desired direction and waits for the reception of the echo to notify the receiver. The role of the duplexer is, first, to connect the transmitter to the antenna during the transmission phase. And then, it connects the antenna to the receiver during the reception phase.

The receiver amplifies the received energy, because it is very low, up to a usable level by the processing block.

The processing block deals with the received information and sends it to the display. Finally, the operator may interpret the displayed image.

The principle of detection is based on the transmission of powerful and very short pulses of electromagnetic energy concentrated in a narrow beam in the atmosphere

followed by the dispersion (backscattering) of the signal on the particles met in the air (droplets of water, dust, insects, ...) and the reception of this backscattered energy with an antenna.

2.2.1. Doppler effect

Discovered by the Austrian physicist Christian Doppler, it consists of a frequency shift of the sound proportional to the velocity of the moving source.

$$f_D = \frac{-v_D}{\lambda/2} = \frac{-2v_D}{\lambda} \quad (1)$$

The Doppler radar operates in the same way. While a target moves towards the radar, the frequency is increased; if the target is moving away (receding) from the radar, the frequency is reduced. The radar, then, compares the frequency of the received signal to the frequency of the transmitted signal. The difference is the frequency shift, giving the velocity of the target.

While moving targets changes the frequency of the electromagnetic energy, the change is usually too small to be accurately measured. Therefore, the Doppler radar focuses on the phase of the electromagnetic energy, as this aspect has a greater degree of variation and increases the probability of detecting the movement [22].

2.2.2. Phase shift

The phase of a wave is a specific point or landmark along this wave. A phase shift is observable by repositioning this mark between successive transmissions. A Doppler radar, in its simplest form, provides a reference signal, which can identify changes in the phase of the successively received pulses. The known phase of the transmitted signal allows the measurement of the phase of the received signal. The Doppler effect is associated to the phase change rate [22].

$$\frac{\Delta \phi}{\Delta t} = \frac{4\pi}{\lambda} v \quad (2)$$

2.2.3. Radial velocity

It should be emphasized that we only can extract the radial component of the velocity of the moving target seen by the Doppler radar. This is achieved by measuring the phase difference between two given instants.

$$v_D = \frac{\Delta\phi}{\Delta t} \times \frac{\lambda}{4\pi} \quad (3)$$

2.2.4. Ambiguous velocity

The maximum Doppler frequency, also called the Nyquist frequency, which can be measured unambiguously, is half the Pulse Repetition Frequency (PRF) of the radar:

$$f_{D_{max}} = \frac{PRF}{2} \quad (4)$$

Consequently, the maximum unambiguous velocity (Nyquist velocity) is

$$v_a = PRF \frac{\lambda}{4} \quad (5)$$

Thus, the range of unambiguous velocities that we can measure is $[-v_a, +v_a]$. A velocity $v > v_a$ would be interpreted as velocity of opposite direction.

2.2.5. Doppler dilemma

If one wants to detect higher velocities, he will need to either stretch the wavelength of the signal (but then, it would be impossible to detect some of the smaller particles: Rayleigh scattering) or increase the PRF.

The maximum unambiguous range is defined as the maximum distance from which the reflected signal of a pulse is received before the transmission of the next pulse.

$$r_a = \frac{c}{2 \cdot PRF} \quad (6)$$

The echo of a target at a distance $r > r_a$ is interpreted as an echo of a new

pulse to a distance ($r - r_a$).

Doppler dilemma is summarized by the expression.

$$v_a \cdot r_a = c \frac{\lambda}{8} \quad (7)$$

Doppler dilemma is caused by physical restrictions based on the laws of nature. The WSR-88D radar handles this dilemma by operating at staggering PRFs, collecting the range information at low PRFs and the velocity information at high PRFs. The two sets of information gathered are compared and processed to estimate the true radial velocities and ranges [23].

In Figure 2.1, the dashed lines highlight the association couples unambiguous speeds and unambiguous ranges.

2.3. Doppler weather radar products

Doppler weather radar provides estimates of basic atmospheric parameters:

- Radar reflectivity factor Z [dBZ]
- Mean radial velocity V_D [ms^{-1}]
- Spectrum width σ_v [ms^{-1}]

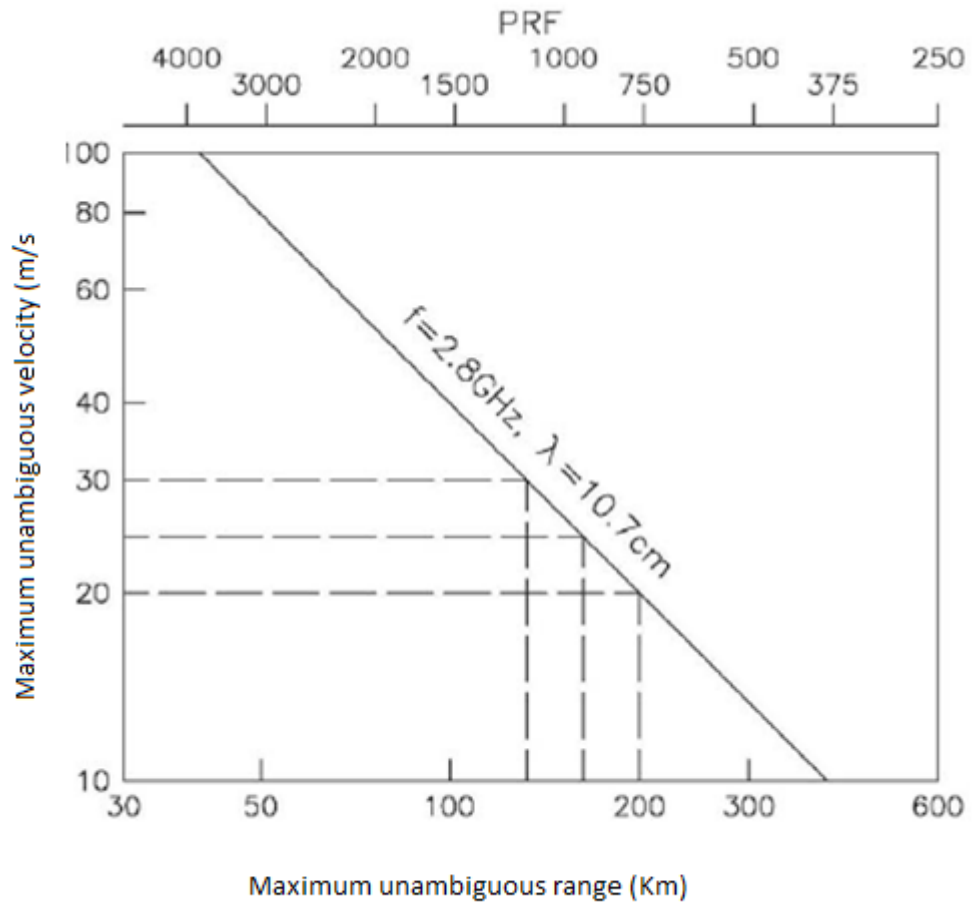


Figure 2.1: Illustration of the Doppler dilemma for a frequency $f = 2.8 \text{ GHz}$

2.4. Weather radar equations

We consider the WSR-88D radar with a transmitted peak power, P_t antenna gain, G , illuminating one single target whose radar cross section σ_b and is at a range r from the radar.

The incident power density P_i , assuming that there is no loss, is

$$P_i = \frac{P_t G}{4\pi r^2} \quad (8)$$

If the target does not absorb energy and backscatters isotropically then the backscattered power, P_r , intercepted by the radar antenna is

$$P_r = \frac{P_t G}{4\pi r^2} \sigma_b \frac{1}{4\pi r^2} A_e \quad (9)$$

where A_e represents the effective aperture area of the antenna and is (according to the theory of antennas)

$$A_e = \frac{G\lambda^2}{4\pi} \quad (10)$$

Thereby obtaining expression of the reverse power measured at the antenna level,

$$P_r = \left[\left[\left(\frac{P_t G}{4\pi r^2} \right) \sigma_b \right] \frac{1}{4\pi r^2} \right] \frac{G\lambda^2}{4\pi} \quad (11)$$

P_r : Collected power by the antenna

$\left[\left(\frac{P_t G}{4\pi r^2} \right) \sigma_b \right]$: Backscattered power by the target

$\left[\left[\left(\frac{P_t G}{4\pi r^2} \right) \sigma_b \right] \frac{1}{4\pi r^2} \right]$: Power density at the antenna

$\left(\frac{P_t G}{4\pi r^2} \right)$: Incident power density

In the case of weather targets, the radar illuminates a large number of targets (distributed targets, ex. raindrops) at the same time and the average power return is

$$\bar{P}_r = \frac{P_t G^2 \lambda^2}{(4\pi)^3 r^4} \sum_{i=1}^N \sigma_{bi} \quad (12)$$

The sum is performed on the volume receiving the power. If targets are uniformly distributed then

$$\sum_{i=1}^N \sigma_{bi} = \text{volume} \times \eta \quad (13)$$

η is the radar cross section per unit volume. The volume in question is (see Figure 2.2):

$$volume = Vol = \pi \left(\frac{r\theta}{2} \right) \left(\frac{r\phi}{2} \right) \left(\frac{c\tau}{2} \right) \quad (14)$$

Or

$$Vol = \frac{\pi\theta\phi r^2}{8} c\tau \quad (15)$$

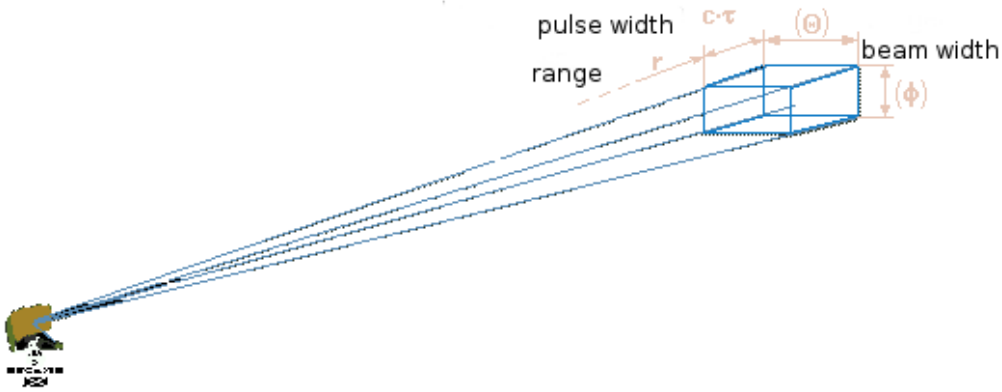


Figure 2.2: Volume resolution at range r

2.4.1. Equivalent radar reflectivity

For a meteorologist, the amount of water contained in a detection volume is very significant. Weather radar describes targets by a factor called equivalent radar reflectivity, Z_e connected to η by the following expression:[24][21]

$$\eta = \frac{\pi^5}{\lambda^4} |K|^2 Z_e \quad (16)$$

where $|K|^2$ represents the complex refractive index ($K = 0.93$ for water and $K = 0.208$ for ice). Considering that the diameter of raindrops spheres is D_e , then the expression of the equivalent reflectivity Z_e is reduced to

$$Z_e = \frac{6\lambda^4 \sigma_b M}{\pi^6 |K|^2 \rho D_e^3} \quad (17)$$

where M is the mass of liquid water and ρ the density of water. This ratio is commonly expressed in $mm^6 m^{-3}$. It requires a 10^{-18} conversion factor to be

consistent with the units of η [m^{-1}] (unit area over unit volume).

2.4.2. Radar equation

The composite radar cross section is given by the following expression

$$\sum_{i=1}^N \sigma_{bi} = Vol \times \eta = \frac{c \tau}{2} \frac{\pi \theta^2 r^2}{8 \ln 2} \frac{\pi^5}{\lambda^4} |K|^2 Z_e \quad (18)$$

Substituting this expression into the equation of the reflected average power,

$$\bar{P}_r = \frac{\pi^3 P_t G^2 \theta^2 c \tau |K|^2 Z_e}{2^{10} \lambda^2 r^2 \ln 2} L \quad (19)$$

Or

$$\bar{P}_r = \underbrace{\frac{\pi^3 c}{1024 \ln 2}}_{constants} \underbrace{\frac{P_t \tau G^2 \theta^2}{\lambda^2}}_{radar} \underbrace{\frac{|K|^2 Z_e}{r^2}}_{target} L \quad (20)$$

where:

- \bar{P}_r : Backscattered mean power, [watts]
- P_t : Transmitted peak power, [watts]
- G: Antenna gain, [unitless]
- λ : Wavelength, [m]
- θ : Beamwidth, [radian]
- τ : Pulse duration, [sec]
- c : Speed of light , [ms-1]
- r : Range to the considered volume, [m]
- Z_e : Equivalent radar reflectivity factor, m^3 (units [$mm^6 m^{-3}$] are often used for the empirical equation of precipitation).
- K : Complex refractive index.
- L : Loss factor associated with the propagation and detection of the receiver.

Hence the expression of the equivalent radar reflectivity factor

$$Z_e = \frac{1024 \ln 2}{c \pi^3} \frac{\lambda^2}{P_t \tau G^2 \theta^2} \frac{\bar{P}_r r^2}{|K|^2} \frac{1}{L} \quad (21)$$

If the following conditions are satisfied, then the equivalent reflectivity factor Z_e becomes simply the reflectivity factor Z , and the expression is:

$$Z = \frac{1024 \ln 2}{c \pi^3} \frac{\lambda^2}{P_t \tau G^2 \theta^2} \frac{\bar{P}_r r^2}{|K|^2} \quad (22)$$

[mm^6/m^3] is the standard used unit.

- The particles of precipitations are homogeneous dielectric spheres of the same nature.
- The particles are widespread throughout the volume.
- The reflectivity factor Z is uniform and constant throughout the volume.
- The microwave attenuation is negligible over the entire distance between the target and the radar antenna.

This expression represents the intensity of the received signal by the radar. It is normally used on a logarithmic scale. It is displayed on screens in dBZ

$$Z \text{ in dBZ} = 10 \log_{10}(Z) \quad (23)$$

Numerical span of Z

The following table (Table 2) shows the reflectivity span in correspondence to the type of precipitation and that it is more convenient to use a logarithmic scale dBZ than the linear scale Z .

$dBZ = 10 \log_{10} \left(\frac{Z}{1 \frac{mm^6}{m^3}} \right)$	$Z = 10^{10 \log_{10}(Z)}$	Precipitation
75	31 622 777	Large hailstones
50	100 000	Heavy rain
25	316	Snow
-28	0.001585	Fog droplets

Table 2 Reflectivity span in correspondence to the type of precipitation.

2.5. Signal processing

The purpose of signal processing is to: [24]

- Provide accurate and unbiased estimates of the characteristics of the desired atmospheric echoes.
- Estimate the measurement accuracy.
- Mitigate the effects of interfering signals.
- Reduce the flow of data.

The signal received by the radar and from meteorological target is represented by a narrow-band Gaussian process [25] for the following reasons:

- The number of backscattering particles contained in the volume of a pulse is very large ($> 10^6$).
- The volume of the pulse is very large compared to the wavelength of the transmitted signal.
- The entire volume of the pulse is filled with backscattering particles.
- All backscattering particles are in motion caused among others by turbulence and shear.

The power spectral density of a weather signal is shown in Figure 2.3.

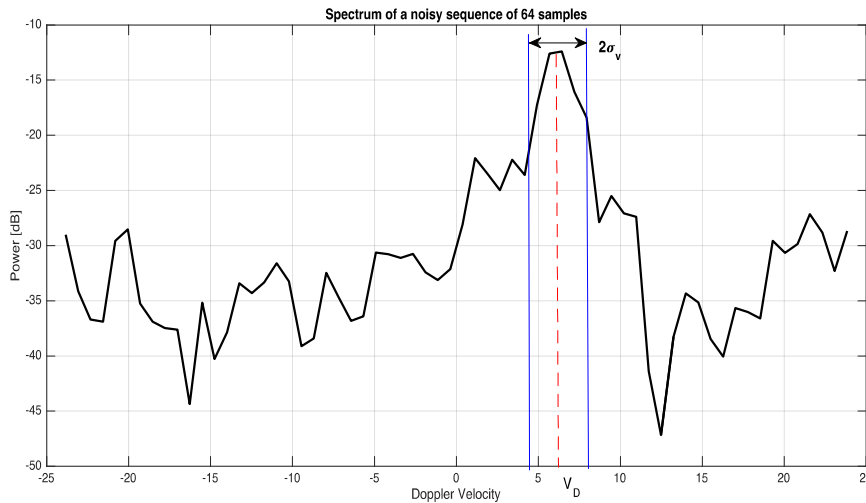


Figure 2.3: Doppler spectrum depicting the received power from a simulated weather perturbation, the mean radial velocity and spectral width of velocity.

The received power is the area under the curve and its expression is:

$$P_r = \int S(f) df = \int S(v) dv \quad (24)$$

This expression is also the zeroth spectral moment.

The frequency f and the velocity v are related by

$$f = \frac{2}{\lambda} v \quad (25)$$

The first spectral moment is the mean velocity

$$\bar{v}_D = \frac{\int v S(v) dv}{\int S(v) dv} \quad (26)$$

The second spectral moment is the variance

$$\sigma_v^2 = \frac{\int (v - \bar{v})^2 S(v) dv}{\int S(v) dv} \quad (27)$$

σ_v is the spectral width of velocities. This parameter measures the degree of perturbation prevailing in the given area.

Doppler spectrum contains information necessary for the measurement of atmospheric perturbation parameters.

The quadrature phase detection is used to obtain the real and imaginary parts of the complex envelope of the signal [24]. The complex signal is digitized into range gates as spatial resolution. A range gate is a distance equal to the radar pulse length. The time series obtained for each range gate is processed using various methods to estimate the parameters of interest.

Estimation of weather signal parameters is complicated by the presence of white noise and ground clutter. Most of this dissertation is based on how to deal with these problems.

2.6. Statistical parameter estimation

Doppler radar provides (for each radar resolution volume) estimates of the spectral moments of great importance [26]. The first three moments of the Doppler power spectral density (PSD) are directly related to the desired base parameters of the atmospheric perturbations: radar reflectivity (Z), mean radial velocity (v_D) and spectrum width of velocities (σ_v) [24]. The estimation of meteorological parameters is performed by range

cells. More detail is in the section devoted to signal processing (Chapter 3) [27].

Since the echo signal received by the radar from a range gate is generated by the reflection of a large number of randomly distributed particles and / or by variations of the refractive index of the atmosphere, then the process of the received signal may be considered (central limit theorem) or approximated by a Gaussian random process. [24] [26]

Therefore, signal processing techniques should be assessed within the context of a theory of statistical estimation framework where it is to determine the best estimates of all parameters.

This is a way to act effectively since, in this case, it is to quickly explore (by the rotating radar antenna) a meteorological phenomenon. This is because the nature of the random process of a meteorological signal will require to make averages. [24]

The process is Gaussian, the output voltage of the receiver of the radar has a zero mean. For this reason, the autocovariance function and the autocorrelation function are identical.

The power conservation connects the Doppler spectrum $S(v)$ to the power spectrum $S(f)$ by [26]

$$\bar{S}(v) = \frac{2}{\lambda} \bar{S}(f) \quad (28)$$

Radar signals (transmitted and received) can be represented by [28]

$$x(t) = a(t) \cos[2\pi f_0 t + \alpha(t)] \quad (29)$$

where f_0 is the carrier frequency, $a(t)$ and $\alpha(t)$ represent the amplitude and the signal phase modulation respectively.

This expression can be developed:

$$\begin{aligned} x(t) &= a(t) \cos[\alpha(t)] \cos(2\pi f_0 t) - a(t) \sin[\alpha(t)] \sin(2\pi f_0 t) \\ &= I(t) \cos(2\pi f_0 t) - Q(t) \sin(2\pi f_0 t) \end{aligned} \quad (30)$$

$I(t)$ and $Q(t)$ are the in-phase and quadrature components of the modulation.

The received signal is complex:

$$s(t) = [I(t) + jQ(t)]e^{j2\pi f_0 t} \quad (31)$$

To distinguish between the received signal and the transmitted signal, it is necessary to write

$$s_{tr} = U_{tr}(t)e^{j2\pi f_0 t} \quad \text{as the transmitted signal.}$$

$$s_r = V_r(t)e^{j2\pi f_0 t} \quad \text{as the received signal.}$$

U_{tr} and V_r are the complex envelope.

Typically, a precipitation is composed of a large number of hydrometeors extending over a large volume, each with its scattering amplitude and velocity. The received voltage may be expressed by:

$$V_r(t) = \sum_k A_k(\tau_k, t)e^{-j2\pi f_0 \tau_k} U_{tr}(t - \tau_k) \quad (32)$$

A_k is the scattering amplitude of the k th particle and $\tau_k = 2 \cdot \frac{r_k}{c}$

V_r is the resultant of the elemental phasors.

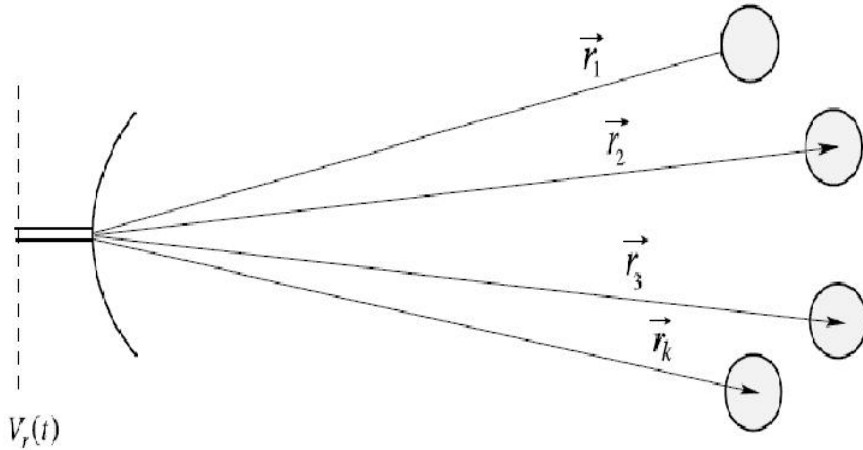


Figure 2.4: Set of random particles for which the instantaneous positions are described by vectors r_k relative to the radar.

Each one of the particles backscatter a portion of the total power towards the radar. The resultant complex signal at the detector embeds information of magnitude and information of phase.

2.6.1. Estimation of received mean power

The prominent measure of the radar is the average power corresponding to the voltage $V_r(t)$. It can be related to the radar cross section per unit volume of precipitation. [28]

The average power of the received signal, $V_r(t)$ in Figure 2.4 is obtained by averaging the samples of instantaneous power. These are a sequence of voltages:

$$IQ[m], m = 1, 2, \dots, M \quad (33)$$

Hence $\hat{P} = \frac{1}{M} \sum_{m=1}^M P_m$, where $P_m = |IQ[m]|^2$ and \bar{P} is the average power.

Radar reflectivity and equivalent reflectivity factor (Z_e) are proportional to the average power of the received signal [28]. The estimated average power converges to the average power of the signal as the number of samples used for estimation increases.

A complex sample $I + jQ$ is the summation of all the elementary backscattered voltages from the resolution volume as it is shown in the Figure 2.5.

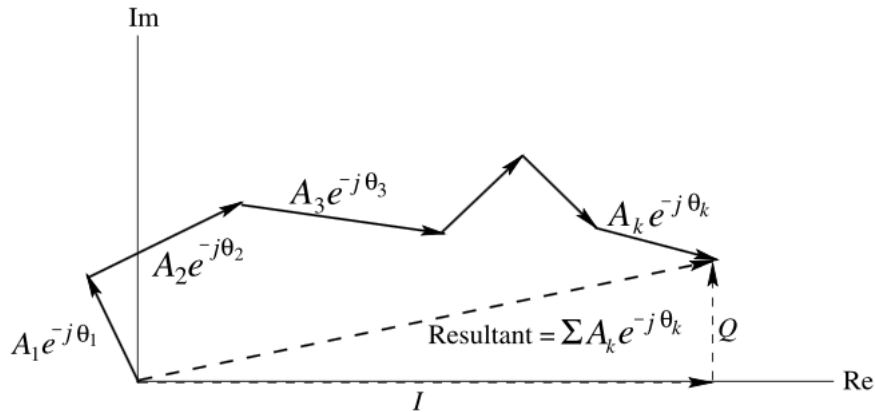


Figure 2.5: The resultant phasor is $I + jQ$ where I refers to the in-phase component and Q refers to the quadrature-phase component.

The variance of the estimated average power can be obtained by: [28]

$$\text{var}[\hat{P}] = \frac{1}{M^2} \sum_{i=1}^M \sum_{j=1}^M \text{cov}(P_i, P_j) \quad (34)$$

where $\text{cov}(P_i, P_j)$ is the covariance between i and j samples. We can simplify the expression to

$$\text{var}[\bar{P}] = \frac{\bar{P}^2}{M} \sum_{l=-(M-1)}^{M-1} \left(1 - \frac{|l|}{M}\right) \rho_p[l] \quad (35)$$

where $\rho_p[l]$ is the correlation coefficient at lag l .

2.7. Dual polarization Doppler weather radar

Typically, single polarized Doppler weather radar only estimates the first three spectral moments of the echo signal, namely the reflectivity (Z), the mean radial velocity (v_D) and the spectrum width (σ_v), whereas polarimetric signals contain significant information about hydrometeor features and the information can be retrieved with sufficient accuracy to be useful.

To fully take advantage of polarimetry, it is necessary to probe the hydrometeor medium with two orthogonal polarizations: Horizontal and vertical polarizations. The vertical–horizontal polarization basis is well suited for surveillance radars because the electric fields are aligned with the principal axis of several hydrometeor types. This maximizes the contrasts between scattering properties of vertically and horizontally polarized waves [29].

The transmitted signals can be either alternated or simultaneous. In the alternate transmission mode, signals power is the same for the two polarization channels, but the number of collected samples is divided by two in each channel.

In the simultaneous mode, each channel is fed by half of the total power (loss of sensitivity) whereas the number of samples is the total number that can be collected in a dwell time, in each channel.

The most commonly exploited radar quantity used by radar meteorologists is arguably the power-based radar reflectivity factor (Z). The equivalent radar reflectivity factor can be expressed as

$$Z_i = \frac{\lambda^4}{\pi^5 |K_w|^2} \int_0^\infty \sigma(D) N(D) dD = \frac{4\lambda^4}{\pi^4 |K_w|^2} \int_0^\infty |f_{hh,vv}^{(b)}(D)|^2 N(D) dD \quad (36)$$

where the index $i = h, v$ stands for one of the two polarizations (horizontal h and vertical v), λ is the radar wavelength, $K_w = \frac{m^2 - 1}{m^2 + 2}$ is a dielectric factor of water

(and m is the complex index of refraction), $\sigma(D)$ is the radar backscattering cross-section, $N(D)$ is the drop-size distribution (DSD), $f_{ii,ii}^{(b)}(D)$ is the backscattering amplitudes at two orthogonal polarizations (typically horizontal (H) and vertical (V)). Z_i is calculated in units of $mm^6 m^{-3}$.

Additional power-based products are produced by radar systems that transmit and receive along two orthogonal polarization planes (H and V). The utility of a ratio-based quantity, differential reflectivity, was first noted by Seliga and Bringi (1976). Differential reflectivity is defined as the logarithmic ratio of the horizontal to vertical power returns in a pulse volume

$$Z_{DR} = 10 \log_{10} \frac{Z_h}{Z_v} = Z_H - Z_V \quad (dB) \quad (37)$$

where Z_h and Z_v are given in linear units and Z_H and Z_V are given in logarithmic units. Differential reflectivity, in dBZ units, is the difference between horizontal and vertical reflectivities. Its values range from -7.9 to 7.9 decibels (dB).

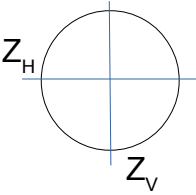
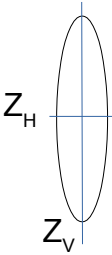
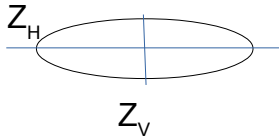
Shape		
Spherical (Drizzle, small hail)	Horizontally oriented (Rain, melting hail)	Vertically oriented (Ice crystals)
		
$Z_H \approx Z_V$	$Z_H > Z_V$	$Z_H < Z_V$
$Z_{DR} \approx 0$	$Z_{DR} > 0$	$Z_{DR} < 0$

Table 3 Differential reflectivity (Z_{DR}) is a good indicator of the mean drop shape of the dominant hydrometeor within the resolution volume.

At smaller diameters, raindrops tend to be spherical and at larger diameters the drops are rather oblate with the major axis aligned in the horizontal and the minor axis aligned in the vertical (Pruppacher 1970). This is why Z_H is larger than Z_V in rain, resulting in $Z_{DR} > 0$ dBZ as it is shown in the Table 3.

Chapter 3 : Doppler weather radar signal processing

3.1. Introduction

One major hypothesis is the following: the output signal from the receiver is a weighted sum with contributions from all scatterers in a resolution volume. The signal may be affected by independent sources (raindrops, snow, hail, ...). Consequently, we can apply the central-limit theorem to model it as a stochastic process with a Gaussian distribution [9].

Pulse Doppler weather radar signals are discrete and consists of a number of samples that must be processed in order to obtain accurate estimates. The dwell time, which is the collection time, is restricted by the necessity for faster antenna rotation rates. Nonetheless there is a high processing rate for a large number of radar volumes to cope with in a short time.

The weather radar signal processing objective is to provide accurate and unbiased estimates of the characteristics of meteorological echoes [25]. To achieve this, the signal processing algorithms have to eliminate or at least reduce the degrading effects of ground clutter and noise. After that, we can proceed with the estimation of weather echo characteristics.

Generally, weather targets velocities are about 50 m/s at most. The working frequencies of a weather radar are about 10^9 Hz corresponding to wavelengths of a few centimeters (<10 cm). The Doppler effect links the frequency shift of the transmitted signal to the velocity of the target. This frequency shift is just a few hundreds of Hz: it is far too low to be measured directly. To address this difficulty, various signal processing techniques can be performed on raw receiver signals. Digital signal processing is used in almost all

modern radars to perform these signal processing operations. We use different approaches in time-domain and in frequency-domain. In time-domain, we measure the phase difference between two successive pulses having probed the same resolution volume in space. Indeed, after the return of the second pulse, the target has changed its position which would result in a phase shift between the two pulses. Hence the birth of the pulse pair method.

The pulse pair estimator calculates the first three moments of the Doppler spectrum using the autocovariance function or autocorrelation.

In frequency-domain, the Fourier method is a nonparametric technique based on estimating the power spectral density (PSD) of the received signal.

This estimator based on the periodogram is not optimal in the sense that it is not derived from an optimality criterion [10][11]. Specifically, periodogram becomes an unbiased estimator when the number of samples tends to infinity. Additionally, the variance of periodogram is in proportion to the spectrum value [30]. It is, however, relatively of low complexity among other non-parametric methods. For this reason, other methods are used to improve the estimation of the spectrum (AR, ARMA).

The accuracy on the spectrum estimation is a real concern. We need to address the noise problem which is inherent to any electronic system. We also need to cope with the ground clutter which is also another issue especially when detected weather targets are moving too slow.

We usually consider the noise level as a constant. In reality, the noise depends on varying factors: temperature of receivers, fluctuations of the system gain and external noise. The sources of the external noise can be antenna elevation and precipitation along the radar beam[31][32]. Indeed, the noise increases if there is precipitation along the beam because particles radiate noise. Also, at low elevations, contribution from the ground increases the noise level.

3.2. Base data estimation

Weather echo is a sampled analog signal and the samples are taken at the PRT or T_s pace. The obtained time series IQ_k is M samples length. The number M is dictated by the PRT or T_s and the dwell time. Each sample is a weighted sum of echoes from randomly located scatterers. And because the scatterers are moving there will be fluctuations between all the samples powers S_k to which is added the noise

power . N_k .

This is to say the total power of each sample is $P_k = S_k + N_k$.

Signal processor provides the first three spectral moment. The zeroth moment corresponds to the weather signal mean power which is, in turn, related to the reflectivity Z , the first moment corresponds to the mean radial velocity v_D and the second moment corresponds to the spectral width of the spectrum σ_v .

3.2.1. Time domain estimators

Time domain moment estimation is based on the autocorrelation function of the received complex signal. An estimate of the autocorrelation function can be calculated from the complex time series IQ_k [25]

$$\hat{R}(m) = (M-m)^{-1} \sum_{k=0}^{M-m-1} IQ_k^* \cdot IQ_{k+m} \quad (38)$$

where m is the lag between the two time series (IQ_k and IQ_{k+m}).

3.2.1.1. Signal power

In modern radars, we use receivers with a square law transfer function because of the generated unbiased power estimate [30]. The signal power is the average of the M samples power of the time series.

$$\hat{S} = \frac{1}{M} \sum_{k=0}^{M-1} (P_k - N_k) \quad (39)$$

where P_k is the power of the k^{th} sample $P_k = |IQ_k|^2$ and N_k is the noise power accompanying the k^{th} sample.

3.2.1.2. Mean Doppler velocity

In time domain, we use the pulse pair or complex covariance technique to estimate the mean radial velocity [30][33][34].

$$\hat{v}_D = -\frac{\lambda}{4\pi T_s} \arg(\hat{R}[1]) = -\frac{\lambda}{4\pi T_s} \tan^{-1}\left(\frac{\text{Im}(\hat{R}[1])}{\text{Re}(\hat{R}[1])}\right) \quad (40)$$

3.2.1.3. Spectrum width

Spectrum width of velocities is the square root of the second central moment of the Doppler spectrum measuring the dispersion of velocities in the considered resolution volume. It is significant because it helps the interpretation of weather data.

It is assumed that the shape of the Doppler spectrum is Gaussian. In such a situation, the autocovariance or autocorrelation function takes the form [30]

$$R[mT_s] = S e^{-8\left(\pi\sigma_v \frac{mT_s}{\lambda}\right)^2} e^{-j4\pi v \frac{mT_s}{\lambda}} + N \delta[mT_s] \quad (41)$$

where S is the signal power, λ is the wavelength and N is the noise power.

From this expression, we infer the spectrum width of velocities as [30][33][34]

$$\hat{\sigma}_v = \frac{\lambda}{2\pi T_s \sqrt{2}} \left| \ln\left(\frac{\hat{R}[0]-N}{\hat{R}[1]}\right) \right|^{1/2} \text{sgn}\left(\frac{\hat{R}[0]-N}{\hat{R}[1]}\right) \quad (42)$$

where

$$\hat{R}[0] = \frac{1}{M} \sum_{k=0}^{M-1} |\hat{I}\hat{Q}[k]|^2 \quad (43)$$

and

$$\hat{R}[1] = \frac{1}{M-1} \sum_{k=0}^{M-2} \hat{I}\hat{Q}^*[k] \cdot \hat{I}\hat{Q}[k+1] \quad (44)$$

According to [25], the pulse pair spectrum width is given by

$$\hat{\sigma}_v = \frac{\lambda}{2\pi T_s \sqrt{2}} \left[1 - P[1] \left(1 + \frac{1}{SNR} \right) \right]^{1/2} \quad (45)$$

where $P[1] = \frac{|R[1]|}{R[0]}$ is the normalized power at first lag.

As regards the SNR, it must be estimated separately.

By expanding the function \ln in the equation (42), [35][34] an expression of the spectral width is derived as follows

$$\hat{\sigma}_v = \frac{\lambda}{2\pi T_s \sqrt{2}} \left| 1 - \frac{|\hat{R}[1]|}{\hat{S}} \right|^{1/2} \operatorname{sgn} \left(1 - \frac{|\hat{R}[1]|}{\hat{S}} \right) \quad (46)$$

where

$$\hat{S} = \hat{R}[0] - N = \frac{1}{M} \sum_{k=0}^{M-1} |\hat{IQ}[k]|^2 - N \quad (47)$$

is the estimated power when noise is deducted.

3.2.2. Frequency domain estimators

The objective of spectral estimation is to infer the power spectral density (PSD) from a finite observation of the underlying process. The usage of spectral techniques to estimate the moments necessitates to assume that the data model is a sum of sinusoids. It is only after this that we can apply the Discrete Fourier Transform (DFT) to the complex signal in order to decompose it into a sum of sinusoids having amplitudes and phases that will be able to reconstruct the original discrete signal [25]. This simple periodogram based estimator is not optimal in the sense that it was not derived from any optimality criterion, and it is not able to achieve uniformly optimal statistical properties [10][11].

3.2.2.1. Windowing effects on spectrum estimation

The magnitude of a temporal window in the frequency domain provides two significant features. The width of its main lobe and the levels of its side lobes. A narrow main lobe provides a better frequency resolution [36][6] and low side lobes enhance the smoothing of the spectrum [36].

In practice, these two properties are never met together. In fact, the narrower its main lobe, the higher its side lobes. This constitute a typical tradeoff in spectrum estimation.

In frequency domain, a rectangular window has the narrowest main lobe, but its side lobes are the most important whereas Blackman window has weaker side lobes, but a

broader main lobe. The type of window is to choose according to what one wishes to observe in a spectrum.

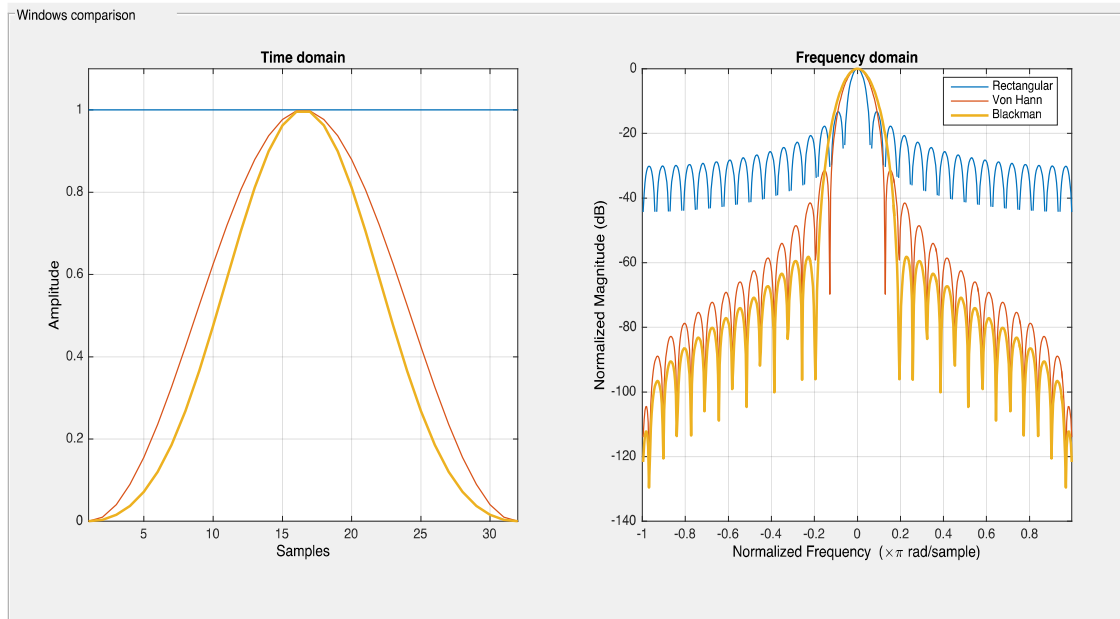


Figure 3.1: Typical windows behavior in the spectral domain. The rectangular window has the narrowest main lobe and the Blackman window has the lowest side lobes. The Von Hann window is the best bargain between the three windows.

Ideally, one has to use a window that can be transformed into the Dirac function in the frequency domain so as when convolved with the given signal, he would get the true spectrum. This is because the Dirac function is the neutral element of the convolution operation. Unfortunately, the desired window would be the rectangular window of infinite length. To overcome the problem of infinite length, we approximate the Dirac peak by narrowest peak with very low side lobes. Most often, the Von Hann window is used in weather radar applications.

If the true power spectrum is in a narrow bandwidth, its convolution operation with a window will smear it into adjacent frequency bins [6]. This frequency leakage phenomenon is window type dependent and has a detrimental effect on power spectrum estimation. Side lobes from adjacent frequency bins add in a constructive or destructive way to the main lobe of a response in another frequency bin of the spectrum [36]. This can mask weaker frequency components.

The applied window is the significant factor that determines the frequency resolution of a spectrum. For a rectangular window the width between 3 dB levels determines the frequency resolution [36].

3.2.2.2. Mean Doppler Velocity

The power spectrum using periodogram is calculated by

$$S[k] = \frac{T_s}{M} \left| \sum_{m=0}^{M-1} w[m] \cdot IQ[m] e^{-j \frac{2\pi m k}{M}} \right|^2 \quad (48)$$

where $k = 0, 1, \dots, M-1$ and w is the weighting window that can be of any type like Hanning, Hamming, etc. This window is used to reduce the side lobes of spectra.

The Doppler mean velocity of the scatterers contained in the resolution volume is [37]

$$\hat{v}_D = -\frac{\lambda}{2 \hat{P} T_s} \sum_{k=-\frac{M}{2}}^{\frac{M-1}{2}} \hat{S}(k) \cdot \left(\frac{k}{M-1} \right) \quad (49)$$

where

$$\hat{P} = \frac{1}{M} \sum_{m=0}^{M-1} |IQ(m)|^2 \quad (50)$$

To avoid biases due to aliasing of symmetric spectrum, a solution is found by Doviak and Zrnić by [30][34]

$$\hat{v}_D = -\frac{\lambda}{2 M T_s} \left\{ k_m + \frac{1}{\hat{P}} \sum_{k=-\frac{M}{2}}^{\frac{k_m+M}{2}} (k-k_m) \hat{S}[\text{mod}_M(k)] \right\} \quad (51)$$

where \hat{P} is the total power in the periodogram, $\text{mod}_M(k)$ is the remainder of the division of k by M and $-M/2 \leq k_m \leq M/2$ is the index of the strongest Fourier coefficient.

3.2.2.3. Spectrum width

Several ways to estimate the spectrum width are proposed. In 1993, D. Aalfs et al. [37] has given the expression

$$\hat{\sigma}_v^2 = \frac{\lambda^2}{4 \hat{P} T_s^2} \sum_{k=-\frac{M}{2}}^{\frac{M}{2}-1} \hat{S}(k) \left(\frac{k}{M-1} + 2 \hat{v}_D \frac{T_s}{\lambda} \right)^2 \quad (52)$$

And Doviak and Zrnić [35][34] have estimated the spectrum width by the expression

$$\hat{\sigma}_v^2 = \frac{\lambda^2}{4 \hat{P} T_s^2} \sum_{k=k_m-\frac{M}{2}}^{k_m+\frac{M}{2}} \hat{S}[\text{mod}_M(k)] \left(\frac{k}{M} + 2 \hat{v}_D \frac{T_s}{\lambda} \right)^2 \quad (53)$$

which acceptably avoids bias due to aliasing for only small widths but still has bias due to the windowing effect.

3.2.3. Enhancing spectra estimators performance

In weather radar applications using spectral approaches, periodogram based spectra are commonly used because a periodogram presents a good tradeoff between the complexity of computations and the efficiency of the mean Doppler velocity and spectral width estimations. It is classified as a non-parametric spectral approach.

The drawback of the method is the bias [38][30] of the estimators because of the windowing effect and short discretized signal (low frequency resolution) associated with the discrete Fourier transform.

In order to improve the spectral quality (accuracy, frequency resolution and detectability), one can use parametric techniques to define the spectrum model. Maximum entropy is one of the techniques in which we use the given weather signal samples to derive the parameters of the model. Hence the problem of spectral estimation is reduced to a parametric estimation where the spectrum is expressed by the model parameters. The most frequently used models in the literature are the autoregressive (AR), the moving average (MA), the autoregressive moving average (ARMA).

Atmospheric echoes can be modeled by autoregressive techniques and if noise is added to the data then the autoregressive moving average modeling will be more appropriate [37][39].

3.2.3.1. Autoregressive Modeling

In AR model, we assume that the observed data have been generated by a

system whose input-output is a linear difference equation given by

$$x_n = -\sum_{k=1}^p a_k \cdot x_{n-k} + n_n \quad (54)$$

where x_n is the observed output of the system, n_n is the unobserved input of the system, and the a_k are its parameters to determine. The input n_n is a zero mean white noise process driving the sequence with unknown variance σ_n^2 , and p is the order of the system. AR models are called all-pole models. The power spectral density associated with the $AR(p)$ model is expressed by

$$S_{AR}(f) = \frac{\sigma_n^2 T_s}{\left| 1 + \sum_{k=1}^p a_k \cdot e^{-j2\pi f k T_s} \right|^2} \quad (55)$$

where T_s is the sampling interval.

The spectral analysis in modeling approaches is a three step procedure:

- Select the model for the time series,
- Estimate the parameters of the assumed model from the data,
- Obtain the spectral estimate by substituting the estimated model parameters into the theoretical PSD implied by the model.

The autocorrelation estimate of a data set x_0, \dots, x_{N-1} is given by

$$\hat{R}_{xx}(m) = \frac{1}{N} \sum_{n=0}^{N-m-1} x_{n+m} x_n^* \quad (56)$$

for $m = 0, \dots, M$ and $M \leq N-1$

If we multiply the equation 54 by x_{n-k}^* and take the expectations of the two sides, we will obtain the equation 57 which is the relationship between the AR parameters and the autocorrelation function of x_n and also known as the Yule-Walker equations.

$$E[x_n x_{n-k}^*] = -\sum_{l=1}^p a_l E[x_{n-l} x_{n-k}^*] + E[n_n x_{n-k}^*] \quad (57)$$

which is equivalent to the equation 58

$$R_{xx}(k) = -\sum_{l=1}^p a_l R_{xx}(k-l) + E[n_n x_{n-k}^*] \quad (58)$$

or

$$R_{xx}(k) = \begin{cases} -\sum_{l=1}^p a_l R_{xx}(k-l), & \text{for } k>0 \\ -\sum_{l=1}^p a_l R_{xx}(-l) + \sigma_n^2, & \text{for } k=0 \end{cases} \quad (59)$$

These equations can be rewritten in a matrix form

$$\begin{bmatrix} R_{xx}(0) & R_{xx}(-1) & \dots & R_{xx}(-p) \\ R_{xx}(1) & R_{xx}(0) & \dots & R_{xx}(-(p-1)) \\ \vdots & \vdots & \ddots & \vdots \\ R_{xx}(p) & R_{xx}(p-1) & \dots & R_{xx}(0) \end{bmatrix} \cdot \begin{bmatrix} 1 \\ a_1 \\ \vdots \\ a_p \end{bmatrix} = \begin{bmatrix} \sigma_n^2 \\ 0 \\ \vdots \\ 0 \end{bmatrix} \quad (60)$$

There are several ways to solve these linear equations for the parameters a_1, \dots, a_p and σ_n^2 [40][41].

In accordance with the conjugate symmetric property of the autocorrelation function of a stationary process, we calculate the negative lags estimate by

$$\hat{R}_{xx}(-m) = \hat{R}_{xx}^*(m) \quad (61)$$

The Levinson-Durbin algorithm [42][43] is used to compute the parameters instead of the Gaussian elimination because of its computational efficiency (p^2 operations instead of p^3 for the Gaussian method). The algorithm proceeds recursively to compute all the parameters even those of orders lower than p :

$$\{a_{11}, \sigma_1^2\}, \{a_{21}, a_{22}, \sigma_2^2\}, \dots, \{a_{p1}, a_{p2}, \dots, a_{pp}, \sigma_p^2\}$$

The final set $\{a_{p1}, a_{p2}, \dots, a_{pp}, \sigma_p^2\}$ is the desired solution.

The algorithm is initialized by

$$a_{11} = -R_{xx}(1)/R_{xx}(0) \quad (62)$$

$$\sigma_1^2 = (1-|a_{11}|^2)R_{xx}(0) \quad (63)$$

for any other parameter of index $k = 2, \dots, p$

$$a_{kk} = -\left[R_{xx}(k) + \sum_{l=1}^{k-1} a_{k-1,l} R_{xx}(k-l) \right] / \sigma_{k-1}^2 \quad (64)$$

$$a_{kl} = a_{k-1,l} + a_{kk} a_{k-1,k-l}^* \quad (65)$$

$$\sigma_k^2 = (1-|a_{kk}|^2) \sigma_{k-1}^2 \quad (66)$$

Several research works have been done to solve the Yule-Walker equations but the most popular approach was introduced by Burg in 1975 [44].

The autoregressive modeling approach suffers from the selection of the right order p for the model to choose for the data set. Indeed, a too low order results in a highly smoothed spectral estimate and a too high order introduces spurious spikes in the spectrum. For these reasons, several criteria have been proposed to solve the problem but none of them was really satisfying in all cases[45][46][47].

For low SNR, the resolution is degraded and is no longer better than that obtained by the periodogram approach. The degradation reason is that the AR model assumed is no longer valid in presence of noise. To reduce the effect of this problem, one can use different approaches:

- Use ARMA modeling,
- Filter the data to reduce the noise,
- Use a larger order for the AR model.

3.2.3.2. ARMA modeling

The power spectral density estimation using ARMA modeling goes through the Yule-Walker equations as well. The ARMA model assumes that the data set can be modeled as an output of a p poles and q zeros filter driven by a white noise.

The difference equation of the model is given by

$$x_n = -\sum_{k=1}^p a_k x_{n-k} + \sum_{k=0}^q b_k n_{n-k} \quad (67)$$

If we multiply the equation (67) by x_{n-k}^* and take the expectations of the two sides, we will obtain the equation (68) which is the relationship between the ARMA parameters and the autocorrelation function of the data set x_n and also known as the Yule-Walker equations.

$$R_{xx}(l) = E[x_n \cdot x_{n-l}^*] = -\sum_{k=1}^p a_k R_{xx}(l-k) + \sum_{k=0}^q b_k R_{nx}(l-k) \quad (68)$$

where $R_{nx}(l-k) = \sigma_n^2 h_{k-l}^*$ because the ARMA process plays the role of a stable and causal filter.

From the equation (68), we derive the Yule-Walker equations

$$R_{xx}(l) = \begin{cases} -\sum_{k=1}^p a_k R_{xx}(l-k) + \sigma_n^2 \sum_{k=1}^q b_k h_{k-l}^*, & \text{for } l = 0, 1, \dots, q \\ -\sum_{k=1}^p a_k R_{xx}(l-k), & \text{for } l = q+1, q+2, \dots \end{cases} \quad (69)$$

After solving this set of nonlinear equations for a_1, a_2, \dots, a_p , b_1, b_2, \dots, b_q and σ_n^2 , we can obtain the power spectral density by

$$S_{ARMA}(f) = \frac{\sigma_n^2 T_s \left| 1 + \sum_{k=1}^q b_k e^{-j2\pi f k T_s} \right|^2}{\left| 1 + \sum_{k=1}^p a_k e^{-j2\pi f k T_s} \right|^2} \quad (70)$$

But the solution to this set of nonlinear equations (69) needs too much computation resources because of the matrices and iterative optimization techniques which don't fit real time processing applications [41] and most of all, it is not guaranteed to converge to the right solution. To avoid this issue, suboptimal approaches have been proposed in which the ARMA process is split into two processes (AR and MA) to be addressed separately.

Or, taking advantage of the Wold theorem asserting that any stationary ARMA model or MA process of finite variance can be represented as an AR model of possibly infinite order. This assertion [41] is very important because if a wrong model is chosen, we

may still obtain an acceptable approximation by using a higher order.

3.2.4. Artifacts removal

In polarimetric Doppler weather radar, noise powers in both receiving channels must be estimated. On the WSR-88D, noise is measured at highest elevations where radiation contribution from precipitation and ground is insignificant. Then the measured noise power is applied to low elevation observations where weather echo noise exists and the antenna intercepts thermal noise of the ground. Additional noise at lower elevations will bias the estimated weather characteristics unless it is correctly estimated which is hard to do [31].

3.2.4.1. Noise removal

Weather radar signals are usually contaminated with noise which has to be at least mitigated if not completely removed in order to gain more accuracy while estimating weather parameters values. When an erroneous noise level is used at low signal to noise ratios (SNR), estimators produce biased weather parameters (Reflectivity, radial velocity, spectrum width, ...).

In the USA, on the National Radar (WSR-88D), the noise level is measured as part of online calibrations. The measurement is performed after each volume scan at high antenna elevation angle. The obtained noise level value is adjusted for other elevations of the antenna.

Clearly, the drawback of such a procedure is that it doesn't take into account the temporal variations that can occur from one range location to another along one radial or from one azimuth to another on the same elevation. Temporal variations of the noise can be caused by many sources (cosmic radiations, water vapor, ...) [30]. Consequently, it is obvious that measuring the noise level at antenna pointing angle is very advantageous. This can be achieved operationally during data collection (online).

In 1974, P.H. Hildebrand and R.S. Sekhon [48] developed a method to objectively determine noise level in Doppler spectra. They took advantage from the property of white Gaussian noise considering that the standard deviation of the spectral densities is equal to the mean spectral density.

In 1992, Urkowitz and Nesper [49] used Kolmogorov-Smirnov test applied to the periodogram by iteratively discarding the Fourier spectral lines until satisfying the noise

hypothesis criterion.

In 2010, I.R. Ivic et al developed a method to estimate noise power dynamically from data. The approach requires an initial rough guess on the noise power. It attempts to disregard all samples at range locations where the presence of signal is detected [50].

3.2.4.2. Ground clutter removal

Ground clutter is a severe problem for weather radar when collecting information at close ranges and low elevations, in the vicinity of airports for instance. It is a factor limiting the performance of the weather radar system.

This clutter is received when the main lobe or side lobes of the antenna beam illuminate objects on the ground. If not removed, these clutter returns will seriously degrade meteorological estimates and tend reflectivity (Z) higher, Doppler velocity and spectrum width lower (toward zero).

A ground clutter filter (GCF) can mitigate the contamination and provide unbiased estimates with a reduced quality.

Moreover, significant biases may occur if the filter is applied when the clutter is simply absent and the radial velocity of the meteorological perturbation is low (close to zero). The presence or absence of the ground clutter is changing dynamically and thus making the problem of applying a GCF very complex.

So, designing a GCF to achieve the suppression of that clutter is the first part of the solution to the problem. We have to make the filter intelligent to decide to apply it only when it is needed.

Ground clutter is characterized by a strong power at reception with a very narrow spectrum width (0.3 m/s) and near zero velocity [30].

There have been several techniques addressing the ground clutter removal/mitigation problem.

In 1992, Sirmans developed a five pole elliptic infinite impulse response (IIR) filter to mitigate the effect of the ground clutter.

In 2004, Siggia and Passarelli [2] took advantage from the new generation of signal processors which provides greater processing power than on previous systems and proposed a greatly improved algorithm to deal with the ground clutter in the frequency domain. The designed filter is GMAP, standing for Gaussian Model Adaptive Processing [2]. The authors use a Gaussian clutter model to remove the ground clutter over a variable number of spectral components that is dependent on the assumed clutter width, signal

power, Nyquist Interval and number of samples. The filter is used to iteratively interpolate power over the components that have been removed (if there are any) and restore any overlapped weather spectral components with minimum bias.

Chapter 4 : Lifting-based wavelet transform in Doppler spectrum estimation

4.1. Introduction

Wavelet analysis is based on a key function $\psi(x)$ that is, more often, compactly supported (defined on a short interval) than not, where the wavelet basis is constructed by translating and dilating the function $\psi(x)$ as follows: $\{\psi_{j,k}\}_{j,k \in \mathbb{Z}}$, where

$$\psi_{j,k} = 2^{\frac{j}{2}} \psi(2^j x - k) \quad (71)$$

The parameters j and k are the dilation and the translation, respectively.

The basic unit in a wavelet transform is a filter bank, consisting of two filters: a high pass filter \tilde{g} and a low pass filter \tilde{h} . A discrete signal is filtered by both filters and then both down-sampled. The outputs are a high pass signal and a low pass signal, each containing half as much samples as the original signal.

In the inverse wavelet transform, both signals (high pass one and low pass one) are, first, up-sampled by inserting zeros in between every sample, then they are filtered by the filters g (high pass) and h (low pass) and the output is the merging of both signals (cf. Figure 4.1).

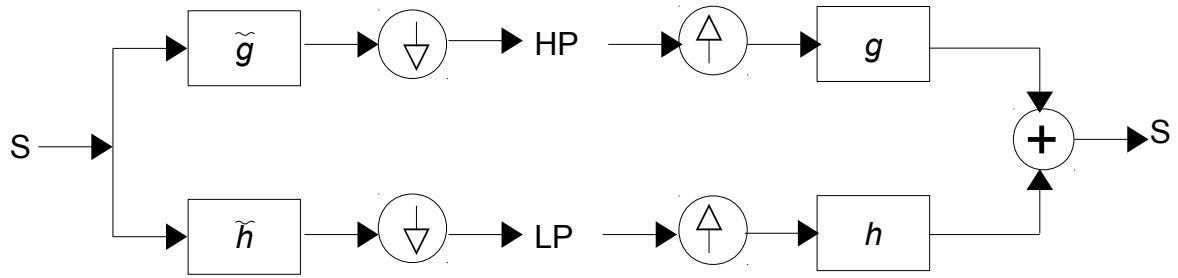


Figure 4.1: Discrete wavelet transform (one level).

The wavelet filters g and h define the primal wavelet function $\psi(x)$ and the primal scaling function $\phi(x)$, respectively. Also, the wavelet filters \tilde{g} and \tilde{h} define the dual wavelet function $\tilde{\psi}(x)$ and the dual scaling function $\tilde{\phi}(x)$, respectively.

If $g = \tilde{g}$ and $h = \tilde{h}$ then both wavelets (analysis and synthesis) coincide and called orthogonal. If the equalities are not satisfied then the wavelets are called biorthogonal wavelets.

Wavelet transform has a mother, $\psi(x)$, and a father, $\phi(x)$, wavelet and the link between them is

$$\phi(x) = \sqrt{2} \sum_{k \in \mathbb{Z}} h_k \phi(2x - k) \quad (72)$$

$$\psi(x) = \sqrt{2} \sum_{k \in \mathbb{Z}} g_k \phi(2x - k) \quad (73)$$

$$\tilde{\phi}(x) = \sqrt{2} \sum_{k \in \mathbb{Z}} \tilde{h}_k \tilde{\phi}(2x - k) \quad (74)$$

$$\tilde{\psi}(x) = \sqrt{2} \sum_{k \in \mathbb{Z}} \tilde{g}_k \tilde{\phi}(2x - k) \quad (75)$$

While \tilde{g}_k are coefficients representing the high pass filter coefficients, \tilde{h}_k are coefficients representing the low pass filter coefficients associated with the particular used wavelet function for decomposition. And g_k are coefficients representing the high pass filter coefficients, h_k are coefficients representing the low pass filter coefficients associated with the particular used reconstruction wavelet function.

So any function $f(x)$ can be represented by a discrete series as follows:

$$f(x) = \sum_k c_{j_0, k} \phi_{j_0, k}(x) + \sum_k \sum_{j > j_0} d_{j, k} \phi_{j, k}(x) \quad (76)$$

$$= c_{0,0} \phi_{0,0}(x) + \sum_k \sum_{j > j_0} d_{j, k} \phi_{j, k}(x) \quad (77)$$

where $c_{j,k}$ are associated with the father wavelet or scaling function (called the approximations) and $d_{j,k}$ are associated with the mother wavelet (called the details). The index k refers to the location when translating the wavelet and the index j refers to the scale or level when dilating the wavelet.

The lifting scheme consists of three steps to achieve a wavelet transform. They are used in the following way [51] as it is shown in Figure 4.2.

1. Split: in this stage, the signal is split into even indexed samples $s_{j,2k}$ and odd indexed samples $s_{j,2k+1}$:

$$(even_{j-1}, odd_{j-1}) = split(s_j) \quad (78)$$

2. Predict: the even samples are used to predict each odd sample by interpolation:

$$d_{j-1} = odd_{j-1} - P(even_{j-1}) \quad (79)$$

where P is the interpolating polynomial for prediction.

3. Update: this step is used to update the detail computed in the previous stage.

$$s_{j-1} = c_{j-1} = even_{j-1} + U(d_{j-1}) \quad (80)$$

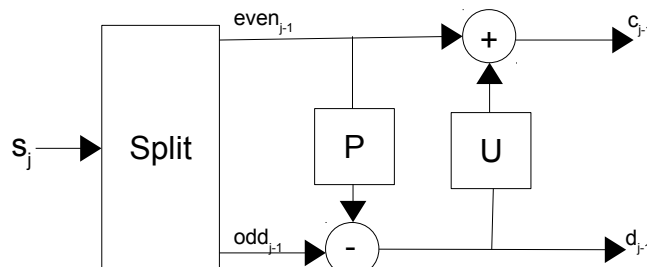


Figure 4.2: Wavelet transform via lifting scheme.

The inverse wavelet transform using the lifting scheme is achieved by first undoing the update stage to recover the even samples, then add the prediction to the details and recover the odd samples, as it is shown in Figure 4.3.

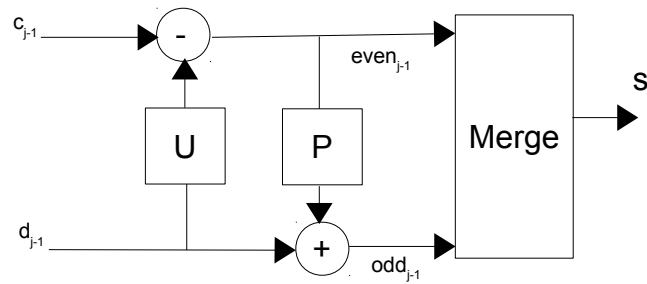


Figure 4.3: Inverse wavelet transform via lifting scheme.

1. Undo update: d_j and c_j are known, so

$$even_{j-1} = c_{j-1} - U(d_{j-1}) \quad (81)$$

2. Undo predict: $even_{j-1}$ and odd_{j-1} are known, so

$$odd_{j-1} = d_{j-1} + P(even_{j-1}) \quad (82)$$

3. Merge: odd_{j-1} and $even_{j-1}$ are known, so

$$s_j = merge(odd_{j-1}, even_{j-1}) \quad (83)$$

The inverse transform is computed by reversing the order of operations and flipping the signs.

The lifting scheme can be used for three (03) purposes:

- Generate a second generation wavelet [52][51].
- Enhance the performance of an existing wavelet by increasing the number of its vanishing moments [53].
- Decompose any wavelet transform into a finite sequence of simple filtering steps (known as lifting steps or ladder structure) [54].

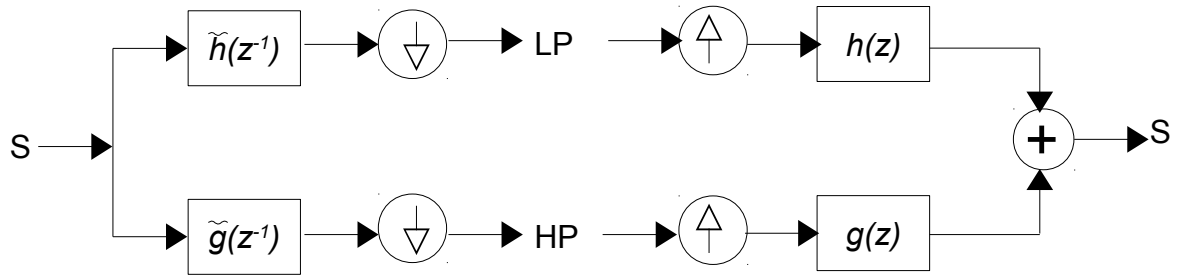


Figure 4.4: DWT: \tilde{h} (Low pass) and \tilde{g} (High pass) are the analysis filters of the forward transform; h (Low pass) and g (High pass) are the synthesis filters of the inverse transform.

To guarantee the perfect reconstruction of a signal, the following condition must be satisfied:

$$\begin{cases} h(z)\tilde{h}(z^{-1}) + g(z)\tilde{g}(z^{-1}) & = 2 \\ h(z)\tilde{h}(-z^{-1}) + g(z)\tilde{g}(-z^{-1}) & = 0 \end{cases} \quad (84)$$

Modulation matrices, for synthesis and analysis, can be defined, respectively, as

$$M(z) = \begin{bmatrix} h(z) & h(-z) \\ g(z) & g(-z) \end{bmatrix} \quad (85)$$

and

$$\tilde{M}(z) = \begin{bmatrix} \tilde{h}(z) & \tilde{h}(-z) \\ \tilde{g}(z) & \tilde{g}(-z) \end{bmatrix} \quad (86)$$

So the perfect reconstruction condition becomes

$$\tilde{M}(z^{-1})^t \cdot M(z) = 2 \cdot I = 2x \begin{bmatrix} 1 & 0 \\ 0 & 1 \end{bmatrix} \quad (87)$$

Nota bene: if the wavelet transform is orthogonal, then $h = \tilde{h}$ and $g = \tilde{g}$.
The polyphase representation of filters h and g is

$$\begin{cases} h(z) = h_e(z^2) + z^{-1}h_o(z^2) \\ g(z) = g_e(z^2) + z^{-1}g_o(z^2) \end{cases} \quad (88)$$

where the index “e” refers to the even coefficients and the index “o” refers to the

odd coefficients of the filters h and g .

$$h_e(z) = \sum_k h_{2k} z^{-k} \quad \text{and} \quad h_o(z) = \sum_k h_{2k+1} z^{-k} \quad (89)$$

$$g_e(z) = \sum_k g_{2k} z^{-k} \quad \text{and} \quad g_o(z) = \sum_k g_{2k+1} z^{-k} \quad (90)$$

Running the Euclidean division algorithm starting from h_e and h_o will yield [54]
[55]

$$\begin{bmatrix} h_e(z) \\ h_o(z) \end{bmatrix} = \prod_{i=1}^n \begin{bmatrix} q_i(z) & 1 \\ 1 & 0 \end{bmatrix} \begin{bmatrix} k \\ 0 \end{bmatrix} \quad (91)$$

where k is a constant.

Given the pair of filters (h, g) there exist Laurent polynomials $s_i(z)$ and $t_i(z)$ for $1 \leq i \leq m$ and $k \neq 0$ so that the polyphase matrix be

$$P(z) = \prod_{i=1}^m \begin{bmatrix} 1 & s_i(z) \\ 0 & 1 \end{bmatrix} \begin{bmatrix} 1 & 0 \\ t_i(z) & 1 \end{bmatrix} \begin{bmatrix} k & 0 \\ 0 & \frac{1}{k} \end{bmatrix} \quad (92)$$

and the dual polyphase matrix as

$$\tilde{P}(z) = \prod_{i=1}^m \begin{bmatrix} 1 & 0 \\ -s_i(z^{-1}) & 1 \end{bmatrix} \begin{bmatrix} 1 & -t_i(z^{-1}) \\ 0 & 1 \end{bmatrix} \begin{bmatrix} \frac{1}{k} & 0 \\ 0 & k \end{bmatrix} \quad (93)$$

The general lifted wavelet transform is given below by the Figure 4.5,

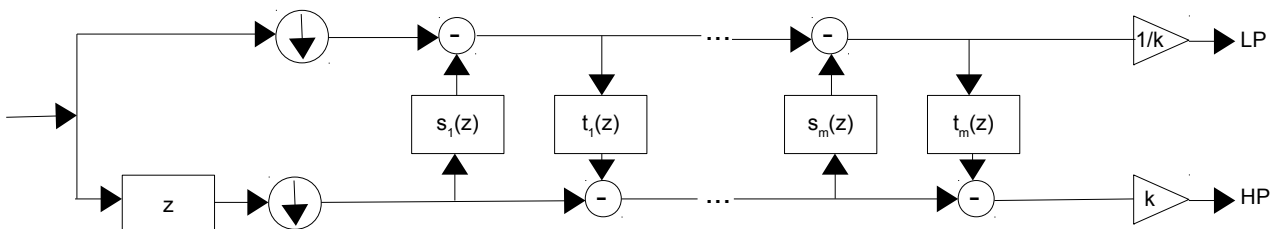


Figure 4.5: Forward wavelet transform using lifting scheme.

The corresponding inverse transform wavelet using lifting scheme is given in Figure 4.6.

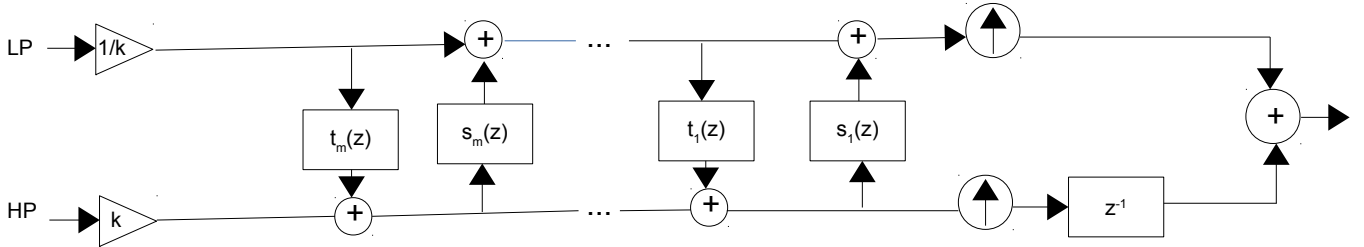


Figure 4.6: Inverse wavelet transform using lifting scheme

4.1.1. Example

Let's factor the Daubechies 4 (D4) into lifting steps. The corresponding h and g filters are given by [56][54]

$$\begin{aligned} h(z) &= h_0 + h_1 z^{-2} + h_2 z^{-2} + h_3 z^{-3} \\ g(z) &= -h_3 z^2 + h_2 z - h_1 + h_0 z^{-1} \end{aligned} \quad (94)$$

where $h_0 = \frac{1+\sqrt{3}}{4\sqrt{2}}$, $h_1 = \frac{3+\sqrt{3}}{4\sqrt{2}}$, $h_2 = \frac{3-\sqrt{3}}{4\sqrt{2}}$ and $h_3 = \frac{1-\sqrt{3}}{4\sqrt{2}}$

The polyphase matrix is

$$P(z) = \begin{bmatrix} h_0 + h_2 z^{-1} & -h_3 z - h_1 \\ h_1 + h_3 z^{-1} & h_2 z + h_0 \end{bmatrix} \quad (95)$$

The factorization of this matrix (reconstruction) will be

$$P(z) = \begin{bmatrix} 1 & -\sqrt{3} \\ 0 & 1 \end{bmatrix} \begin{bmatrix} \frac{\sqrt{3}}{4} + \frac{1}{4} z^{-1} & 0 \\ \frac{\sqrt{3}-2}{4} z^{-1} & 1 \end{bmatrix} \begin{bmatrix} 1 & z \\ 0 & 1 \end{bmatrix} \begin{bmatrix} \frac{\sqrt{3}+1}{\sqrt{2}} & 0 \\ 0 & \frac{\sqrt{3}-1}{\sqrt{2}} \end{bmatrix} \quad (96)$$

The corresponding diagram is shown in Figure 4.7.

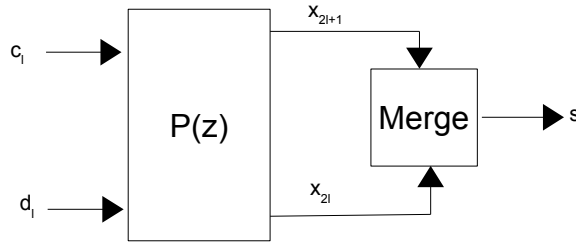


Figure 4.7: Inverse wavelet transform through lifting scheme using D4 wavelet.

and the dual polyphase matrix (analysis) is as follows:

$$\tilde{P}(z^{-1})^t = \begin{bmatrix} \frac{\sqrt{3}+1}{\sqrt{2}} & 0 \\ 0 & \frac{\sqrt{3}-1}{\sqrt{2}} \end{bmatrix} \begin{bmatrix} 1 & 0 \\ z^{-1} & 1 \end{bmatrix} \begin{bmatrix} 1 & \frac{\sqrt{3}}{4} + \frac{\sqrt{3}-2}{4} z^{-1} \\ 0 & 1 \end{bmatrix} \begin{bmatrix} 1 & 0 \\ -\sqrt{3} & 1 \end{bmatrix} \quad (97)$$

The corresponding diagram is shown in Figure 4.8.

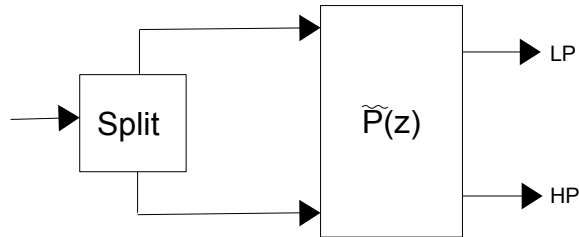


Figure 4.8: Forward wavelet transform through lifting scheme using D4 wavelet.

The implementation of the LWT through equations corresponding to the polyphase matrices computed previously are given by equations 98 and 99 for the forward wavelet transform and the inverse wavelet transform respectively.

$$\begin{aligned} d_l^{(1)} &= x_{2l+1} - \sqrt{3} x_{2l} \\ c_l^{(1)} &= x_{2l} + \frac{\sqrt{3}}{4} d_l^{(1)} + \frac{\sqrt{3}-2}{4} d_{l+1}^{(1)} \\ d_l^{(2)} &= d_l^{(1)} + c_{l-1}^{(1)} \\ c_l &= \frac{\sqrt{3}+1}{\sqrt{2}} c_l^{(1)} \\ d_l &= \frac{\sqrt{3}-1}{\sqrt{2}} d_l^{(2)} \end{aligned} \quad (98)$$

and

$$\begin{aligned}
d_l^{(2)} &= \frac{\sqrt{3}+1}{\sqrt{2}} d_l \\
c_l^{(1)} &= \frac{\sqrt{3}-1}{\sqrt{2}} c_l \\
d_l^{(1)} &= d_l^{(2)} - c_{l-1}^{(1)} \\
x_{2l} &= c_l^{(1)} - \frac{\sqrt{3}}{4} d_l^{(1)} - \frac{\sqrt{3}-2}{4} d_{l+1}^{(1)} \\
x_{2l+1} &= d_l^{(1)} + \sqrt{3} x_{2l}
\end{aligned} \tag{99}$$

4.2. Motivation

One of the challenges in real-time signal processing, in rapidly changing weather phenomena, is to process a large amount of data using newer algorithms consuming larger amount of computing resources because of the complexity of algorithms and because the Weather Service is required to deliver:

- Earlier warnings of potential hazardous storms such as tornadoes, hail, wind-shear, etc
- More accurate weather parameters such as rainfall rate, hydrometeors classification, etc.

For these reasons, in this work, a method is proposed for better estimating weather parameters without overwhelming the weather radar signal processor with extra computations.

The suggested procedure is estimating the Doppler spectrum using the well known lifting-based wavelet transform (LWT).

It's proven by [54] that for long and symmetric filters the lifting scheme halves the computation complexity ($O(n/2)$) compared to the standard wavelet transform with a complexity of $O(n)$.The standard wavelet transform is known to be more efficient than the FFT with its computation complexity of ($O(n \log n)$), as it is shown in Figure 4.9.

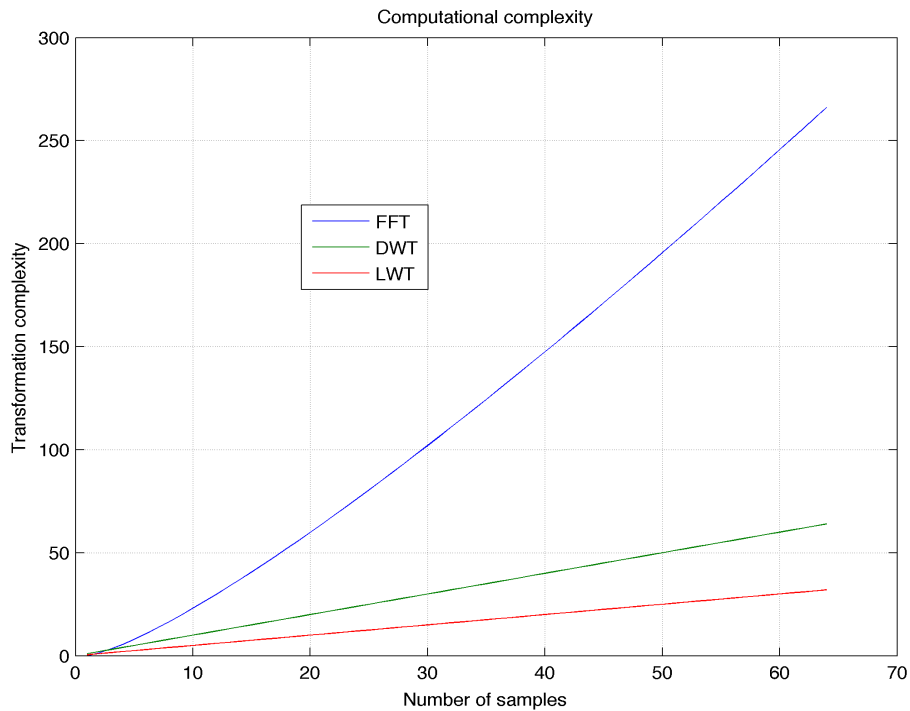


Figure 4.9: Computational complexity vs number of samples: Lifted wavelet transform is faster than DWT and FFT.

The specificity of this work lies in the determination of an adaptive threshold to apply on wavelet coefficients to mitigate the effect of different types of noises on weather parameters estimates. Next section will be devoted to the procedure presentation.

4.3. Wavelet choice

The selection of an optimal wavelet impacts substantially the performance of the denoising procedure. In weather radar applications, denoising signals using wavelet transform is a task requiring:

1. Perfect reconstruction conditions to be satisfied by the wavelet transform,
2. Smoothness of the denoised spectrum,
3. Fast processing to avoid being a burden for the radar system software.

There are many filters which satisfy the perfect reconstruction conditions but not as many for the fast processing requirement.

As for the smoothness of the spectrum after denoising, the wavelet needs to have more than one vanishing moment.

Fast processing is achieved by a lifted wavelet transform. This would be faster if the filters would be symmetric [54].

For all these requirements, the suitable wavelet for this application may be the biorthogonal wavelet Bior4.4.

This particular wavelet is symmetric and has four (4) vanishing moments.

4.4. Thresholding strategy choice

There is a variety of thresholds to apply for a given situation. These thresholds can be divided into two categories:

- Global thresholds,
- Level dependent thresholds.

The first category means that one applies one threshold value on all wavelet coefficients (over all different levels, if any), $\left[d_{jk} : j = j_0, \dots, J-1 ; k = 0, 1, \dots, 2^j - 1 \right]$, whereas for the second category, one applies one different threshold value T_j for each level $j = j_0, \dots, J-1$.

Any threshold requires knowledge of the noise level σ . In 1995, Donoho and Johnstone [57] argued that it is more important to estimate the noise level from given data than to assume it as known. In practice, it derives from the wavelet coefficients at the finest resolution. At this level, wavelet coefficients tend to consist only of noise. The authors derived the noise level as

$$\hat{\sigma} = \frac{MAD(d)}{0.6745} \quad (100)$$

where MAD stands for Median Absolute Deviation.

Deriving thresholds is performed by means of some known methods such as:

- Universal threshold,
- Minimax threshold,
- SURE (Stein's Unbiased Risk Estimate).

4.4.1. Minimax threshold

It is developed by Donoho and Johnstone [19] in 1994. This threshold is signal size dependent as well as noise level dependent:

$$T_{minimax} = \sigma T_M^*$$

where T_M^* is defined as the largest value of T by the expression

$$T_M^* = \inf_T \sup_d \left\{ \frac{\rho(T, d)}{M^{-1} + \min(d^2, 1)} \right\} \quad (101)$$

where $\rho(T, d) = E[(\hat{d}_T - d)^2]$ is the risk on the estimate \hat{d} of wavelet coefficient d .

4.4.2. Universal threshold

As an alternative to Minimax thresholds, Donoho and Johnstone suggested thresholding wavelet coefficients by using the universal threshold.

$$T_u = \hat{\sigma} \sqrt{2 \log(M)} \quad (102)$$

where M is the length of the sequence.

It is based on the hypothesis that noise superimposed on the underlying data is white and Gaussian. Its energy is distributed over all frequency bands (decomposition levels). Therefore, the standard deviation is calculated in a band where the useful signal (data) is absent or almost non-existent (in high frequency band).

4.4.3. SURE threshold

The threshold is selected for each resolution level of the wavelet transform. It is estimated based on the principle of minimizing the risk of unbiased estimate of Stein (SURE).

For actual signals (sequences), if $\hat{\mu} = \hat{\mu}(x)$ is a particular estimator of μ and if $x \sim N(\mu, 1)$, then according to [57], one can state that

$$\hat{\mu}(x) = x + g(x) \quad (103)$$

where $g(x)$ is a function from \mathbb{R} into \mathbb{R} . If $g(x)$ is weakly differentiable, then

$$E_\mu \left\{ \|\hat{\mu}(x) - \mu\|^2 \right\} = 1 + E_\mu \left\{ \|g(x)\|^2 + 2 \frac{dg(x)}{dx} \right\} \quad (104)$$

This equation is the risk on estimating $\mu(x)$ in an unbiased manner (SURE).

As regard to thresholding strategies, one can use one of the two most known and used in denoising applications. Hard thresholding and soft thresholding. Their corresponding effects are shown in Figure 4.10

4.4.4. Hard thresholding

if d is a wavelet coefficients vector and T is a selected threshold, then hard threshold estimator is as follows

$$\eta_T^{Hard}(d) = \begin{cases} d & \text{if } |d| \geq T \\ 0 & \text{if } |d| < T \end{cases} \quad (105)$$

4.4.5. Soft thresholding

Soft threshold estimator is given by

$$\eta_T^{Soft}(d) = \begin{cases} d \left(1 - \frac{T}{|d|}\right) & \text{if } |d| > T \\ 0 & \text{if otherwise} \end{cases} \quad (106)$$

Soft thresholding produces smoother results compared to those of hard thresholding. Hard thresholding, by contrast, produces a better preservation of discontinuities.

4.4.6. Other thresholds

Alongside soft and hard thresholds, other mitigation diagonal non-linearities can improve estimation of a desired signal [18].

$$\eta_T^{Diagonal}(d) = \max\left(1 - \frac{T^\beta}{|d|^\beta}, 0\right) \quad (107)$$

where $\beta > 0$.

When $\beta = 1$, the function corresponds to a soft thresholding non-linearity.

When $\beta = 2$, the function is between soft and hard thresholding.

When $\beta \rightarrow \infty$, the function corresponds to a hard thresholding.

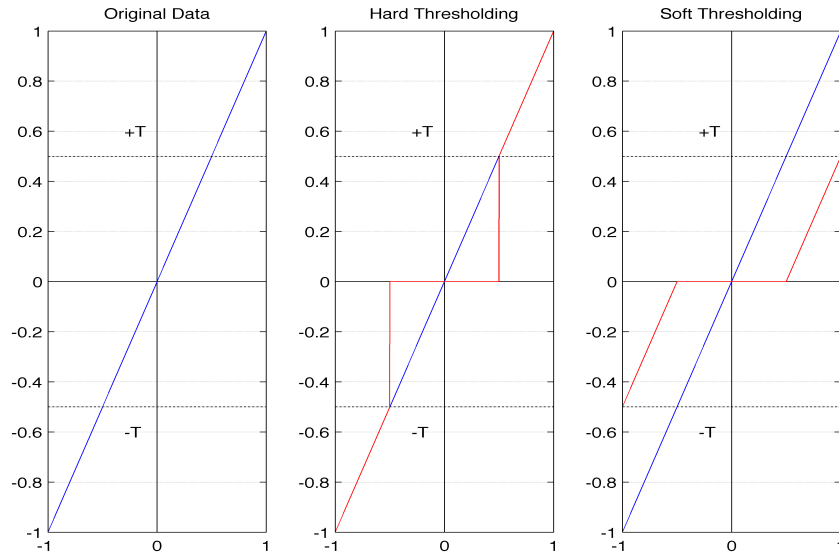


Figure 4.10: Output of hard and soft thresholds nonlinearities.

4.5. Algorithm for spectrum estimation

Doppler weather radar signal in a range gate is consisted of a time series or a sequence $IQ(kT_s)$ of M complex samples with T_s ms apart. M is defined by the dwell time MT_s (collection time of M samples for one estimate) of the radar. Currently, operational values can be:

- 40 for the phased array weather radar test-bed located in Norman, OK, USA,
- 40-280 for radars of the U.S. National Weather Service network (WSR-88D).

$$IQ(kT_s) = s(k)e^{-jw_D kT_s} + \sigma n(k) , \quad k = 0, \dots, M-1$$

where $s(k)$ is the weather echo signal free of white noise $n(k)$. This noise is an additive sequence of independent identically distributed (i.i.d.) Gaussian random variables, σ is the noise level and w_D is the Doppler pulsation (frequency).

Weather signals spectra from areas of uniform reflectivity would be closely resembling a Gaussian function [30]. Strong shear and turbulence would contribute to broaden spectra until obtaining a closely horizontal line in a “skirt” shape in the case of severe weather like tornadoes.

It is convenient to assume a Gaussian power spectrum for more than 75 % cases [30].

$$S(v) = \frac{S}{\sqrt{2\pi}\sigma_v} e^{-\frac{(v-v_D)^2}{2\sigma_v^2}} + \frac{N}{2v_a} \quad (108)$$

where:

- S , signal power [W],
- σ_v , spectral width [m/s],
- v , radial velocity [m/s],
- v_D , mean radial velocity [m/s],
- N , noise power [W],
- v_a , maximum unambiguous velocity [m/s].

Removing the noise from the sequence for $IQ(kT_s)$ (in the time domain) or removing it from $S(v)$ (in the frequency domain) is the same problem. But as I am required to work on spectral approaches, I decided to handle the denoising procedure in the frequency domain.

The periodogram of the time sequence IQ is given by

$$S(k) = \frac{T_s}{M} \left| \sum_{m=0}^{M-1} w(m) IQ(m) e^{-j\frac{2\pi mk}{M}} \right|^2 \quad (109)$$

where w is the window applied to the weather sequence IQ .

4.5.1. Spectral moments dependence with noise

It is obvious that noise affects substantially the quality of spectral moments estimates. Signal power is increased by noise power. Consequently, mean Doppler radial velocity estimate will decrease and spectrum width will be increased, as it is shown in Figure 4.11.

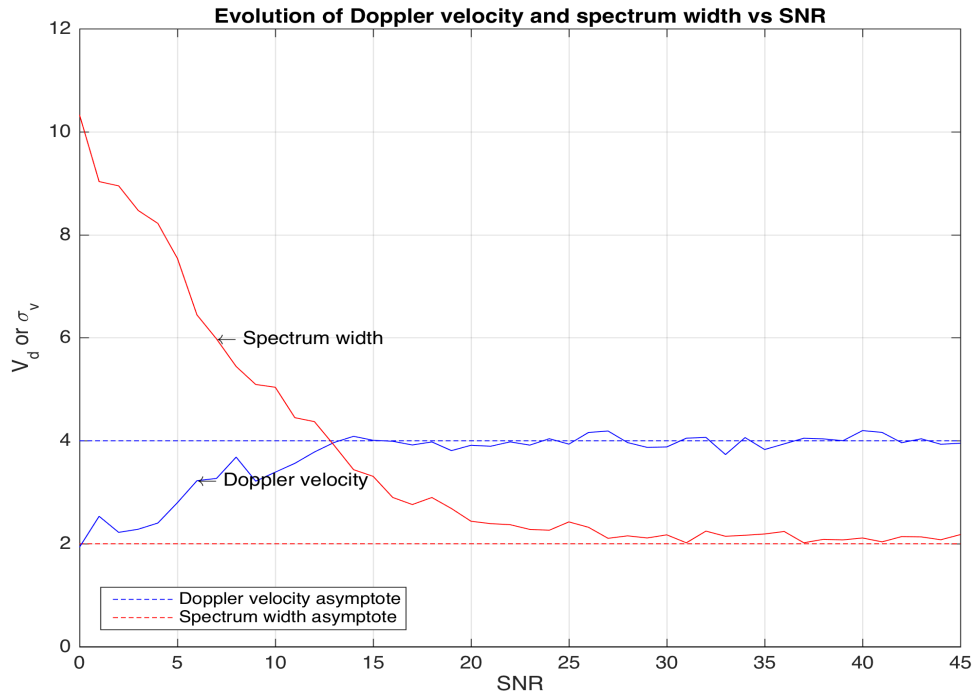


Figure 4.11: Evolution of radial velocity estimate and spectrum width estimate with noise level. In the present case, true radial velocity is 4 m/s and true spectrum width is 2m/s.

4.5.2. Procedure course

The proposed algorithm for the denoising procedure is built on two underlying parts:

Part 1: Obtain initial guesses for the threshold to use and for Doppler velocity and spectrum width. The corresponding flow chart is shown in Figure 4.12.

1. Windowing of the weather sequence for better performance. Usually, Hanning window works fine.
2. Calculation of periodogram is performed using the standard FFT.
3. Application of the LWT on the previously computed power spectral density to obtain at each level of decomposition two sequences of size $m = 2^{-j}M$ (j is the current decomposition level): coefficients of detail (d_m) and coefficients of approximation (c_m).
4. Calculation of the noise variance σ_n using the coefficients of wavelet previously obtained.

$$\sigma_n = \frac{MAD(d_m)}{0.6745} \quad (110)$$

where MAD is the median absolute value of the coefficients of details.

5. Set the universal threshold $t_u = \sigma_n \cdot \sqrt{\frac{2 \log(m)}{m}}$ and apply the soft threshold

$$\text{nonlinearity } \eta_t(d_{ij}) = \begin{cases} \text{sgn}(d_{ij})(|d_{ij}| - t) & \text{if } d_{ij} \geq t_u \\ 0 & \text{if } d_{ij} < t_u \end{cases} .$$

This means, a soft thresholding is applied on every wavelet coefficient d_{ij} , where $j = 1, \dots, J$ (J is the maximum decomposition level), $i = 1, \dots, m$, knowing that $m = 2^{-j} M$.

6. Invert the LWT, getting an estimated spectrum.
7. Compute the Doppler velocity V_D and spectral width σ_v using equations 51 and 53 respectively.

Part 2: Implementation of an iterative calculation of Doppler parameters. The corresponding flow chart is shown in Figure 4.13.

1. Increment the previously calculated threshold by dT_u step:

$$T_u = T_u + dT_u$$

2. Apply soft threshold non-linearity on the details previously calculated (in step 1) to obtain thresholded coefficients d_{thresh} with the new value of T_u .

3. Reconstruct the original spectrum sequence by inverse lifted wavelet transform:

$$S_{rec} = \text{ilwt}(c, d_{thresh})$$

4. Estimate weather parameters $(V_D)_{new}$ and $(\sigma_v)_{new}$

5. Compute increments of these parameters:

$$\begin{aligned} dV &= |(V_D)_{new}| - |(V_D)_{old}| \\ d\sigma &= |(\sigma_v)_{old}| - |(\sigma_v)_{new}| \end{aligned}$$

6. Test if $(dV > 0 \wedge d\sigma < 0)$: if the result is true, then loop from step1. If the result is false, then current values of V_D and σ_v are kept because the corresponding spectrum is optimally denoised.

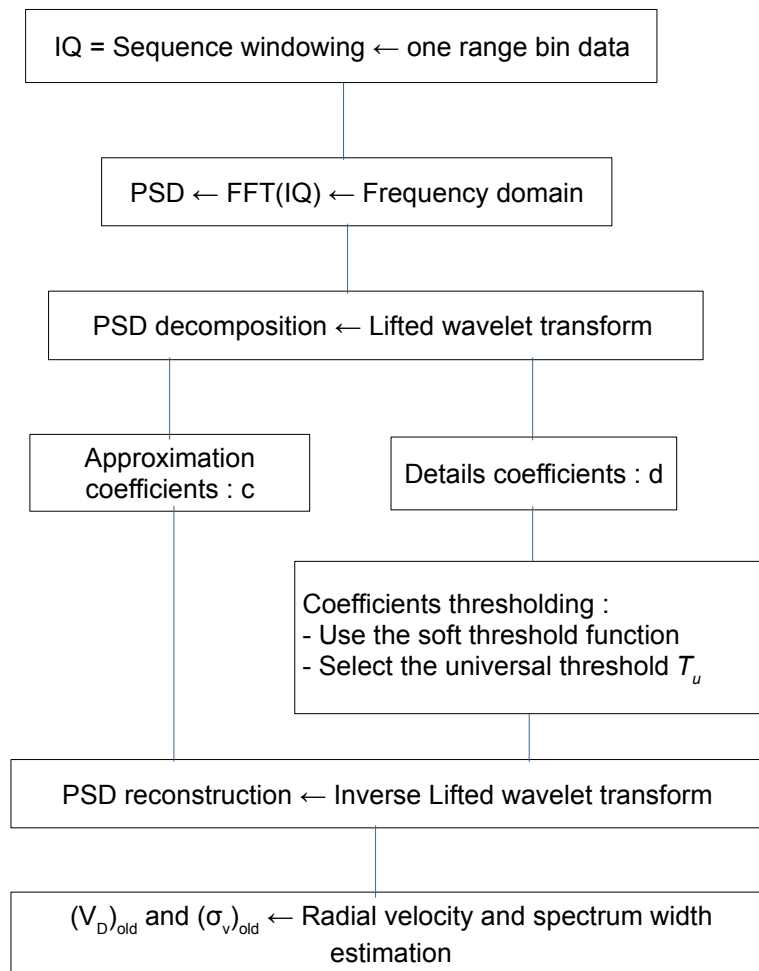


Figure 4.12: First step of weather radar spectrum denoising using lifted wavelet transform.

4.6. Case study

4.6.1. Available sources

In order to achieve a comprehensive test of the proposed algorithm, one should have real weather radar technical specifications along with actual data. The given opportunity is the phased array radar in the National Weather Radar Testbed (NWRT) located in Norman (Oklahoma, USA).

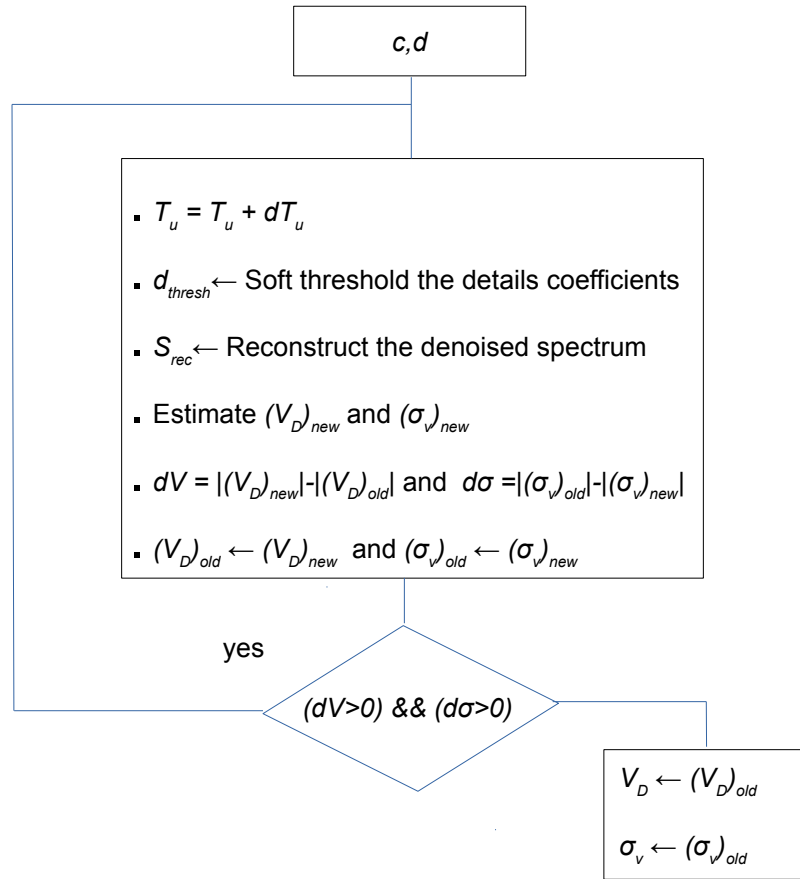


Figure 4.13: Second step of weather radar spectrum denoising using lifted wavelet transform.

The corresponding needed technical specifications of the phased array radar testbed are summarized in the Table 4

Feature	Value
Antenna (circular aperture)	3.66 m
Wavelength (λ)	0.0937 m
Beam width	1.5° (2.1° at 45° from beam center)
Transmitting peak power	750 Kw
Pulse width	1.57 μ s or 4.71 μ s
Pulse repetition time (PRT or T_s)	0.984 ms

Table 4: Technical specifications of the weather phased array radar testbed located in Norman (Oklahoma, USA).

4.6.2. Synthetic data

The first step is to generate synthetic weather signals corresponding to the radar specifications. This part is achieved by using the method proposed by Zrnić in 1975 [58].

Zrnić method can be conceived as a routine requiring some parameters as input (Radar power, maximum unambiguous Doppler velocity, SNR, sequence length, radial mean velocity and spectrum width corresponding to a weather perturbation) in order to produce a time series as output expected to represent a desired meteorological phenomenon.

However, some assumptions must be done. The radar return signal from a range gate is generated by backscattering from a large number of particles (meteorological, biological, dust, ...) randomly distributed and/or by refractive index changes in the atmosphere. The received signal can be considered (Central limit theorem) as or approximated by a Gaussian random process.

Furthermore, the random return is assumed to be a stationary process. It is characterized by the power spectral density (PSD) of a Gaussian statistical distribution given by the expression 111,

$$S(f) = \frac{1}{\sqrt{(2\pi)\sigma_v}} e^{-\frac{(f-f_D)^2}{2\sigma_v^2}} \quad (111)$$

where f is a frequency contained in the Nyquist interval, f_D is the Doppler frequency and σ_v is the spectrum width.

Moreover, some other assumptions are needed [58]:

- The spectrum of a weather echo is narrow band, unlike the noise spectrum that is broadband.
- Power of weather signal is larger than noise power.
- Statistical properties of a weather echo and those of noise are almost similar (Gaussian).

The probability density of a Doppler weather signal U can be written as [28]:

$$f(U) = \frac{1}{2\pi\sigma_v^2} e^{-\frac{|U|^2}{2\sigma_v^2}} = \frac{a}{2\pi\sigma_v^2} e^{-\frac{a^2}{2\sigma_v^2}} = f(a, \theta) \quad (112)$$

These equations can be decomposed into a product of two (02) functions $f_\theta(\theta)$ and $f_A(a)$ representing phase and amplitude respectively. This indicates that amplitude and phase are independent.

$$f(a, \theta) = f_A(a) \cdot f_\Theta(\theta) \quad (113)$$

where

$$f_A(a) = \frac{a}{\sigma_v^2} e^{-\frac{a^2}{2\sigma_v^2}}, \quad a > 0 \quad (114)$$

is a function representing a Rayleigh distribution, as in Figure 4.14.a, and

$$f_\Theta(\theta) = \frac{1}{2\pi}, \quad 0 < \theta \leq 2\pi \quad (115)$$

is a function representing a uniform distribution, illustrated in Figure 4.14.b.

Since for every sample k of the signal, its power is $P_k = |V_k|^2$ and mean power of the signal is $\bar{P} = E(|V|^2) = 2\sigma_v^2$, one can write

$$f_P(P) = \frac{1}{\bar{P}} e^{-\frac{P}{\bar{P}}}, \quad P > 0 \quad (116)$$

is a function representing an exponential distribution, shown in Figure 4.14.c.

4.6.3. Real data

The corresponding actual data are obtained for a full sector of this radar made of 109 radials. Each radial is an array of 2166 range bins and each range bin consists of 40 samples. These 40 samples from one range bin constitute one time series to analyze in order to produce the relevant spectral moments (Power, velocity, spectrum width).

We have dealt with actual radar raw data in the following circumstances:

- Date and time: 03.31.2009 at 02 h 23 min 53 s
- Elevation: 1.5°
- Range bins: two portions have been selected from two separate radials.
 - Radial # 1: the selected portion spans from range bin 70 to range bin 249, azimuth = 130°.
 - Radial # 100: the selected portion spans from range bin 350 to range bin 549, azimuth = 239°.

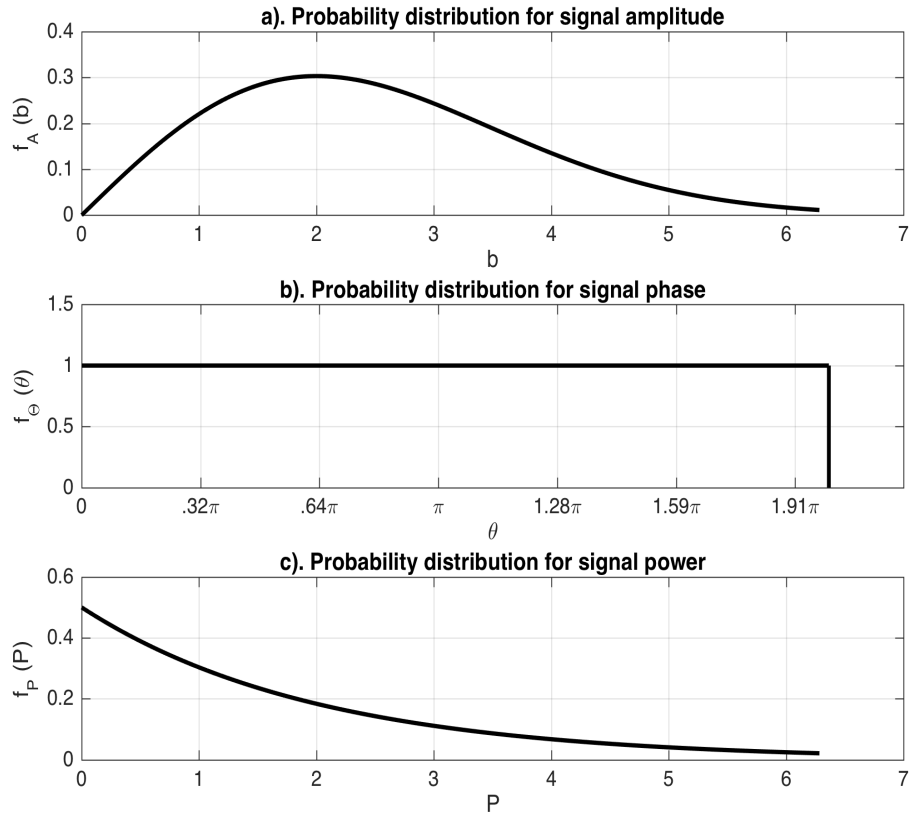


Figure 4.14: Signal features distributions: a) Rayleigh distribution for amplitude. b) Uniform distribution for phase. c) Exponential distribution for power.

Chapter 5 : Results and comments

5.1. Synthetic signals

The generated signals mimic the real phased array radar signals as follows:

- Length of sequences: $M = 40$ samples,
- Wavelength: $\lambda = 0.0937$ m,
- Sampling period: $T_s = 0.984$ ms,
- Maximum non-ambiguous radial velocity: $V_a = \frac{\lambda}{4T_s} = 23.81$ m/s,
- Peak power: $P_{peak} = 750$ KW.

To compute periodograms, the FFT algorithm is needed, so zero-padding of the sequences (of length 40) to 64 points is mandatory to achieve spectra calculation.

Through all the following figures depicting spectral width σ_v , in some cases, estimated values are erroneous and because of that the continuity of the corresponding curve is disrupted as in Figure 5.8, Figure 5.10 and Figure 5.12. This phenomenon is more evident in Figure 5.15 and Figure 5.17.

5.1.1. Generation of weather sequences

In this section, the following curves, each of which represents time series (Top) and corresponding spectrum (Bottom), are obtained under these circumstances:

- Spectral width: $\sigma_v = 2$ m/s,
- Radial velocity: $V_D = -15$ m/s,
- $SNR = -5, +2, +15$ in Figure 5.3, Figure 2.3 and Figure 5.1 respectively.

Visually, spectra are more talkative than counter-part time series. All of the spectra

in the bottom of illustrations Figure 5.3, Figure 2.3 and Figure 5.1 are centered at the Doppler velocity particularly on high SNR. In some cases, spectrum is bimodal or even more. Ground clutter can be located and centered at zero Doppler in addition to weather spectrum as it is illustrated by Figure 5.4. Therein, the red curve (Bottom) depicts the ideal spectrum whereas the blue curve is the actual spectrum.

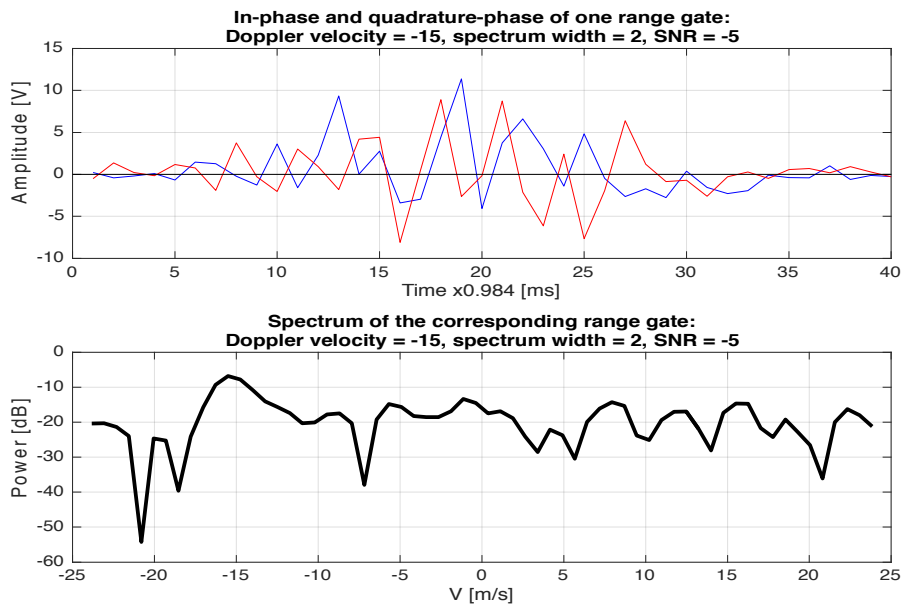


Figure 5.1: Simulated time series of 40 samples and the corresponding spectrum for $V_D = -15 \text{ m/s}$, $\sigma_v = 2 \text{ m/s}$ and $\text{SNR} = -5$.

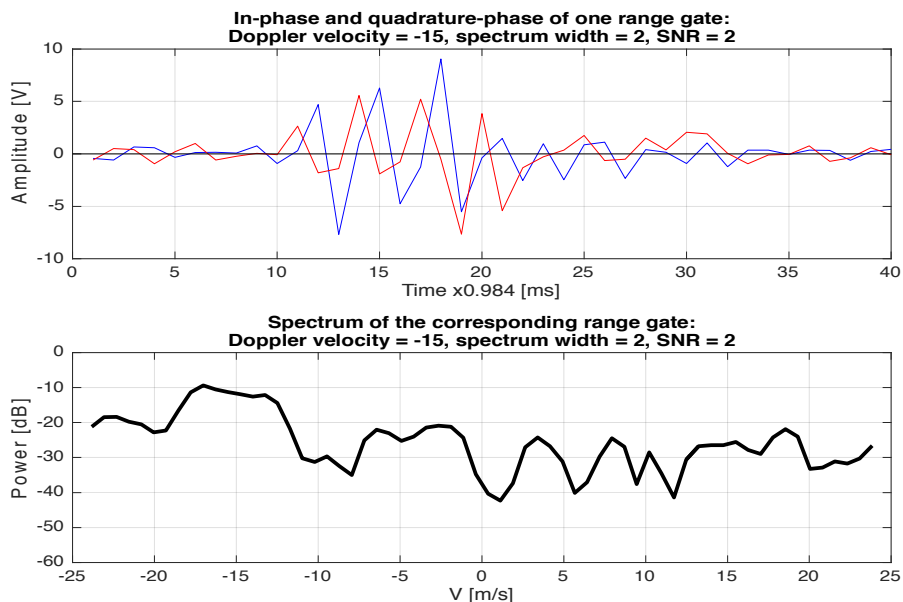


Figure 5.2: Simulated time series of 40 samples and the corresponding spectrum for $V_D = -15 \text{ m/s}$, $\sigma_v = 2 \text{ m/s}$ and $\text{SNR} = 2$.

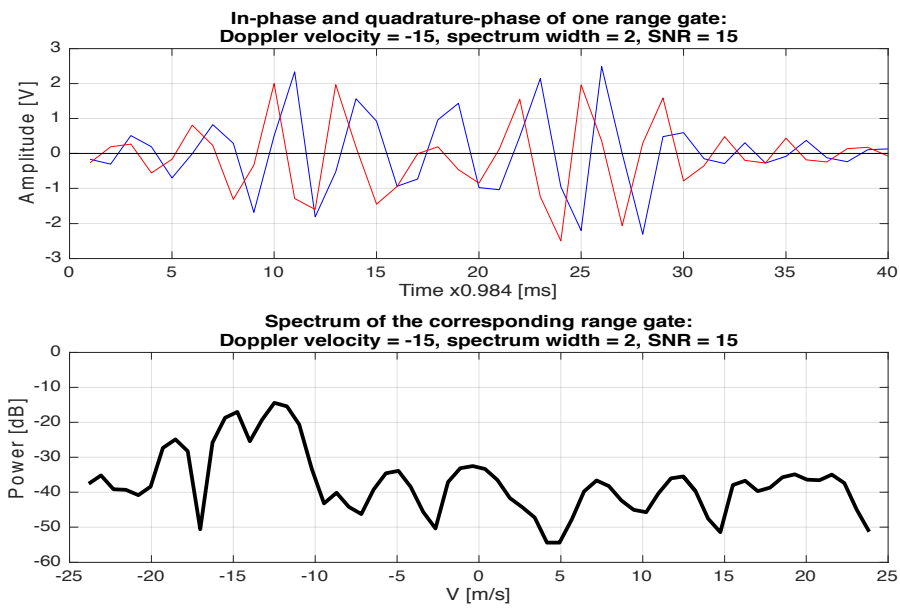


Figure 5.3: Simulated time series of 40 samples and the corresponding spectrum for $V_D = -15 \text{ m/s}$, $\sigma_v = 2 \text{ m/s}$ and $\text{SNR} = 15$.

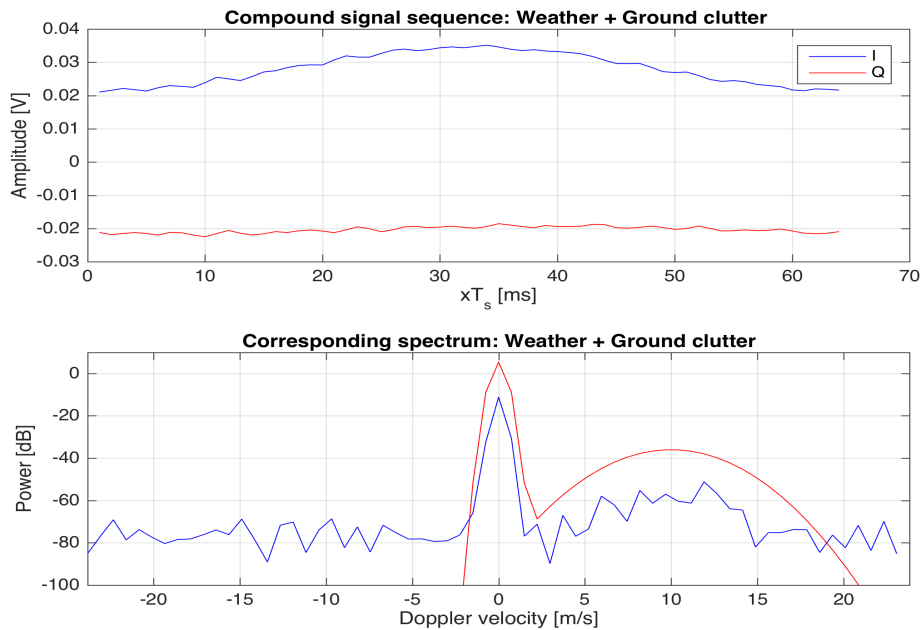


Figure 5.4: Bimodal signal composed of weather centered at 10 m/s and ground clutter centered at zero Doppler. The red curve (Bottom) depicts the ideal spectrum whereas the blue curve is the actual spectrum.

5.1.2. Statistical properties of weather sequences

In this section, complex sequences IQ are assumed to be ground clutter free

and only weather return is considered. Both parts, real and imaginary, of weather complex sequences comply with theory (Central limit theorem). The distribution is Gaussian Figure 5.5.a Figure 5.5.b. In addition, both parts are uncorrelated , $cov(real(IQ), imag(IQ)) = 0$, as it is shown by the scatter plot in Figure 5.6.

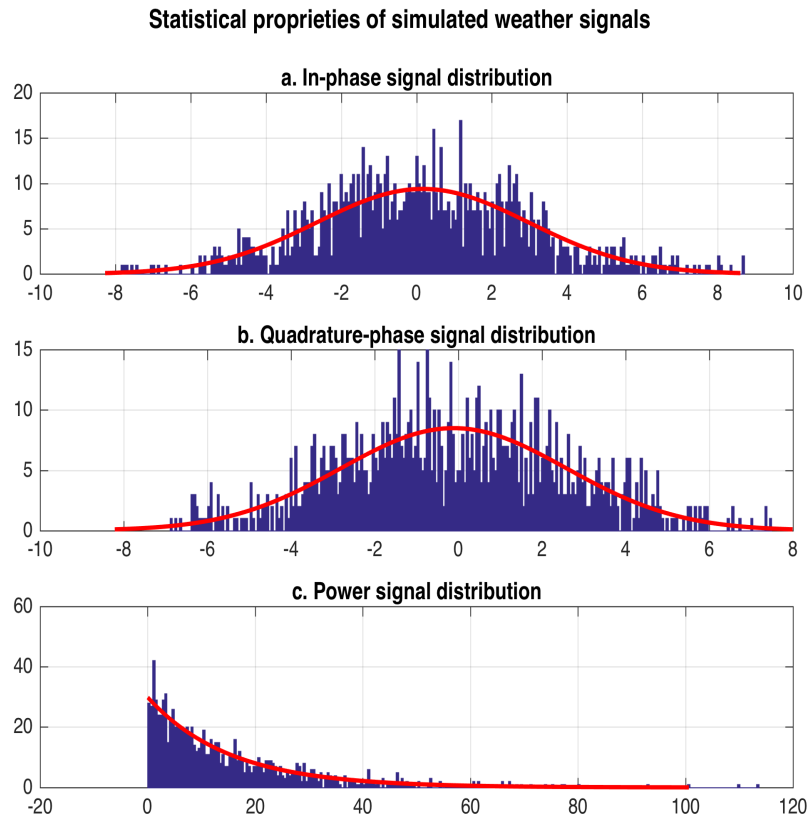


Figure 5.5: Statistical properties of a simulated sequence.

5.1.3. Denoising using lifted wavelets and optimum threshold

The following set of figures (from Figure 5.7 to Figure 5.12) depicts the performance of standard algorithm (blue curves), Lifted Wavelet Transform in conjunction with Universal Threshold LWT-UT (green curves) and Lifted Wavelet Transform in conjunction with an Adaptive Threshold LWT-AT (red curves) through the first and the second spectral moments estimation (V_D and σ_v).

For any Doppler radial velocity in the Nyquist interval, $[-V_a:V_a] = [-23.81:23.81]$ m/s, as a true velocity (black slanting line), the corresponding estimate using LWT-UT (blue curve) or without any treatment (green curve) is very poor for low SNR ($SNR < 10$). This is depicted in Figure 5.7 and Figure 5.9. But for higher SNR, $SNR > 15$,

the corresponding estimates are considerably enhanced as shown in Figure 5.11. So it is for the estimates of spectrum width σ_v that are enhanced only for high SNR.

But one can notice very clearly that the proposed method LWT-AT (red curve) outperforms the LWT-UT method (green curve) in estimating both the Doppler radial velocity V_D and spectrum width σ_v whatever may be the SNR value as shown in Figure 5.7 through Figure 5.12 where $SNR = -5, +2, +15$.

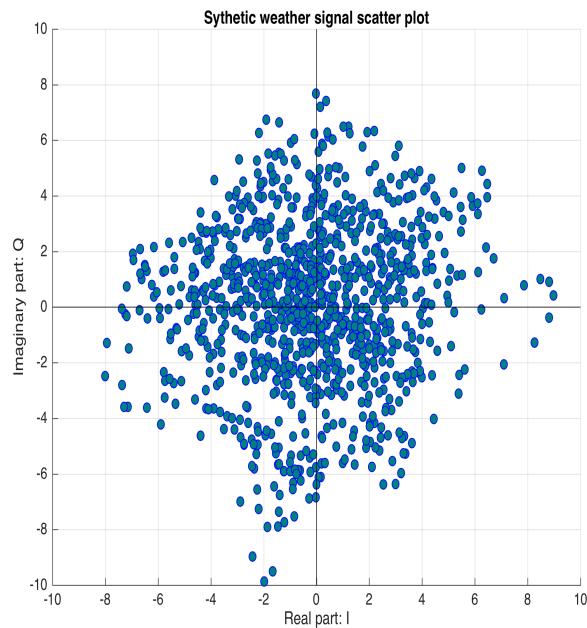


Figure 5.6: Scatter plot of quadrature-phase vs in-phase of a simulated weather sequence.

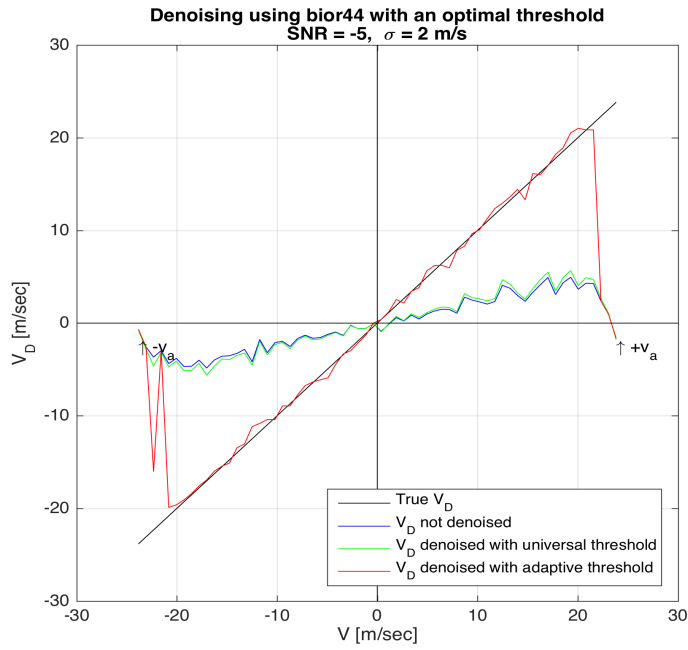


Figure 5.7: Doppler Radial velocity: Denoising of simulated signals (throughout Nyquist interval) for $SNR=-5$, $\sigma_v=2m/s$, using the standard LWT in green and the proposed algorithm in red.

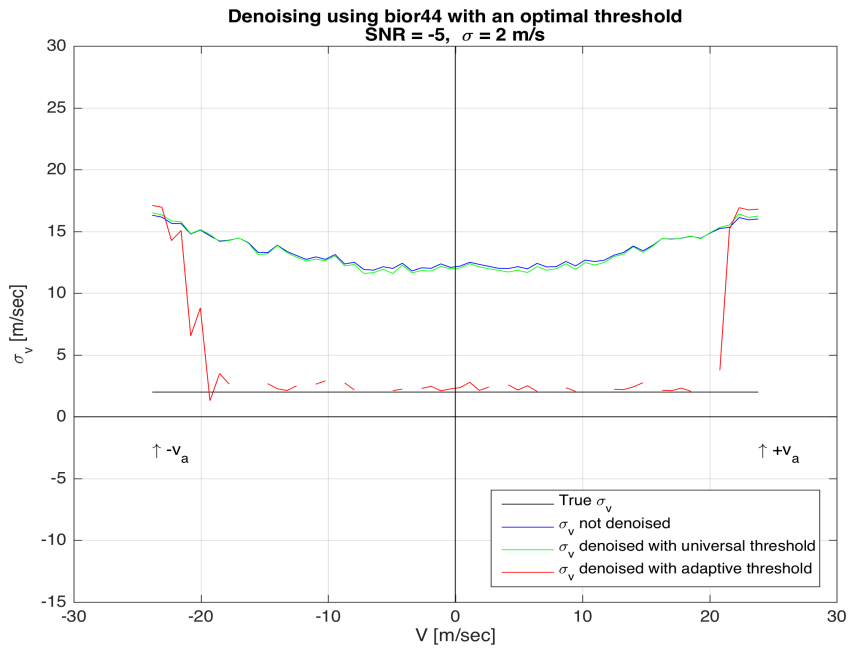


Figure 5.8: Spectrum width: Denoising of simulated signals (throughout Nyquist interval) for $SNR=-5$, $\sigma_v=2m/s$, using the standard LWT in green and the proposed algorithm in red.

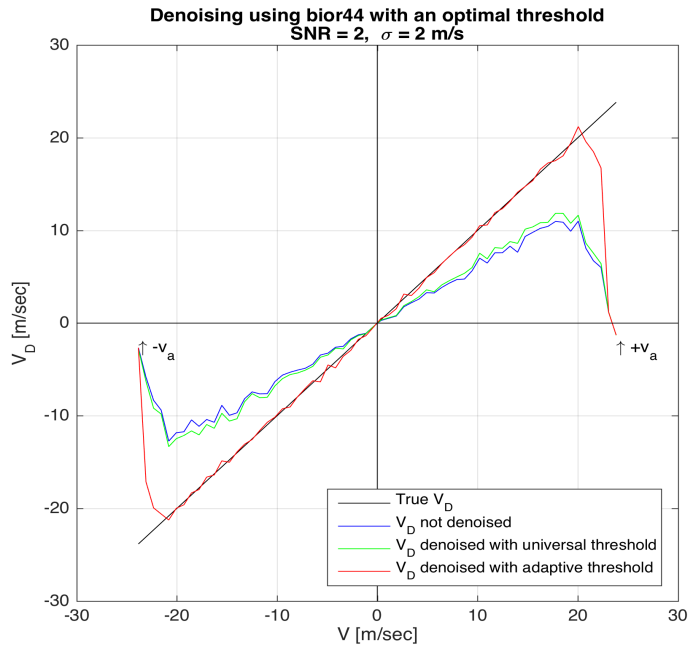


Figure 5.9: Doppler Radial velocity: Denoising of simulated signals (throughout Nyquist interval) for $SNR=2$, $\sigma_v=2m/s$, using the standard LWT in green and the proposed algorithm in red.

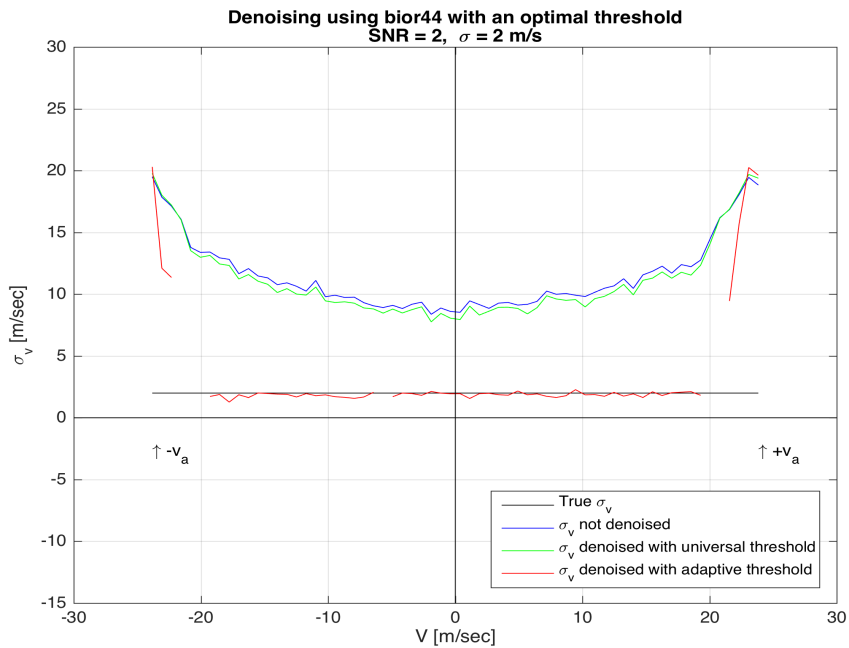


Figure 5.10: Spectrum width: Denoising of simulated signals (throughout Nyquist interval) for $SNR=2$, $\sigma_v=2m/s$, using the standard LWT in green and the proposed algorithm in red.

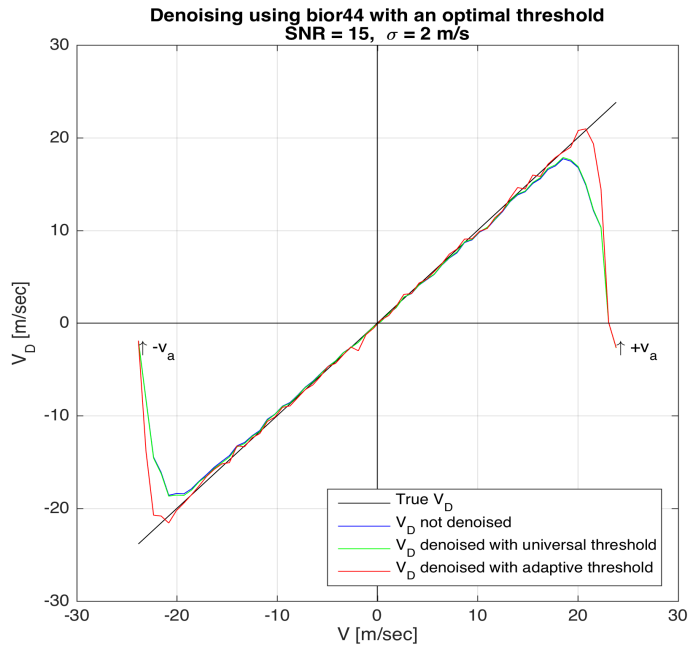


Figure 5.11: Doppler Radial velocity: Denoising of simulated signals (throughout Nyquist interval) for $SNR=15$, $\sigma_v=2\text{ m/s}$, using the standard LWT in green and the proposed algorithm in red.

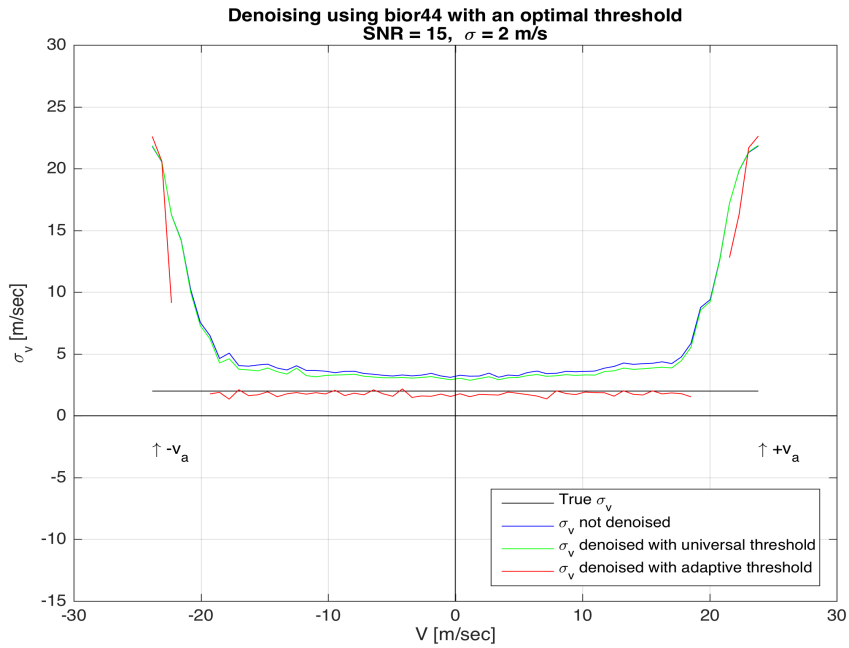


Figure 5.12: Spectrum width: Denoising of simulated signals (throughout Nyquist interval) for $SNR=15$, $\sigma_v=2\text{ m/s}$, using the standard LWT in green and the proposed algorithm in red.

5.1.4. Denoising using Hildebrand and Sekhon algorithm

In the current section, previous considerations are reproduced (V_D spans from

$-V_a = -23.81$ m/s to $+V_a = +23.81$ m/s, $SNR = -5, +2, +15$ and $\sigma_v = 2$ m/s) to test the efficiency of an old method proposed by Hildebrand and Sekhon (HS) to objectively estimate Gaussian noise level in spectra.

It turned out that HS method does an acceptable job on low SNRs to estimate radial velocity V_D as it is shown in Figure 5.14 and Figure 5.16 but wouldn't say as much about spectrum width estimate for the same low SNRs values as it is depicted by the Figure 5.15 and Figure 5.17 where most of the values are discarded because they are erroneous.

For high SNR values (>15), HS algorithm is very efficient. The result is shown in Figure 5.18 for the radial velocity V_D and in Figure 5.19 for the spectrum width σ_v .

The performance of HS algorithm is shown in Figure 5.13 through simulated radar signals. As input, noisy weather sequence is plugged in (varying noise level) from $SNR = -10$ to $SNR = 50$ and the output of the algorithm is the estimated noise level from the calculated corresponding spectrum of the sequence.

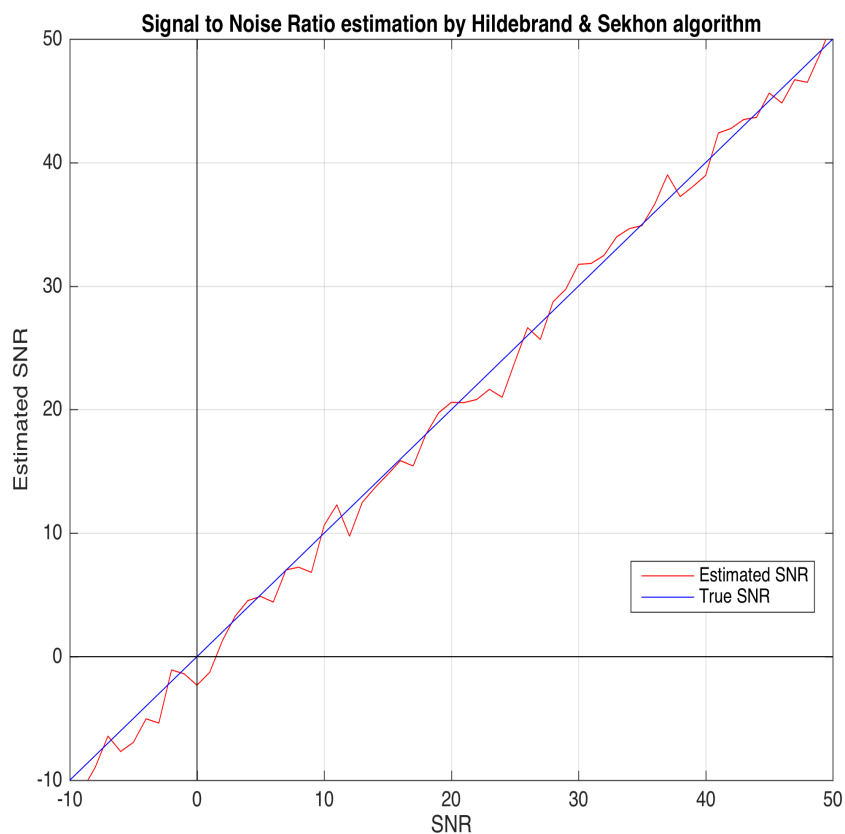


Figure 5.13: Hildebrand & Sekhon algorithm performance.

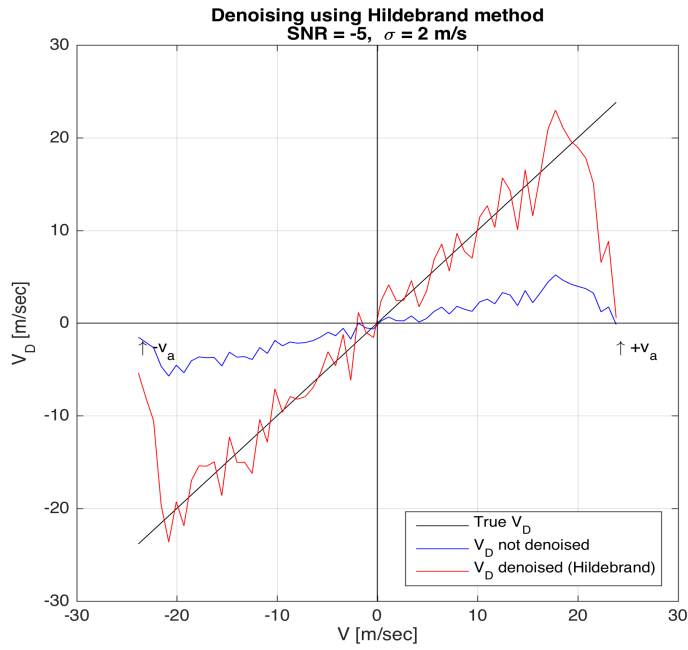


Figure 5.14: Doppler Radial velocity: Denoising of simulated signals (throughout Nyquist interval) for $SNR=-5$, $\sigma_v=2m/s$, using the Hildebrand & Sekhon algorithm in red.

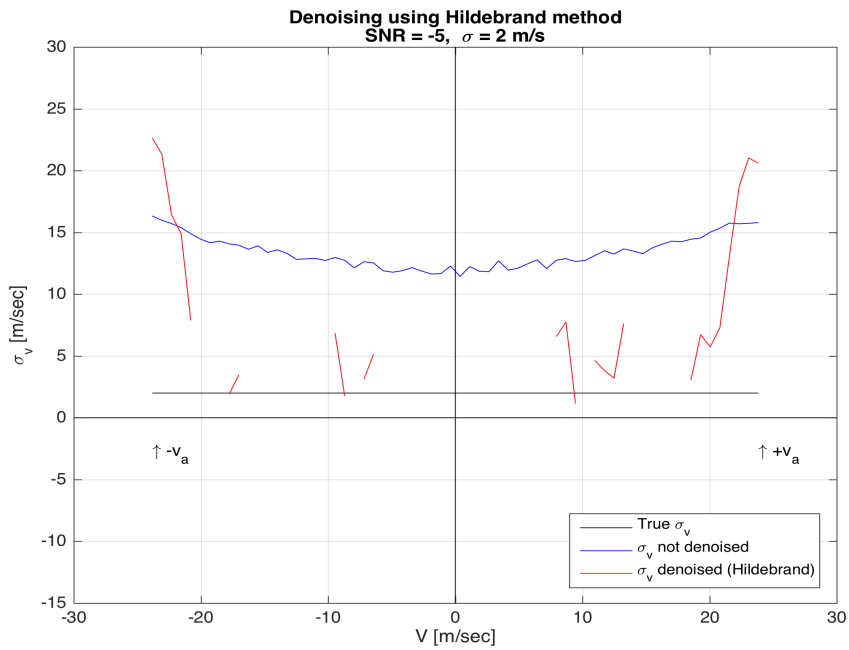


Figure 5.15: Spectrum width: Denoising of simulated signals (throughout Nyquist interval) for $SNR=-5$, $\sigma_v=2m/s$, using the Hildebrand & Sekhon algorithm in red.

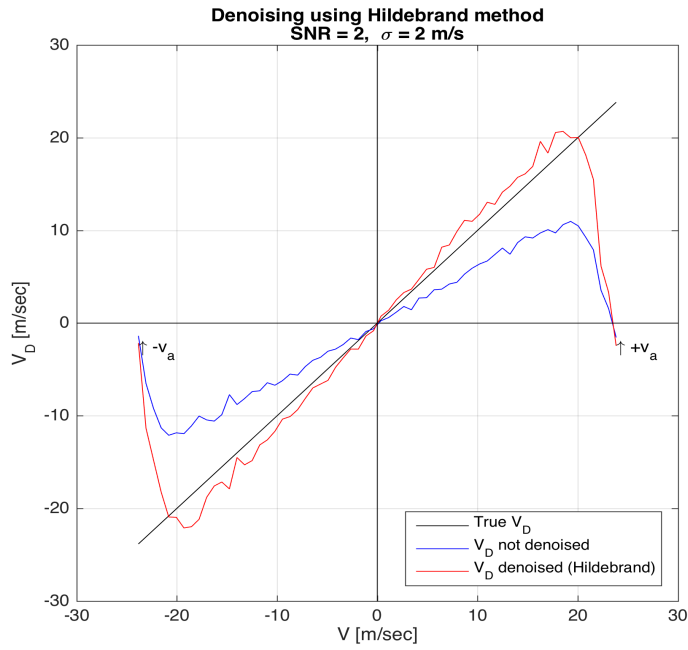


Figure 5.16: Doppler Radial velocity: Denoising of simulated signals (throughout Nyquist interval) for $SNR=2$, $\sigma_v=2m/s$, using the Hildebrand & Sekhon algorithm in red.

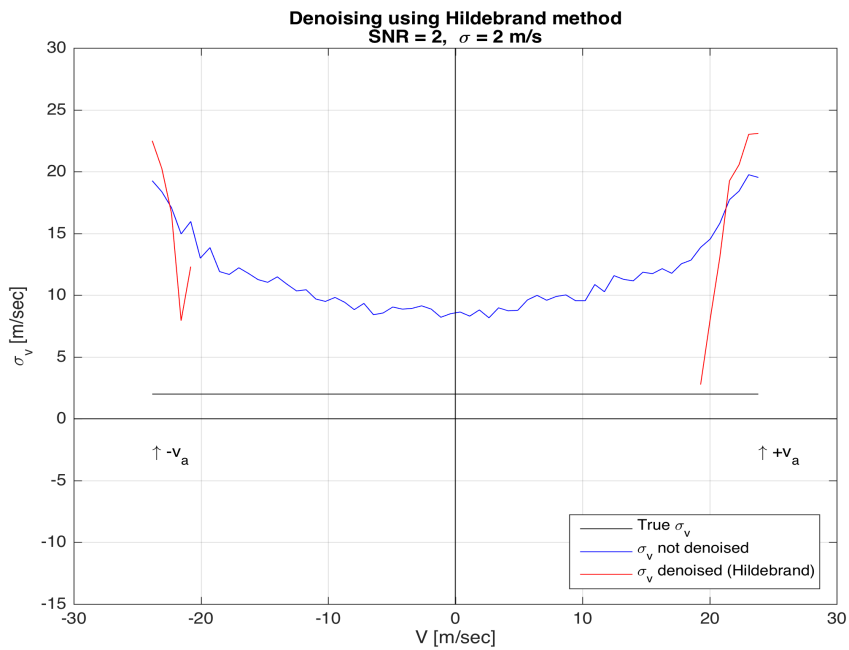


Figure 5.17: Spectrum width: Denoising of simulated signals (throughout Nyquist interval) for $SNR=2$, $\sigma_v=2m/s$, using the Hildebrand & Sekhon algorithm in red.

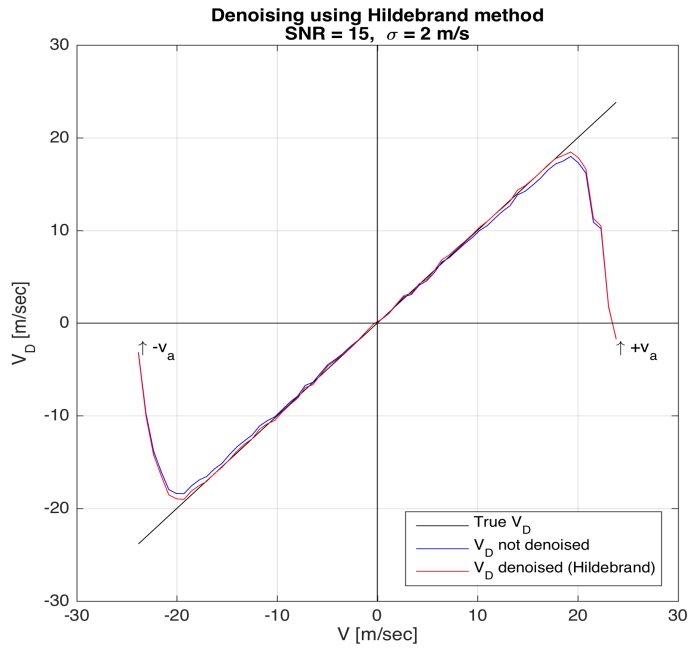


Figure 5.18: Doppler Radial velocity: Denoising of simulated signals (throughout Nyquist interval) for $SNR=15$, $\sigma_v=2m/s$, using the Hildebrand & Sekhon algorithm in red.

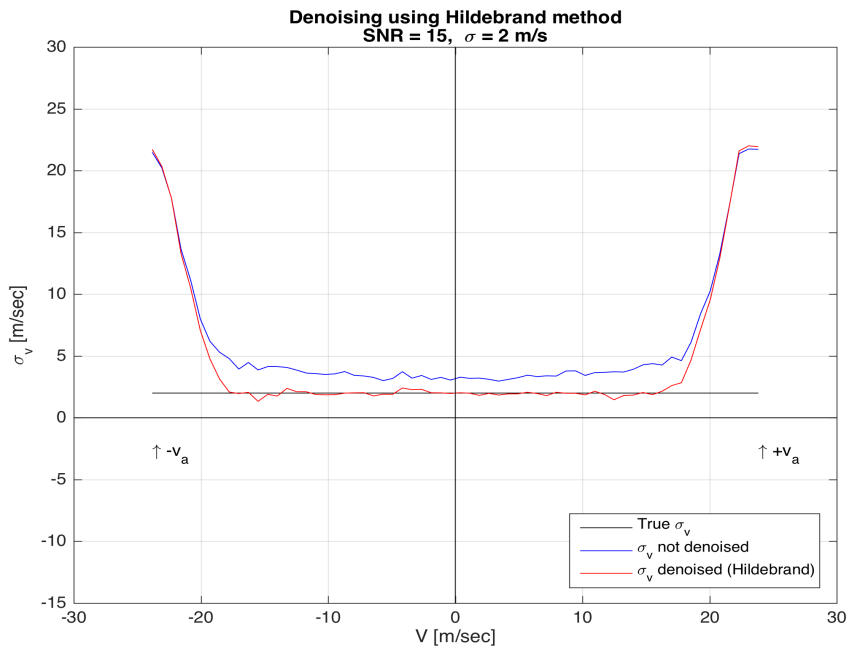


Figure 5.19: Spectrum width: Denoising of simulated signals (throughout Nyquist interval) for $SNR=15$, $\sigma_v=2m/s$, using the Hildebrand & Sekhon algorithm in red.

5.1.5. Comparison

In this section, comparison between LWT-AT method performance and HS method

performance is carried out. Previous conditions are also reused here to test the efficiency

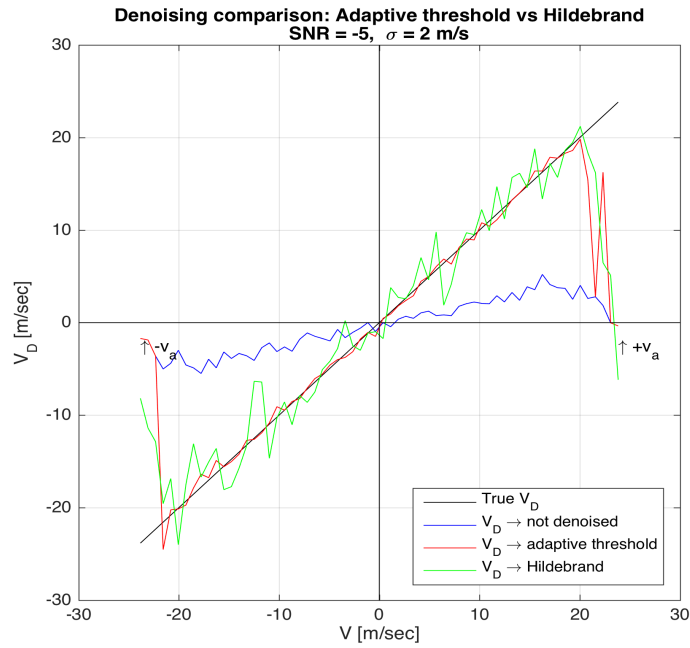


Figure 5.20: Doppler Radial velocity: Comparison in denoising of simulated signals (throughout Nyquist interval) for , SNR=-5 , using the proposed algorithm in red and the Hildebrand & Sekhon algorithm in green.

of both algorithms.

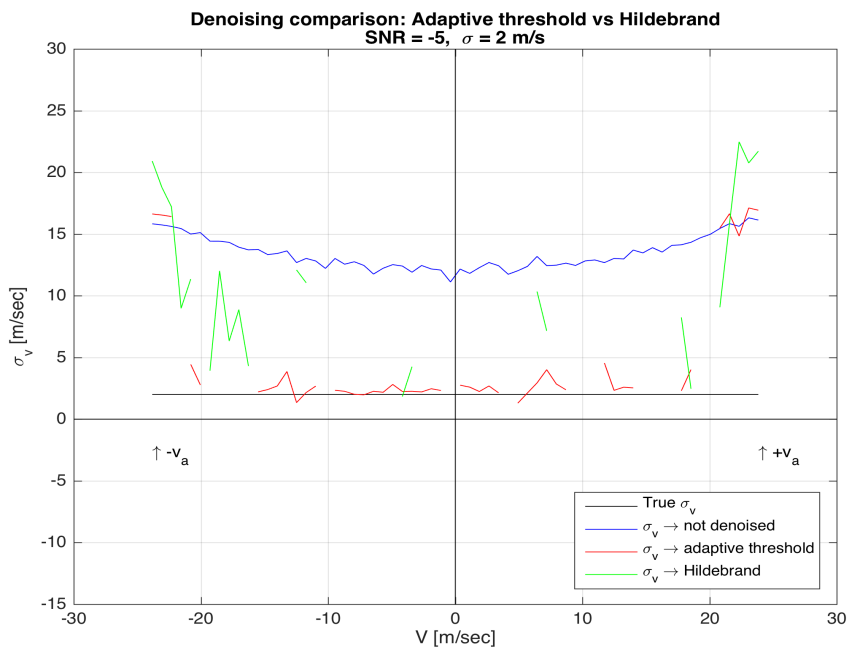


Figure 5.21: Spectrum width: Comparison in denoising of simulated signals (throughout Nyquist interval) for , SNR=-5 , using the proposed algorithm in red and the Hildebrand & Sekhon algorithm in green.

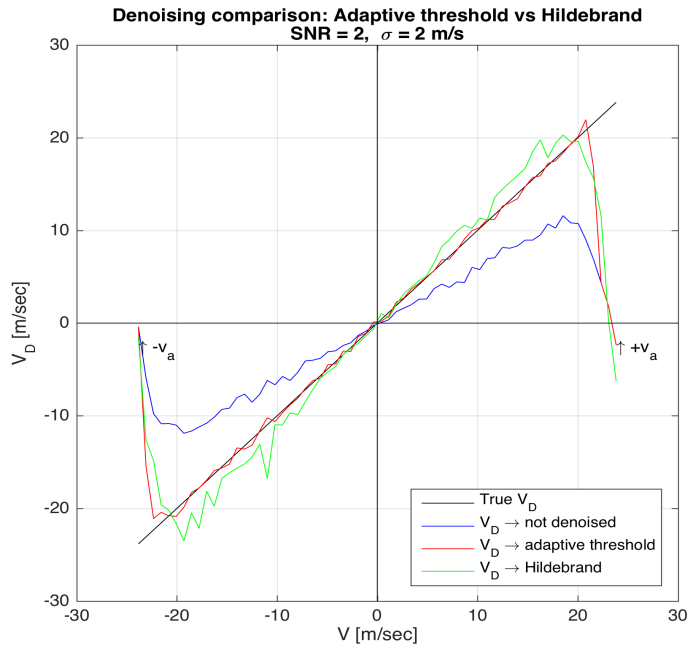


Figure 5.22: Doppler Radial velocity: Comparison in denoising of simulated signals (throughout Nyquist interval) for , $SNR=2$, using the proposed algorithm in red and the Hildebrand & Sekhon algorithm in green.

Clearly, it is shown that the proposed method (LWT-AT) outperforms the counterpart HS method in all the testing conditions (regarding the SNR value) particularly in low SNRs. For higher values of the SNR, performance of both methods are almost alike with a slight superiority of the LWT-AT method as it is depicted in Figure 5.24 for the velocity and in Figure 5.25 for the spectrum width.

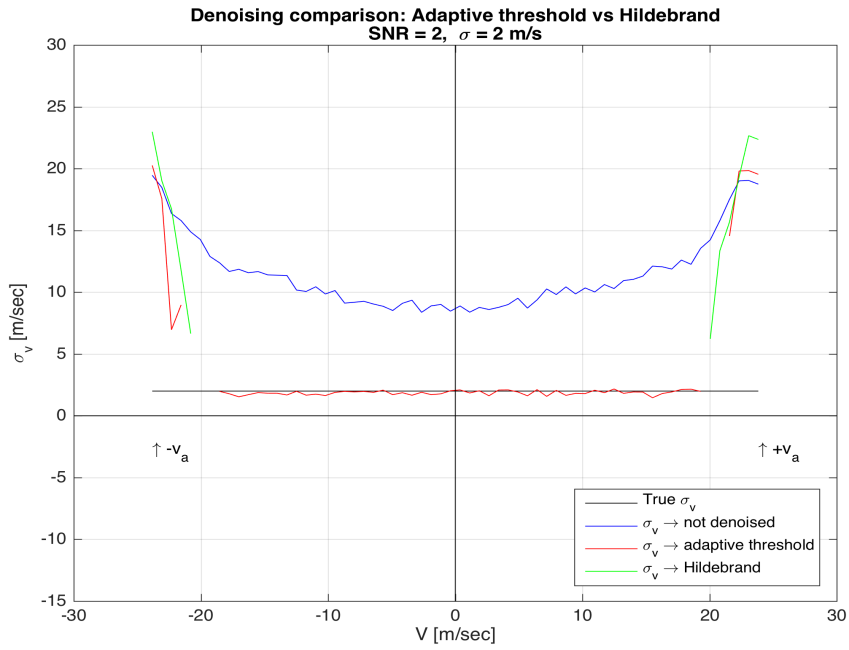


Figure 5.23: Spectrum width: Comparison in denoising of simulated signals (throughout Nyquist interval) for , SNR=2 , using the proposed algorithm in red and the Hildebrand & Sekhon algorithm in green.

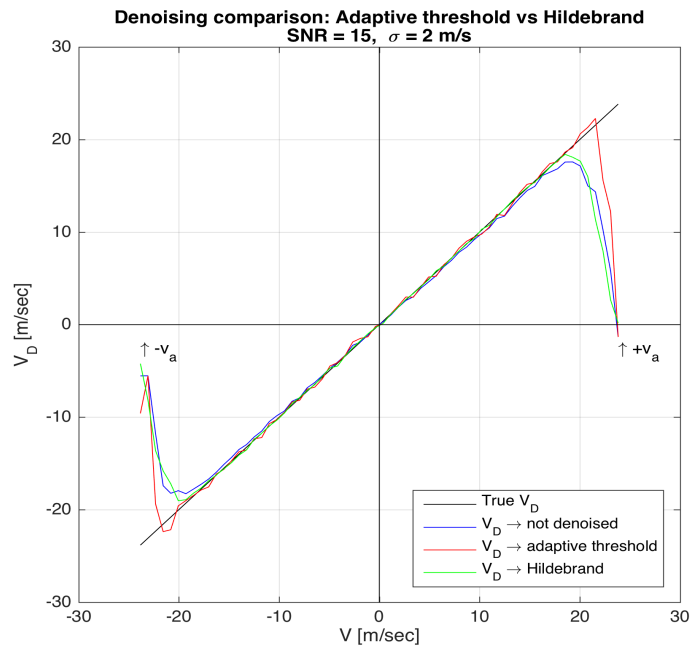


Figure 5.24: Doppler Radial velocity: Comparison in denoising of simulated signals (throughout Nyquist interval) for , SNR=15 , using the proposed algorithm in red and the Hildebrand & Sekhon algorithm in green.

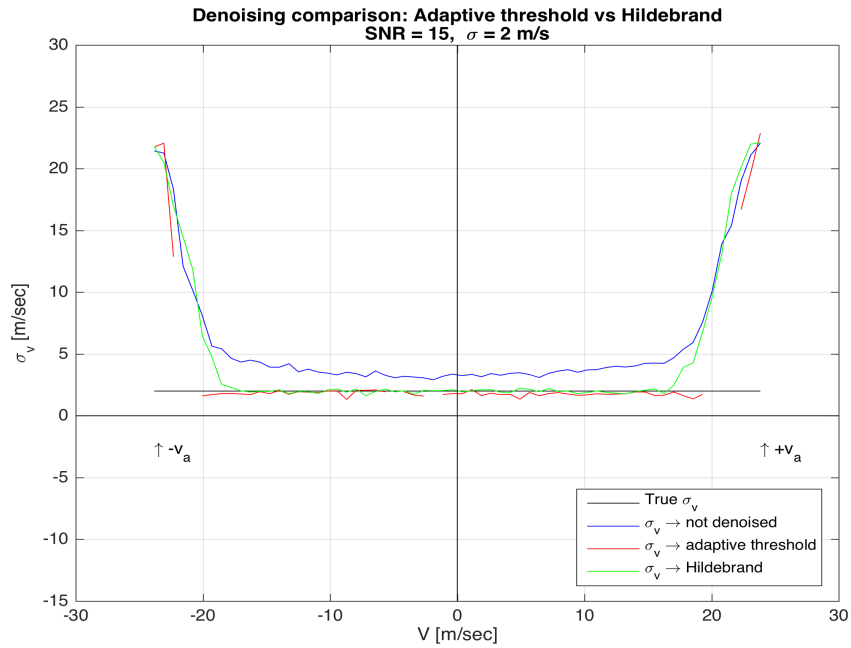


Figure 5.25: Spectrum width: Comparison in denoising of simulated signals (throughout Nyquist interval) for , $SNR=15$, using the proposed algorithm in red and the Hildebrand & Sekhon algorithm in green.

5.2. Actual data

5.2.1. Representation of weather sequences

In Figure 5.26 and Figure 5.28, true radar signals corresponding to range cells #380 and #432 respectively. Both are extracted from the same radial #109 of the aforementioned phased array radar.

Accordingly, Figure 5.29 and Figure 5.27 depict the corresponding spectra. One can speculate that both spectra are noisy because of the presence of skirt-like shape in the base all over the Nyquist interval. The first spectrum (#380) is centered at 10 m/s and the second one (#432) is centered at 14 m/s.

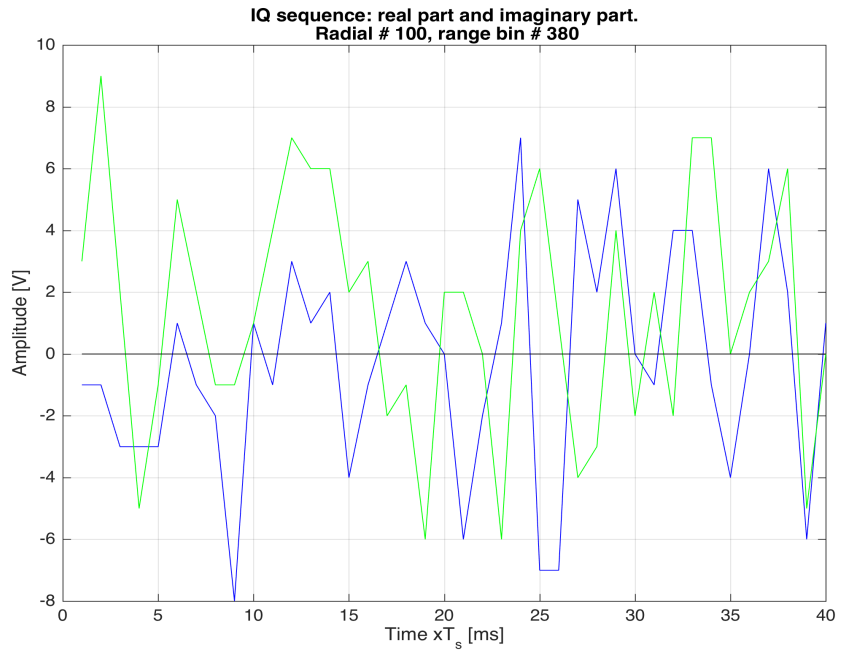


Figure 5.26: Time series: Real radar signal corresponding to range cell #380 from the radial #109.

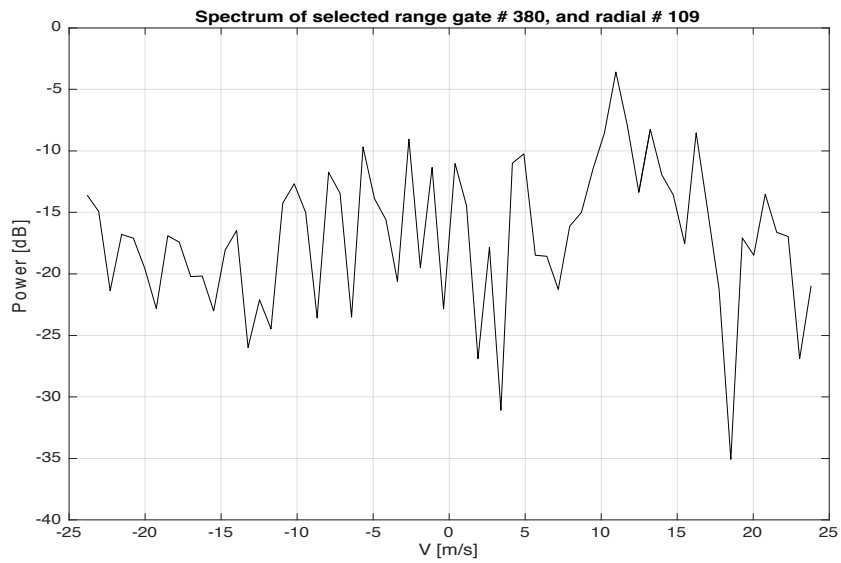


Figure 5.27: Spectrum of time series: Real radar signal corresponding to range cell #380 from the radial #109.

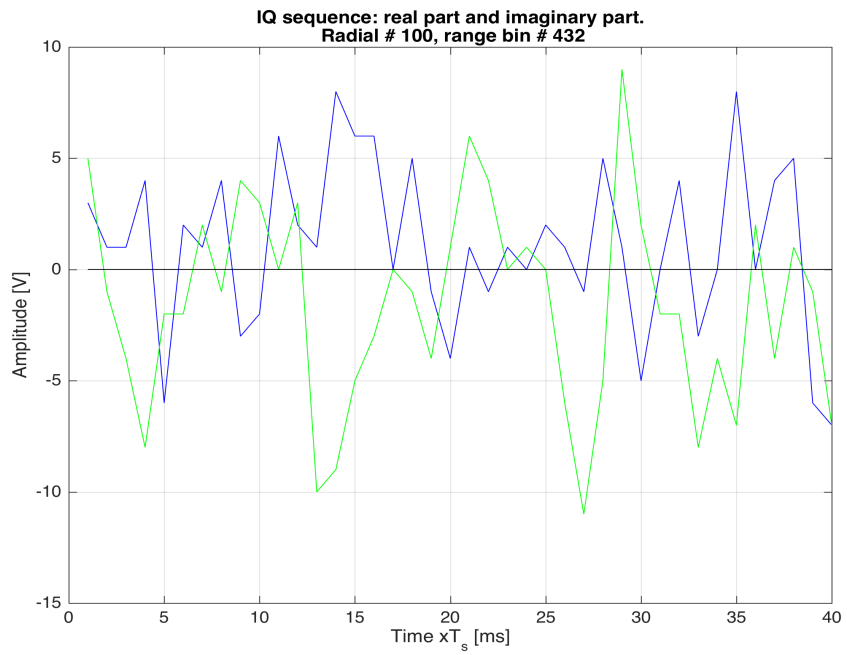


Figure 5.28: Time series: Real radar signal corresponding to range cell #432 from the radial #109.

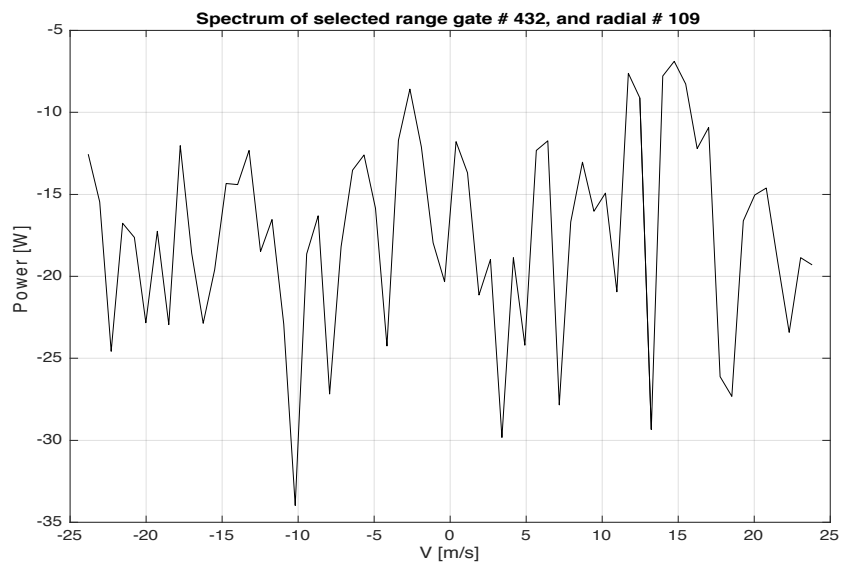


Figure 5.29: Spectrum of time series: Real radar signal corresponding to range cell #432 from the radial #109.

5.2.2. Statistical properties of real radar signals

As an illustration, range bin #380 of the radial #109 is considered and depicted by the Figure 5.30. All of the tested range gates signals of the real radar data in our hands have shown their statistical properties as in Figure 5.32.

Both in-phase and quadrature-phase signals distributions are Gaussians centered at zero. There is no correlation between both signals as it is depicted by the scatter plot in Figure 5.31.

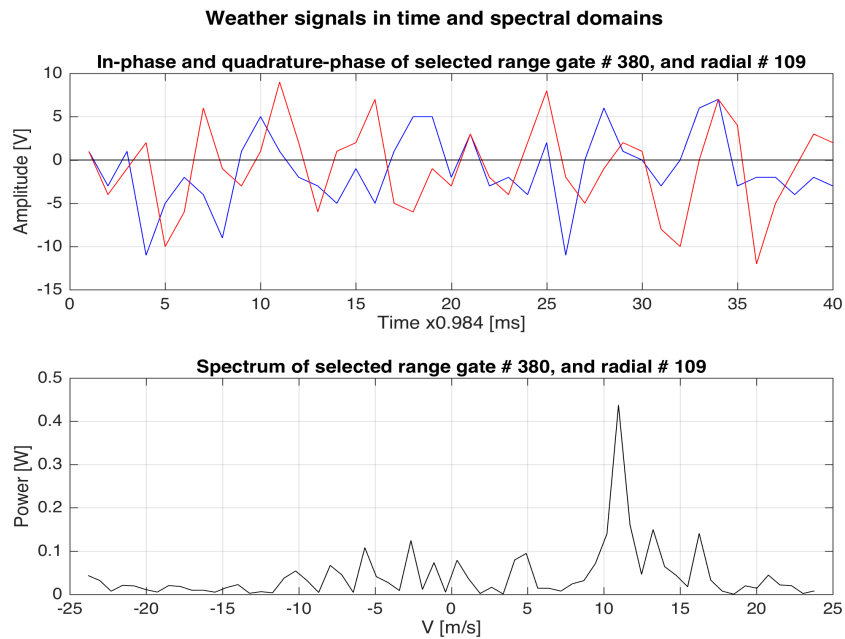


Figure 5.30: Real phased array radar signal and the corresponding spectrum (Range bin #380 from radial #109).

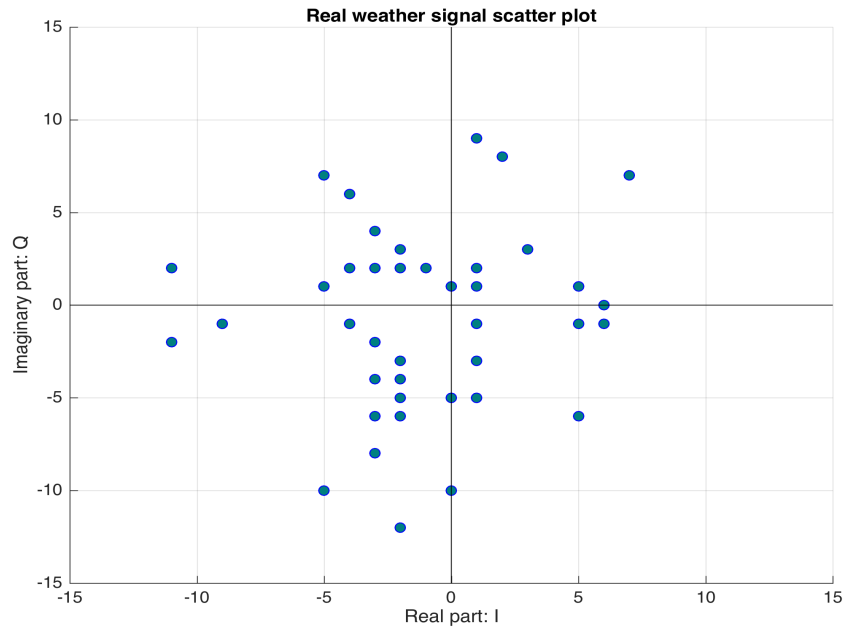


Figure 5.31: Scatter plot of a real signal corresponding to range bin #380 from radial #109.

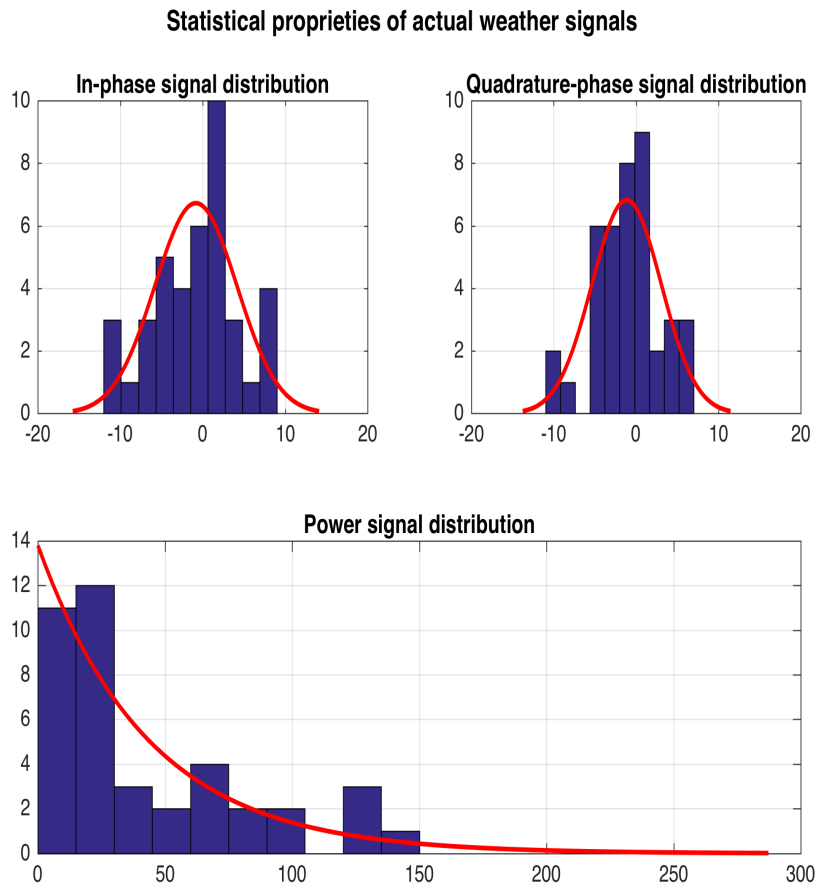


Figure 5.32: Statistical properties of a selected range bin sequence from the radial #109.

5.2.3. Denoising using lifted wavelets and optimum threshold

through the following figures of this section, Figure 5.34 to Figure 5.37, where Figure 5.34 and Figure 5.35 correspond to radial velocity and spectrum width of an excerpt from radial #1 (uttermost left of the sector shown in Figure 5.38), from range bin #70 to range bin #249 and Figure 5.36 along with Figure 5.37 correspond to radial velocity and spectrum width of another excerpt from radial #100 (uttermost right of the sector shown in Figure 5.38), from range bin #350 to range bin #549.

On these two sets of data, the proposed method (LWT-AT) is applied. The results show that the performance of the proposed algorithm on the data looks like selective (acts on some areas and not on others) but it is not the case. This rather shows that the noise level is not the same even along one single azimuth (radial). That's why when there is noise the estimated velocity has increased and the estimated spectrum width has decreased.

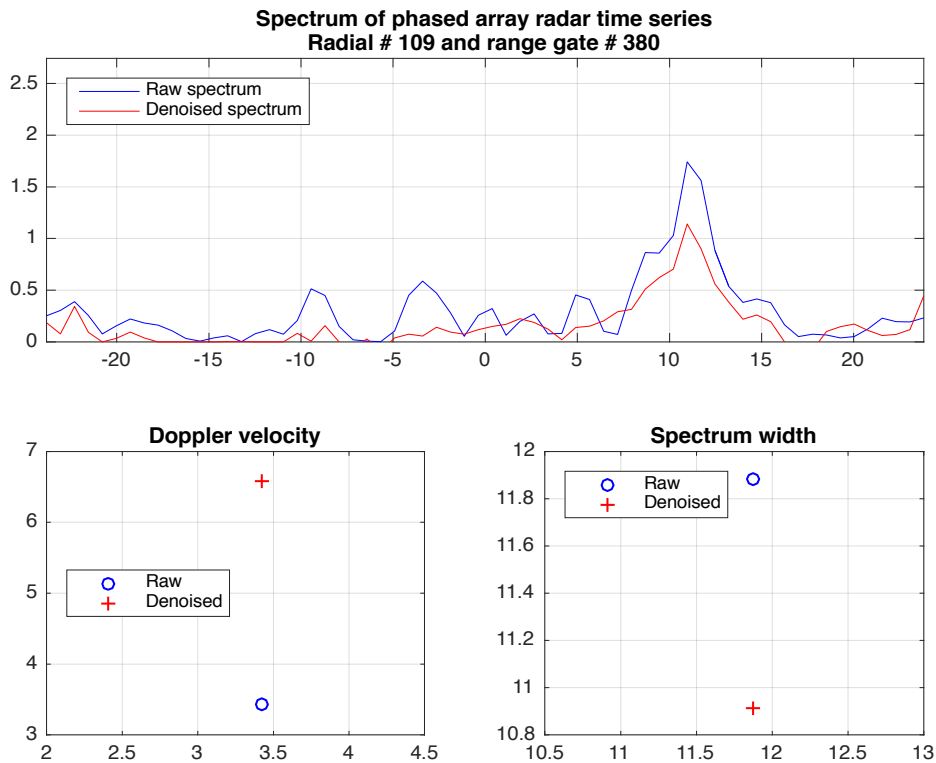


Figure 5.33: Performance of the proposed algorithm on real data to estimate the spectrum, radial Doppler velocity and spectrum width of the range bin #380 (radial #109)

The high performance of the adaptive threshold is shown on one single range bin

(range bin #380 of radial #109) where both spectra (raw and denoised) are represented on top of Figure 5.33 and Doppler velocity along with the corresponding spectrum width are depicted as well. Doppler velocity has increased from 3.43 m/s to 6.57 m/s. Regarding spectrum width, it has decreased from 11.88 m/s to 10.92 m/s as it is expected in presence of noise.

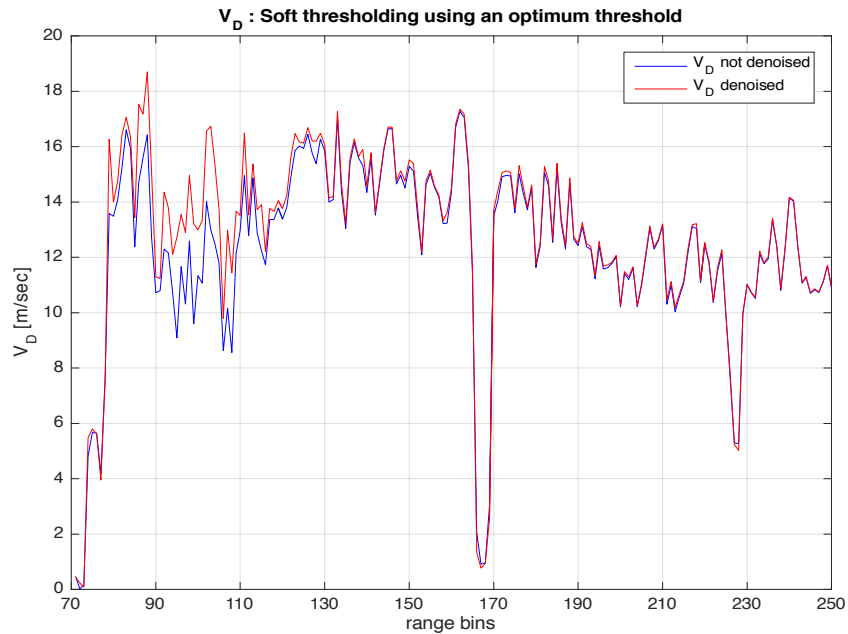


Figure 5.34: Performance of the proposed algorithm on real data to estimate the radial Doppler velocity from range bin #70 to range bin #249.

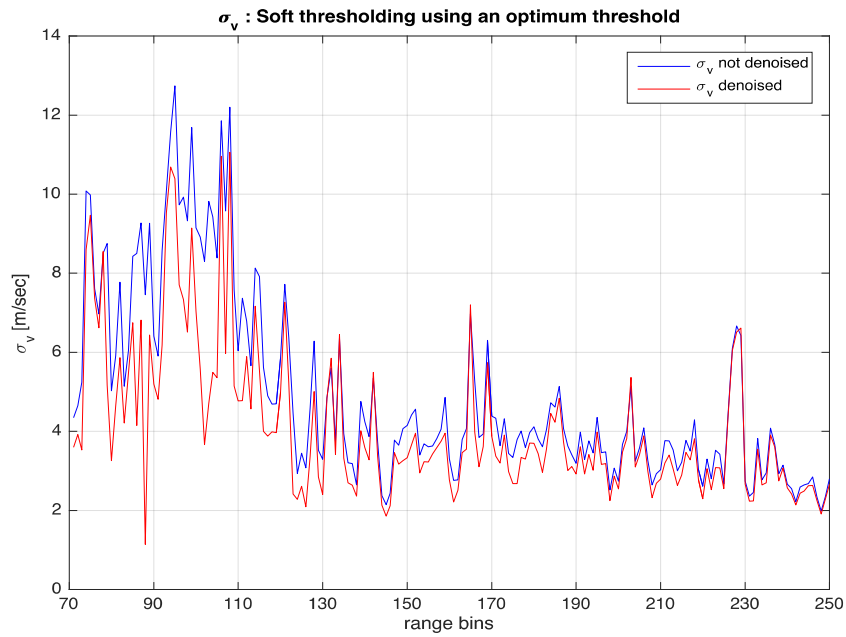


Figure 5.35: Performance of the proposed algorithm on real data to estimate the corresponding spectrum width from range bin #70 to range bin #249.

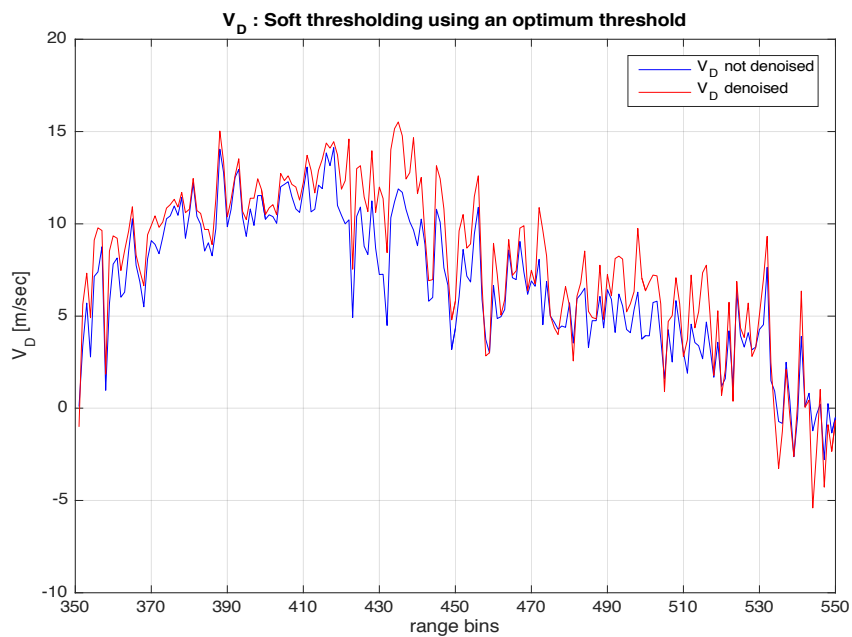


Figure 5.36: Performance of the proposed algorithm on real data to estimate the radial Doppler velocity from range bin #350 to range bin #549.

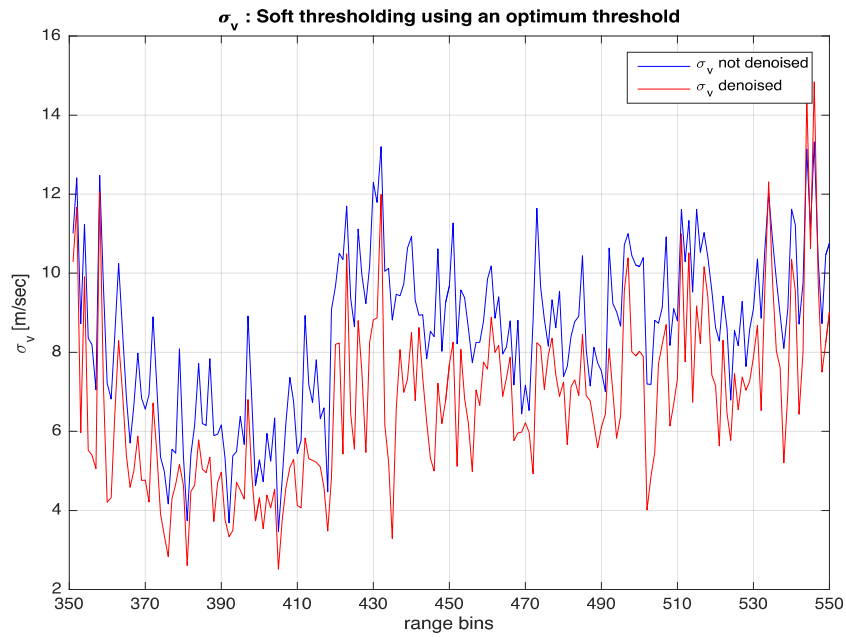


Figure 5.37: Performance of the proposed algorithm on real data to estimate the corresponding spectrum width from range bin #350 to range bin #549.

5.2.4. Global view of real data

The Figure 5.39 shows the filtered PPI view for reflectivity obtained by the proposed method using the data from the phased array weather radar testbed located in Norman (close to Oklahoma City in Oklahoma State, USA) and shown in Figure 5.38.

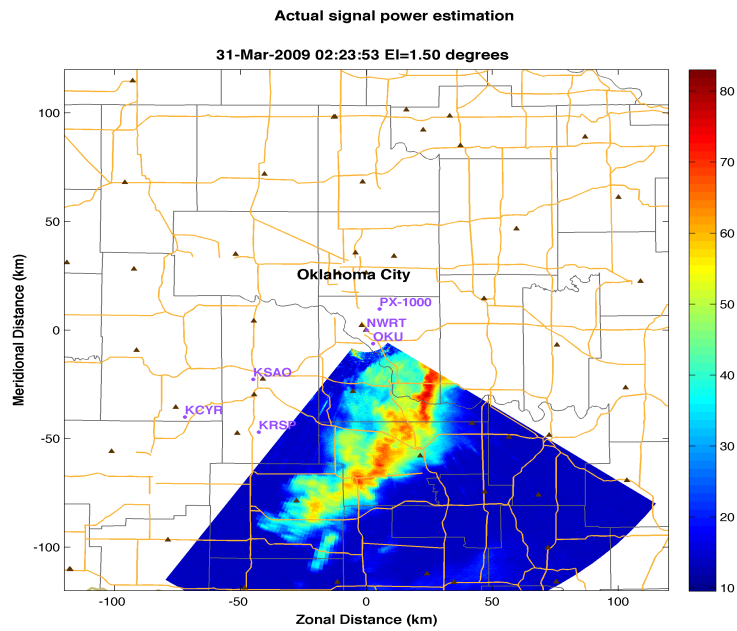


Figure 5.38: Sectorial view of real data from the phased array weather radar located in Norman, OK (USA).

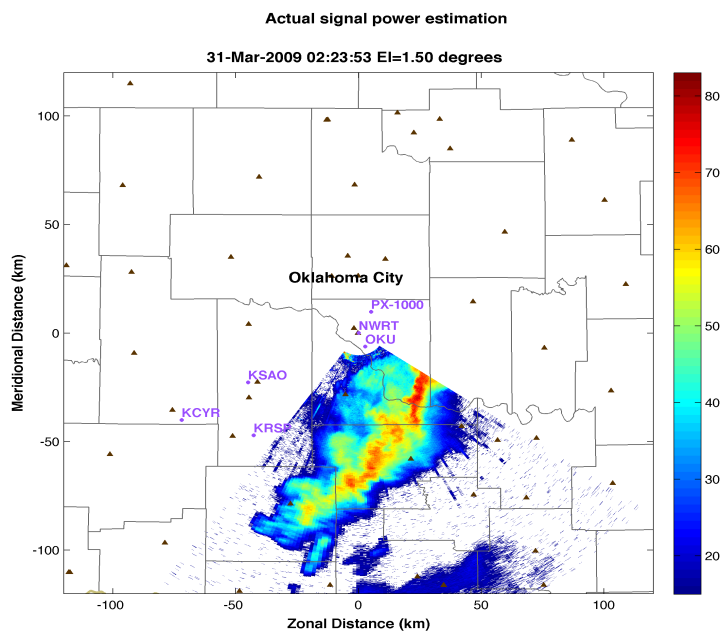


Figure 5.39: Filtered real data from the phased array weather radar located in Norman, OK (USA).

A comparison of results obtained by two different radars closely to each other is carried out. The closest radar to the phased array radar located in Norman is KTLX which belongs to the National Weather Service radars network. It is located in North West at 20 km (in a straight line) from Norman as it is shown by Figure 5.40.

The available data from the phased array radar is picked up at 02:23:53 but the

data available from KTLX radar is picked up at 02:22:47 (one minute earlier). The two views illustrated by Figure 5.38 and Figure 5.41 are alike despite the minute gap.

Therefore, one can infer that the velocity of the weather perturbation is not high. So the two sets of data from the two radars are comparable.

In Figure 5.42, the grid is narrower than the one in Figure 5.41. It complies with the one in the Figure 5.38 corresponding to the phased array radar located in Norman.

The Figure 5.43 depicts a projection onto Google Earth of the gridded view of the Figure 5.42 through a kmz file (Google Earth file format) created by the Weather Toolkit of the federal agency NOAA (*National Oceanic and Atmospheric Administration*).

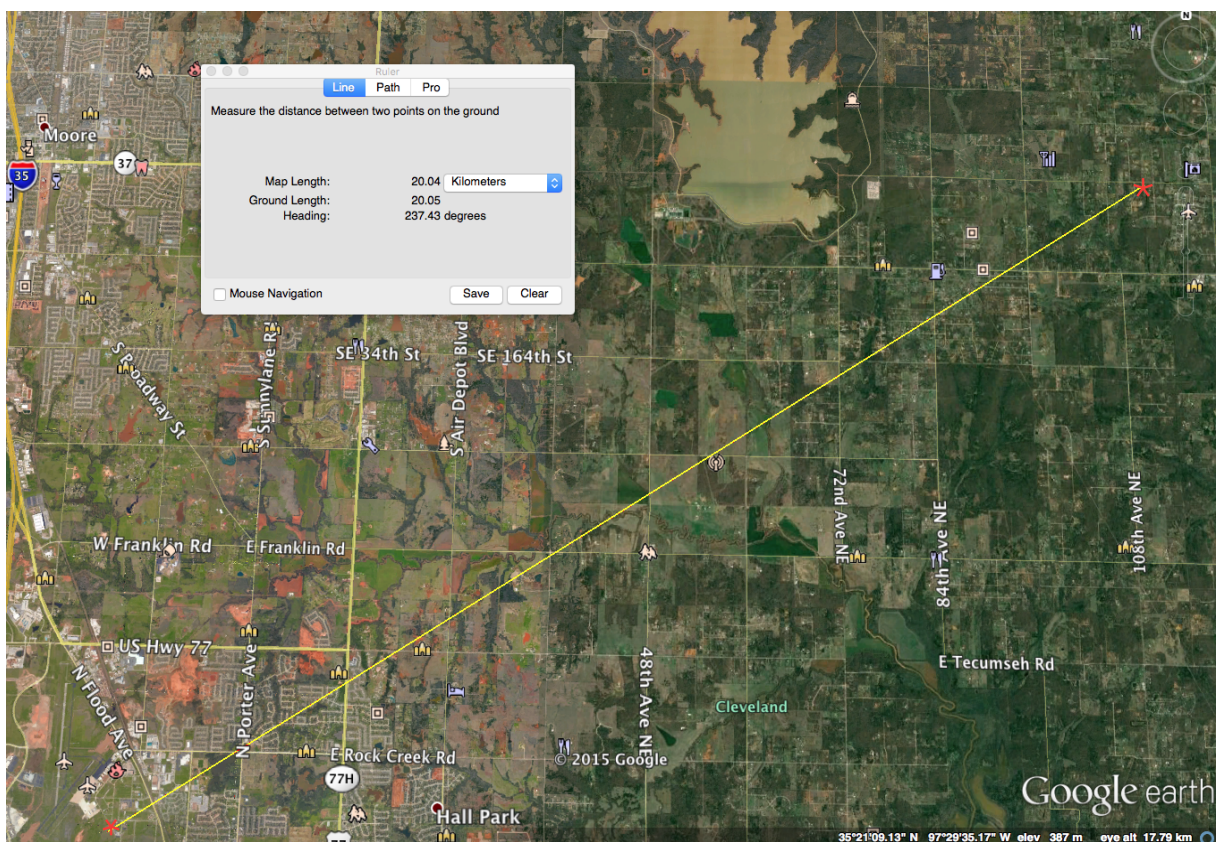


Figure 5.40: Location of the phased array radar (Norman, OK) relatively to the WSR-88D KTLX radar (S.W. of Oklahoma City).

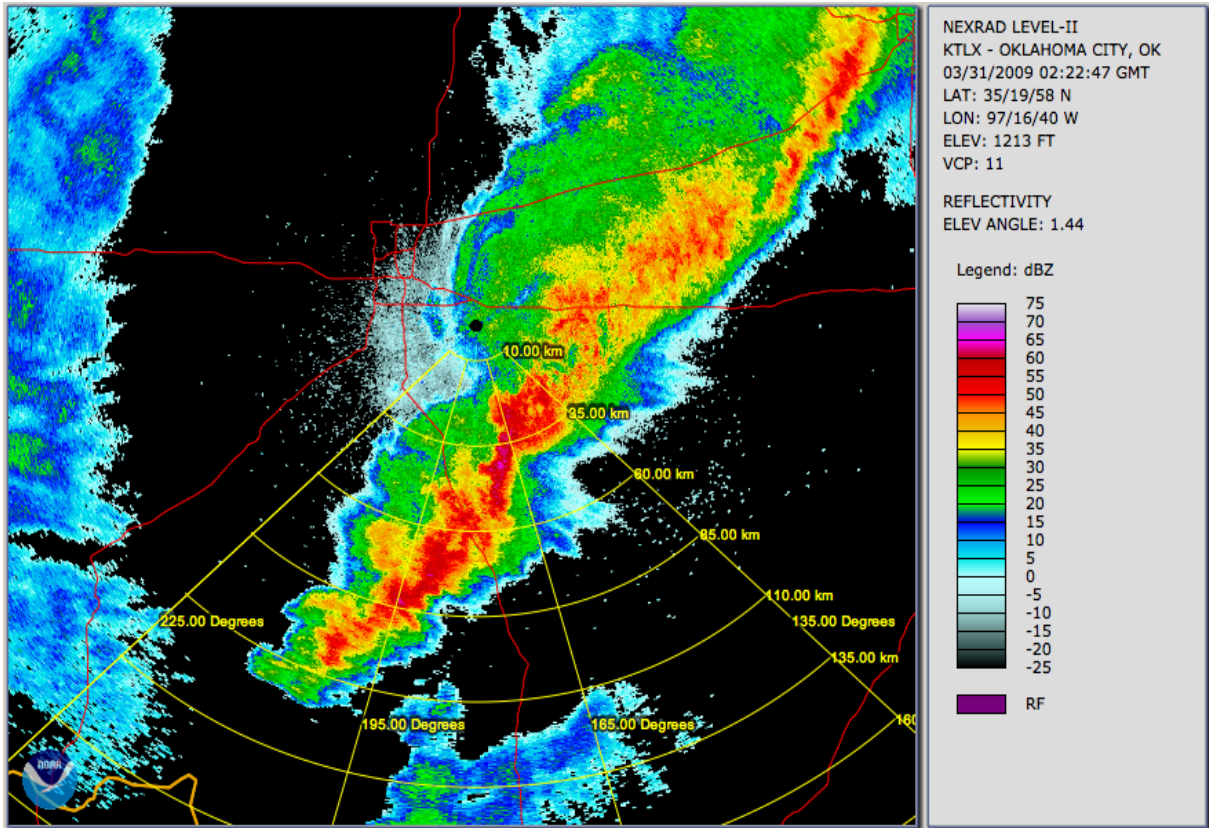


Figure 5.41: View of the same weather perturbation by KTLX radar.

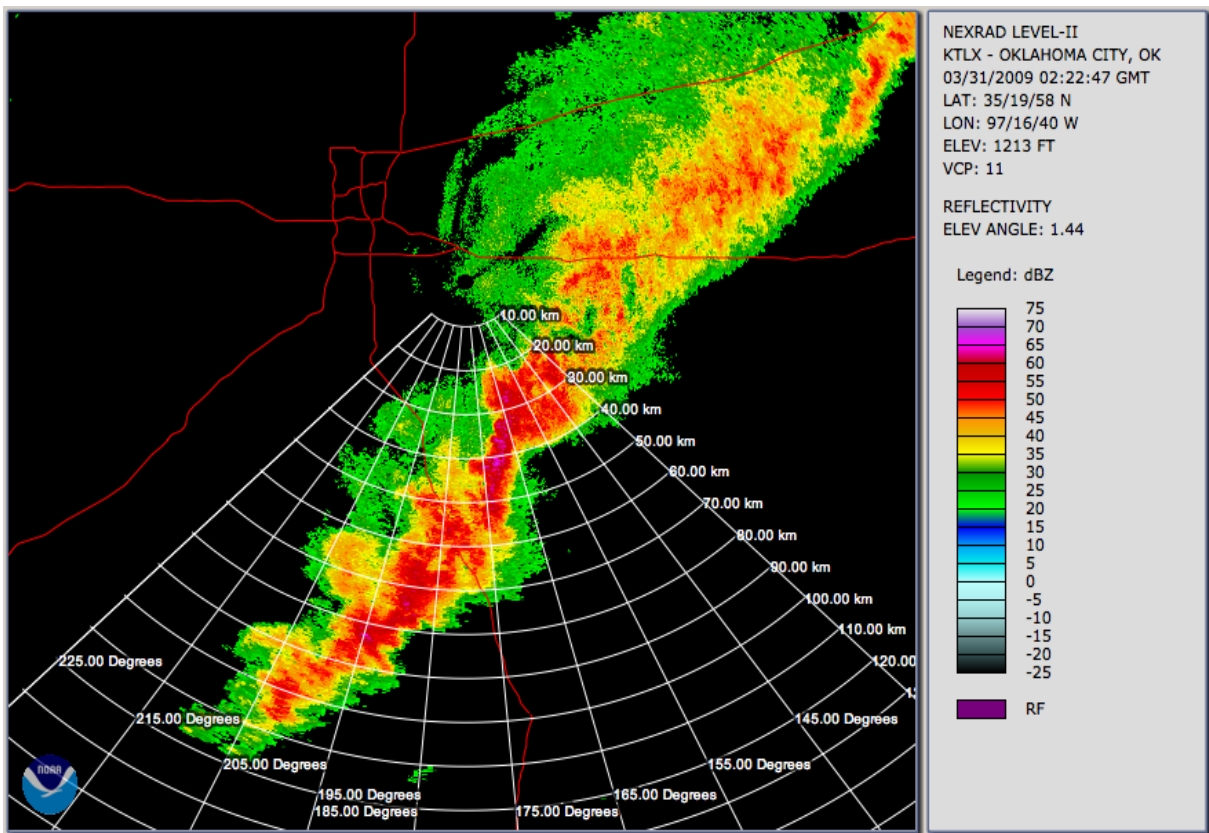


Figure 5.42: Gridded and labeled view of the sector corresponding to the phased array radar sight for the storm.

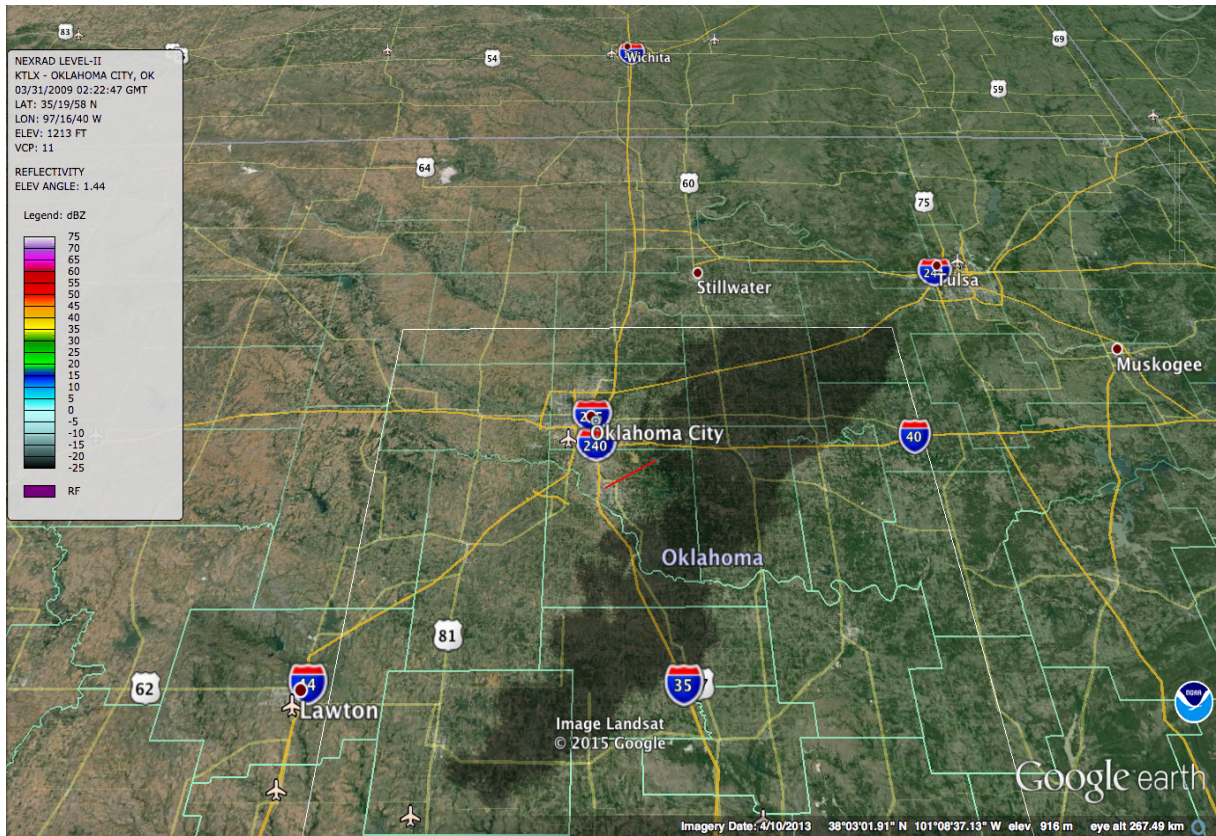


Figure 5.43: Reconstruction of the shade of the storm in conjunction of Google Earth and NOAA Weather and Climate Toolkit.

Chapter 6 : Conclusion and recommendations for future work

6.1. Summary and conclusions

The objective of this work is to estimate the dynamic properties of a weather radar signal using spectral approaches. A number of various methods for spectrum estimation were developed using both simulated and actual data. Parametric and non-parametric procedures are the two major approaches that are assessed and used in many fields, including weather radar domain. Both have advantages and drawbacks. Mainly, parametric methods have a higher complexity and need more computational resources than non-parametric ones. On this aspect, non-parametric approaches are faster than parametric ones.

On the other hand, using parametric methods may help to produce better spectral estimates with lower uncertainty than those obtained with non-parametric procedures.

The ideal approach would be the one that would offer a high accuracy of estimates without being greedy in computational resources.

In this work, an alternative approach is developed and assessed using both synthetic and real data. This approach is based on the synergy of three (03) elements: Periodogram, Lifting Scheme Wavelet Transform and Adaptive Thresholding.

The advantage of periodogram is that it is fast to compute but it lacks of accuracy, which is a serious drawback. This inconvenience is corrected by the use of a Lifted Wavelet Transform (LWT). This latter is enhanced by the use of an adaptive thresholding of wavelet coefficients.

In weather radar applications, the wavelet transform is not very used. It is rather

used in atmospheric radars. The two types of radars operate differently. The major consequence is the large difference between lengths of their respective signals. Atmospheric radar signals (time series) are much longer than weather radar counterparts.

Wavelet transform is much better suited for long signals because many levels can be exploited in search of any remaining noise power in those signals.

Unlike the case of the weather radar signals which are short, wavelet transform can be performed only on very few levels. Consequently, the associated standard thresholds to apply on wavelet coefficients are never efficient to remove all the existing noise as it has been shown by the obtained results.

So the prominent problem of efficiency of wavelet transform performed on weather radar signals is the short length thereof associated with standard thresholds (universal, minimax, SURE, etc.).

Another problem inherent to the use of wavelet transform is the computational burden substantially implied when the involved wavelet is a long filter.

The filter length is paired with the number of vanishing moments of the wavelet. As this number characterizes smoothness, the result of the wavelet transform processing is in turn smooth without sharp edges, provided that the selected wavelet has a high number of vanishing moments.

This complex problem is solved, in this work, by using a LWT associated with a long filter but symmetric (Biorthogonal wavelets). While the length of the filter provides smoothness, symmetry provides half the burden of computations (because we don't need to recalculate symmetric (equal) coefficients).

To enhance the performance of the LWT on Doppler spectrum, the Universal Threshold, which is a very simple and fast to determine is used as a first guess. This type of threshold could be very efficient if weather radar signals were long. This initial value is iteratively incremented while Doppler radial velocity along with spectrum width are recalculated and compared to their corresponding previous values. All the procedure is designed and described.

As long as noise still remains in the Doppler spectrum, both Doppler radial velocity and spectrum width will be biased. The former (i.e, V_D) is underestimated and the latter (i.e, σ_v) is overestimated.

So, while removing an amount of noise after each iteration, the two estimates get closer to their respective true values. The final iteration will be the one where both

Doppler radial velocity and spectrum width don't get enhanced any better. This means that almost all the noise is no longer present in the estimated spectrum.

The necessary number of iterations is noise level dependent. The higher the level of noise is, the higher the necessary number of iterations is. If there is no noise, then there will not be any iteration. This fact is incentive and encouraging to apply the algorithm at all range bins and all elevations because if, at any range bin, there would be no noise then there would be no waste of time upon iterations.

The performance of the algorithm on real data (Figure 5.33 through Figure 5.37) shows that the noise level is not the same everywhere, not even on a same radial. This attests the necessity to estimate noise level at all range bins and elevations in contrast to the fact that it is commonly considered as a constant valued for a whole radar sweep.

The performance of the algorithm on simulated data shows that as of $SNR = 15$ dB, there is no need for any algorithm to improve spectrum estimate.

On the other hand, when SNR is lower than 2 dB, the algorithm is still very efficient, as it is shown on Figure 5.7 through Figure 5.10.

The detection threshold of the U.S Weather Surveillance Radar (WSR-88D) is 2 dB for reflectivity (Z) and 3 dB for Doppler radial velocity (V_D). through the simulated data, the algorithm can extract weather spectrum even at $SNR = -5$ dB.

The selected real data, in this work, are chosen on the basis that they are ground clutter free. This is to show the true performance achieved by the developed algorithm to estimate Doppler spectrum with a high accuracy.

As regards the simulated signals, they not only are ground clutter free but also generated to very unfavorable cases ($SNR = -5$ dB), again to highlight the efficiency reached by the developed technique.

6.2. Recommendation for future work

Logical actions to be taken consequently to this work may be suggested in the following topics for future research:

- To be able to apply the developed algorithm (in this work), without any limiting circumstances like presence of ground clutter, it is recommendable to first remove this latter. So, it is desirable to devise an intelligent technique to carry out the task using wavelet transform. The intelligence refers to the detection capability of presence or absence of ground clutter in the current

range location, followed by the decision whether to apply, or not, the technique to remove it.

- Once all the data are cleaned from all any impurities (noise, ground clutter, etc.), any further processing would be less subject to uncertainties. It is desirable to carry out a thorough study of the most challenging application of weather radars (dual polarized) which is the precipitation estimation in presence of a mixture of hydrometeors according to their respective drop size distributions (DSD), as well as understanding the microphysics of hydrometeors in order to be capable to recognize their corresponding signatures and classify them.

Bibliography

- 1: National Research Council. "Weather Radar Technology beyond NEXRAD". National Academy Press, 2002.
- 2: A.D. Siggia, R.E. Passarelli. "Gaussian Model Adaptive Processing (GMAP) for improved ground clutter cancellation and moment calculation". Proceedings of ERAD, 2004.
- 3: F.J. Yanovsky et al.. "Comparison of Modeled and Measured Doppler-Polarimetric Parameters of Radar Signal Reflected From Rain". Proceedings of ISPAA, 2000.
- 4: F.J. Yanovsky. "Doppler Polarimetric Approach to Microwave Remote Sensing of Precipitation". Symposium Proceedings, 2007.
- 5: F.J. Yanovsky. "Consecutive Description of and Recent Results in the Polarimetric Doppler Weather Radar". International Radar Symposium, 2011.
- 6: S.M. Kay, S.L. Marple. "Spectrum Analysis - A Modern Perspective". Proceedings of the IEEE, 1981.
- 7: A.T. Walden, D.B. Percival & E.J. McCoy. "Spectrum estimation by Wavelet Thresholding of Multitaper Estimators". IEEE Trans. on Signal Processing, 2002.
- 8: Qing Cao et al.. "Spectrum - Time Estimation and Processing (STEP) for improving Weather Radar Quality". IEEE Trans. on Geoscience and Remote Sensing, 2012.
- 9: R.D. Palmer et al.. "Enhanced Autoregressive Moving Average Spectral Estimation Applied to the measurement of Doppler Spectral Width". IEEE Trans. on Geoscience and Remote Sensing, 1991.
- 10: J.M.B. Dias, J.M.N. Leitao. "Nonparametric Estimation of Mean Velocity and Spectral Width in Weather Radar". IEEE, Transactions on Geoscience and Remote Sensing, 1995.
- 11: J.M.B. Dias, J.M.N. Leitao. "Nonparametric Estimation of Mean Doppler and Spectral Width". IEEE, Transactions on Geoscience and Remote Sensing, 2000.
- 12: R. Von Sachs, K. Schneider. "Wavelet Smoothing of Evolutionary Spectra by Nonlinear Thresholding". Applied and computational harmonic analysis, 1996.
- 13: Hong-Ye Gao. "Spectral Density Estimation via Wavelet Shrinkage". Tech. Report, Statistics, Stanford, 1996.
- 14: P. Moulin. "Wavelet Thresholding Techniques for Power Spectrum Estimation". IEEE Trans. on Signal Processing, 1993.
- 15: M. Tikhemirine, M. Lagha, S. Bergheul. "Noise Cancellation in Doppler Moment Estimation of Phased Array Weather Radar Signals Using Biorthogonal Wavelets". Digital Signal Processing,

Elsevier, 2013.

- 16: M. Lagha, M. Tikhemirine, et al. "Denoised Estimation of the Weather Doppler Spectrum by the Wavelet Method". Digital Signal Processing, Elsevier, 2013.
- 17: C. Wang, F. Wang. "Improved Algorithm of Pulse Wave Threshold Denoising Based on Lifting Wavelet Transform". IEEE, 3rd ICBBE, 2009.
- 18: S. Mallat. "A Wavelet Tour of Signal Processing". Academic Press (Elsevier), 2009.
- 19: D.L. Donoho, I.M. Johnstone. "Ideal Spatial Adaptation by Wavelet Shrinkage". Biometrika, 1994.
- 20: D.L. Donoho, I.M. Johnstone. "Minimax Estimation via Wavelet Shrinkage". The Annals of Statistics, 1998.
- 21: DOC, NOAA. "FCM-H11B. Doppler Radar, Meteorological Observations: Doppler Radar Theory and Meteorology. Part B". DOC, NOAA, 2005.
- 22: US Navy. "Environmental Satellites and Weather Radar". US Navy, 1999.
- 23: DOC, NOAA. "FCM-H11B. Doppler Radar, Meteorological Observations: WSR-88D Products and Algorithms. Part C". DOC, NOAA, 2006.
- 24: R.J. Keeler, R.E. Passarelli. "Radar Handbook, Chapter 19: Meteorological Radar, 3rd Edition". Mc Graw Hill, 2008.
- 25: R.J. Keeler, R.E. Passarelli. "Signal Processing for Atmospheric Radars". NCAR Technical Note, 1989.
- 26: R.J. Doviak, D.S. Zrnic. "Doppler Weather Radar". Proceedings of the IEEE, 1979.
- 27: David D. Aalfs, et al. . "Signal Processing Aspects of Wind Shear Detection". Microwave journal, 1993.
- 28: V.N. Bringi, V. Chandrasekar. "Polarimetric Doppler Weather Radar: Principles and Applications". Cambridge University Press, 2005.
- 29: D.S. Zrnic, A.V. Ryzkhov. "Polarimetry for Weather Surveillance Radars". Bulletin of the American Meteorological Society, 1998.
- 30: R.J. Doviak, D.S. Zrnic. "Doppler Radar and Weather Observations". Dover Publications; 2nd Edition, 2006.
- 31: V.M. Melnikov, D.S. Zrnic. "Simultaneous Transmission Mode for the Polarimetric WSR-88D". Report of CIMMS, University of Oklahoma, 2004.
- 32: V.M. Melnikov, I. Ivic, D.S. Zrnic. "Processing to Obtain Polarimetric Variables on the ORDA". Report of CIMMS, University of Oklahoma, 2008.
- 33: G. Meymaris, J.K. Williams. "Spectrum Width Estimators for the NEXRAD ORDA: Evaluation and Recommendation". Journal of American Meteorological Society, 2007.
- 34: D.S. Zrnic. "Estimation of Spectral Moments for Weather Echoes". IEEE Trans. on Geoscience Electronics, 1979.
- 35: V.M. Melnikov, D.S. Zrnic. "Autocorrelation and Cross-Correlation Estimators of Polarimetric Variables". Journal of American Meteorological Society, 2006.
- 36: V. K. Madisetti, . "The Digital Signal Processing Handbook". CRC Press; 2nd Edition, 2010.
- 37: David D. Aalf, et al. . "Signal Processing Aspects of Wind Shear Detection". Microwave journal, 1993.
- 38: J.M.B. Dias, J.M.N. Leitao. "Nonparametric Estimation of Mean Doppler and Spectral Width". IEEE, Transactions on Geoscience and Remote Sensing, 2000.
- 39: J.A. Cadzow. "High Performance Spectral Estimation - A New ARMA Method.". IEEE Trans. on

Acoustics, Speech and S.P., 1980.

- 40: B. W. Keel. "Adaptive clutter rejection filters for airborne Doppler weather radar applied to the detection of low altitude windshear". NASA Technical report #11, 1989.
- 41: S. M. Kay and S. L. Marple. "Spectrum Analysis—A Modern Perspective". Proceedings of IEEE, 1981.
- 42: J. Durbin. "The Fitting of Time-Series Models". International Stat. Institute, 1960.
- 43: G. Cybenko. "Round-off error propagation in Durbin's, Levinson's, and Trench's algorithms". IEEE International Conference on ICASSP '79, 1979.
- 44: J. P. Burg. "Maximum Entropy Spectral Analysis". Ph.D. Thesis of University of Stanford, 1975.
- 45: H. Akaike. "Fitting Autoregressive Models for Prediction". Annals of the Institute of Statistical Mathematics, 1969.
- 46: H. Akaike. "A New Look at the Statistical Model Identification". IEEE Trans. on Automatic Control, 1974.
- 47: E. Parzen. "Some Recent Advances in Time Series Modeling". IEEE Trans. on Automatic Control, 1974.
- 48: P.T. Hildebrand, R.S. Sekhon. "Objective Determination of the Noise Level in Doppler Spectra ". Journal of Applied Meteorology, 1974.
- 49: H. Urkowitz, J.D. Nesper. "Obtaining Spectral Moments by Discrete Fourier Transform with Noise Removal in Radar Meteorology". IEEE, 1992.
- 50: I.R. Ivic, S.M. Torres. "Online Determination of Noise Level in Weather Radars". ERAD, 2010.
- 51: W. Sweldens, P. Schroder. "Building Your Own Wavelets at Home". Springer, 2000.
- 52: W. Sweldens. "The Lifting Scheme: A Construction of Second Generation Wavelets". SIAM, 1998.
- 53: W. Sweldens. "The Lifting Scheme: A Custom-Design Construction of Biorthogonal Wavelets". Elsevier, 1996.
- 54: I. Daubechies, W. Sweldens. "Factoring Wavelet Transforms into Lifting Steps". Springer, 1998.
- 55: A. Jensen, A. la Cour-Harbo. "Ripples in Mathematics: The Discrete Wavelet Transform". Springer-Verlag, 2001.
- 56: I. Daubechies. "Orthonormal Bases of Compactly Supported Wavelets". Comm. Pure Appl. Math., 1988.
- 57: D.L. Donoho, I.M. Johnstone. "Adapting to Unknown Smoothness Via Wavelet Shrinkage". Journal of the American Statistical Association, 1995.
- 58: D.S. Zrnica. "Simulation of Weather-Like Doppler Spectra and Signals". Journal of American Meteorological Society, 1975.

Appendix A:

Factorizing of the biorthogonal wavelet filter pair that has been used in this work

The biorthogonal wavelet that has been selected in this thesis is the well known 9/7 filter pair. It is used in several domains because it is very effective.

The reason it is called that way is that the analysis filter \tilde{h} has 9 coefficients, while the synthesis filter h has only 7 coefficients. The corresponding number of vanishing moments of the two involved wavelets (g and \tilde{g}) are four (4).

The achievement of a transform through this biorthogonal wavelet needs two wavelets (one for analysis and the other for reconstruction) and two corresponding scaling functions (again, one for analysis and the other for reconstruction). These four elements are considered as FIR filters and their corresponding equations are as follows:

Analysis low pass filter (Decomposition scaling function):

$$\tilde{h}(z) = \tilde{h}_4(z^4 + z^{-4}) + \tilde{h}_3(z^3 + z^{-3}) + \tilde{h}_2(z^2 + z^{-2}) + \tilde{h}_1(z+1) + \tilde{h}_0$$

Analysis high pass filter (Decomposition wavelet):

$$\tilde{g}(z) = \tilde{g}_3(z^3 + z^{-3}) + \tilde{g}_2(z^2 + z^{-2}) + \tilde{g}_1(z+1) + \tilde{g}_0$$

Reconstruction low pass filter (Reconstruction scaling function):

$$h(z) = h_3(z^3 + z^{-3}) + h_2(z^2 + z^{-2}) + h_1(z+1) + h_0$$

Reconstruction high pass filter (Reconstruction wavelet):

$$g(z) = g_4(z^4 + z^{-4}) + g_3(z^3 + z^{-3}) + g_2(z^2 + z^{-2}) + g_1(z+1) + g_0$$

where the coefficients values are as follows:

$$h_0 = 0.788485616614, \quad h_1 = 0.418092273333, \\ h_2 = -0.040689417620, \quad h_3 = -0.064538882646$$

$$g_0 = 0.852698679009, \quad g_1 = -0.377402855613, \quad g_2 = -0.110624404418, \\ g_3 = 0.023849465019, \quad g_4 = 0.037828455507$$

$$\tilde{h}_0 = g_0, \quad \tilde{h}_1 = -g_1, \quad \tilde{h}_2 = g_2, \quad \tilde{h}_3 = -g_3, \quad \tilde{h}_4 = g_4 \\ \tilde{g}_0 = h_0, \quad \tilde{g}_1 = -h_1, \quad \tilde{g}_2 = h_2, \quad \tilde{g}_3 = -h_3.$$

Curves of this biorthogonal wavelet are depicted in Figure 6.1 where analysis/synthesis wavelets along with scaling functions and their corresponding filters are represented.

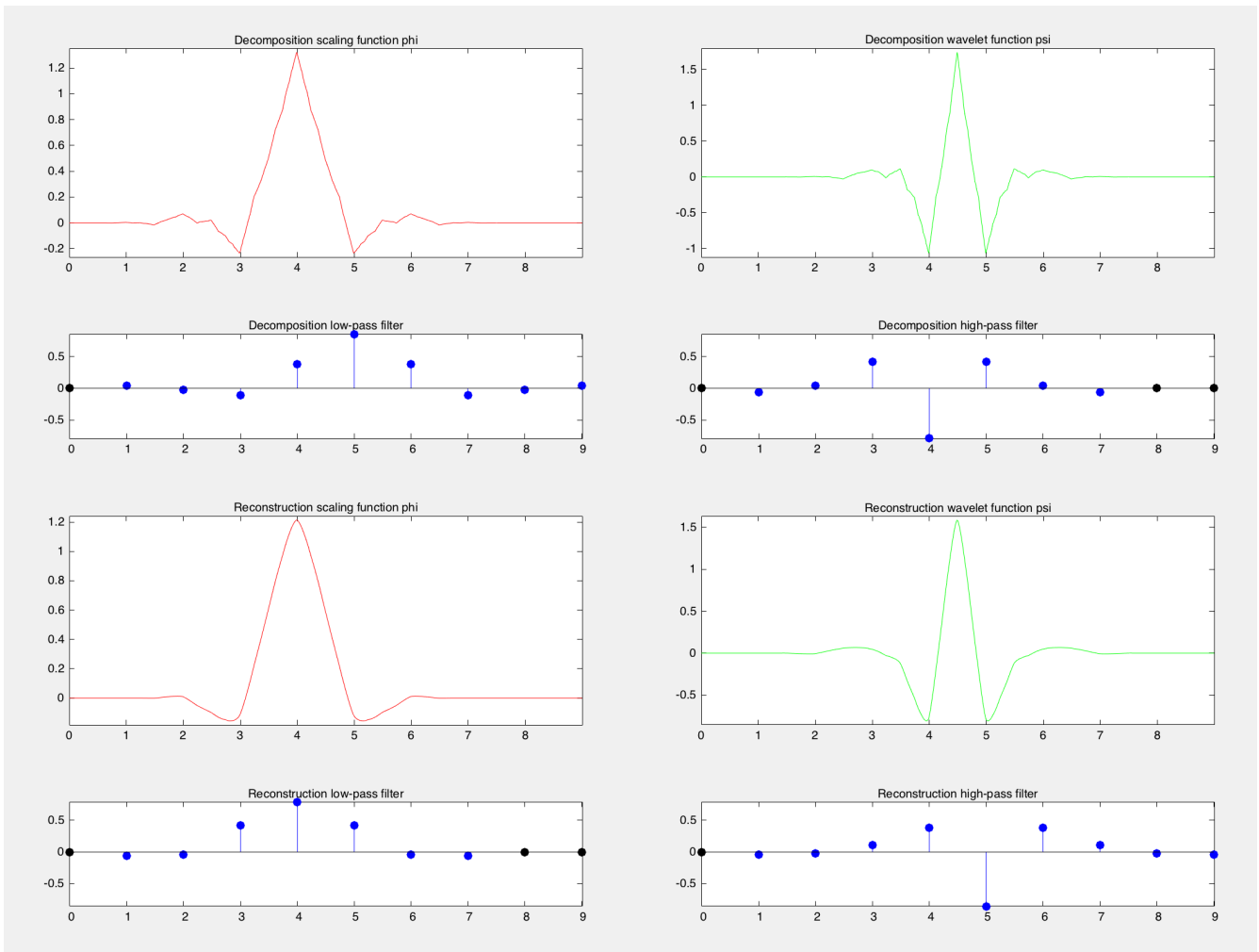


Figure 6.1: Biorthogonal 9/7 wavelet: Decomposition wavelet and its scaling function and their corresponding filters (Top). Reconstruction wavelet and its scaling function and their corresponding filters (Bottom).

Factorization of the filters

The analysis filter $\tilde{h}(z)$ will be decomposed into two filters (even part and odd part).

$$\begin{aligned}\tilde{h}(z) &= \tilde{h}_4(z^4+z^{-4})+\tilde{h}_3(z^3+z^{-3})+\tilde{h}_2(z^2+z^{-2})+\tilde{h}_1(z+1)+\tilde{h}_0 \\ &= \tilde{h}_e(z)+z^{-1}\tilde{h}_o(z)\end{aligned}$$

The even polynomial and the odd polynomial are derived as follows:

$$\begin{aligned}\tilde{h}_e(z) &= \sum_k \tilde{h}_{2k} z^{-k} && \text{for the even part, and} \\ &= \tilde{h}_4(z^2+z^{-2})+\tilde{h}_2(z+z^{-1})+\tilde{h}_0\end{aligned}$$

$$\begin{aligned}\tilde{h}_o(z) &= \sum_k \tilde{h}_{2k+1} z^{-k} && \text{for the odd part.} \\ &= \tilde{h}_3(z+z^{-1})+\tilde{h}_1(z+1)\end{aligned}$$

As regards to the analysis wavelet filter

$\tilde{g}(z) = \tilde{g}_3(z^3+z^{-3}) + \tilde{g}_2(z^2+z^{-2}) + \tilde{g}_1(z+1) + \tilde{g}_0$, it will be decomposed into the two following filters (even part and odd part).

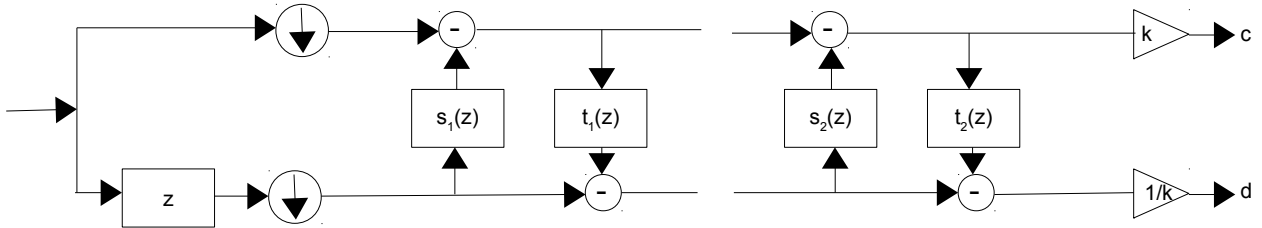
$$\tilde{g}_e(z)=\tilde{h}_2(z+z^{-1})+\tilde{h}_o \text{ for the even part, and}$$

$$\tilde{g}_o(z)=-\tilde{h}_3(z^2+z^{-2})-\tilde{h}_1(z+1) \text{ for the odd part.}$$

From these equations, a polyphase matrix is derived as follows:

$$\tilde{P}(z) = \begin{pmatrix} \tilde{h}_e(z) & \tilde{g}_e(z) \\ \tilde{h}_o(z) & \tilde{g}_o(z) \end{pmatrix} = \prod_{i=1}^m \begin{pmatrix} 1 & 0 \\ -s_i(z^{-1}) & 1 \end{pmatrix} \begin{pmatrix} 1 & -t_i(z^{-1}) \\ 0 & 1 \end{pmatrix} \begin{pmatrix} k & 0 \\ 0 & 1/k \end{pmatrix}$$

where $s_i(z^{-1})$ are the lifting polynomials of the low pass sub-band with the help of the high pass sub-band and $t_i(z^{-1})$ are the lifting polynomials of the high pass sub-band with the help of the low pass sub-band.



The polynomials are as follows:

$$s_1(z)=\alpha_1(1+z^{-1}) \quad t_1(z)=\beta_1(1+z^{-1})$$

$$s_2(z)=\alpha_2(1+z^{-1}) \quad t_2(z)=\beta_2(1+z^{-1})$$

where $\alpha_1=-1.586134342060$, $\beta_1=-0.052980118573$,
 $\alpha_2=0.882911075531$, $\beta_2=0.443506852044$,
 $k=1.149604398860$.

Implementation of the biorthogonal wavelet transform 9/7

If S is the input signal of the wavelet transform, then the equations involved would yield the following implementation.

$$d^{(1)}[n] = S[2n+1] + \alpha S[2n] + \alpha S[2n+2]$$

$$c^{(1)}[n] = S[2n] + \beta d^{(1)}[n] + \beta d^{(1)}[n-1]$$

$$d^{(2)}[n] = d^{(1)}[n] + \alpha_2 c^{(1)}[n] + \alpha_2 c^{(1)}[n+1]$$

$$c^{(2)}[n] = c^{(1)}[n] + \beta_2 d^{(2)}[n] + \beta_2 d^{(2)}[n-1]$$

$$c = k c^{(2)}[n]$$

$$d = d^{(2)}[n]/k$$

The inverse wavelet transform implementation will be as follows:

$$d^{(2)}[n] = d \cdot k$$

$$c^{(2)}[n] = c/k$$

$$c^{(1)}[n] = c^{(2)}[n] - \beta_2 (d^{(2)}[n] + d^{(2)}[n-1])$$

$$d^{(1)}[n] = d^{(2)}[n] - \alpha_1 (c^{(1)}[n] + c^{(1)}[n+1])$$

$$S[2n] = c^{(1)}[n] - \beta_1 (d^{(1)}[n] + d^{(1)}[n-1])$$

$$S[2n+1] = d^{(1)}[n] - \alpha_1 (S[2n+1] + S[2n+2])$$

Appendix B:

Generation of weather-like Doppler radar signals

It is a prominent task to compare, under controlled conditions, the performance of various Doppler radar signal processing techniques. Zrnic [58] presented a method that generates directly an arbitrarily shaped power spectrum with the essential weather-like signal properties.

Some hypotheses have to be taken into account:

- Weather echo spectrum is narrow-band, unlike noise spectrum that is broadband.
- Weather signal power is larger than noise power.
- Weather echo and receiver noise have almost similar statistical properties.

For a given range bin, the i th sample in-phase I and quadrature-phase Q components can be written as

$$\begin{cases} I(i) = s(i)\cos(\phi(i)) + n(i)\cos(\phi(i)) \\ Q(i) = s(i)\sin(\psi(i)) + n(i)\sin(\psi(i)) \end{cases}$$

where:

$s(i)$: weather signal envelope

$\phi(i)$: uniformly distributed phase of $s(i)$

$n(i)$: radar noise

$\psi(i)$: uniformly distributed phase of $n(i)$

This pair of equations can be written as follow

$$I(i)+jQ(i) = \frac{1}{n} \sum_{k=1}^n P_k e^{j\theta_k} e^{(-j\frac{2\pi}{n}ki)}$$

where P_k is the exponentially distributed instantaneous power of the signal plus noise, and θ_k is a uniformly distributed phase.

Let X_k be a uniform random variable between 0 and 1. The basic probability law relates X_k and P_k through

$$P(P_k)dP_k = P_x(X_k)dX_k$$

Integrating both sides of the equation between 0 and P_k in the left side and between 0 and X_k in the right side, the resulting equation relating the power of the total signal P_k and the random variable X_k is, after simplification,

$$P_k = -(S_k+N)\log(X_k)$$

The probability density of p_k can be written as

$$P(P_k) = \frac{1}{S_k+N} e^{-\frac{P_k}{S_k+N}}$$

The steps of the implemented algorithm are:

1. Generate a power spectrum of signal with an arbitrarily shaped S_k
2. Choose the noise power N so as to have a signal to noise ratio as follow

$$SNR = \frac{signal}{noise} = \frac{1}{nN} \sum_{k=1}^n S_k$$

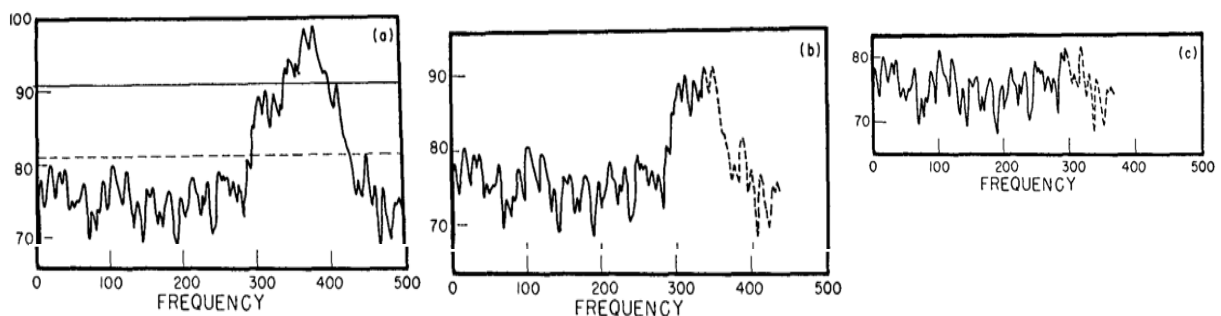
3. The signal and noise powers are added, at each frequency, and multiplied with the logarithm of a uniformly distributed random number X_k to generate a desired power spectral component P_k .

Appendix C:

Determination of the noise level from a Doppler radar spectrum by Hildebrand & Sekhon

The importance of identifying the noise threshold may be seen from computation of the variance of the Doppler spectrum. The computed Doppler spectrum variance can be seriously affected by noise, if the signal to noise ratio is low. To avoid this problem, spectral lines due to radar system noise should be removed from the variance computation.

The signals due to weather and to radar system noise are both Gaussian. Where the former has a colored spectrum and the latter has a white one. The following figure (left part) depicts a typical spectrum of a combined signal (weather + noise).



From this spectrum, we construct a new spectrum by rejecting spectral densities

stronger than an arbitrarily assigned threshold (central part of the figure), and by forming a continuous spectrum out of the remaining parts of the spectrum.

For a given spectrum, we can apply a series of decreasing thresholds until the constructed spectrum satisfies the conditions of white noise. This particular threshold would, then, be the noise threshold.

In order to test for white noise, the following parameters are calculated:

$$\sigma^2 = \frac{\sum f_n^2 S_n}{\sum S_n} - \left(\frac{\sum f_n S_n}{\sum S_n} \right)^2$$

$$\sigma_N^2 = \frac{F^2}{12}$$

$$P = \frac{\sum S_n}{N}$$

$$Q = \sum \left(\frac{S_n^2}{N} \right) - P^2$$

$$R_1 = \frac{\sigma_N^2}{\sigma^2}$$

$$R_2 = \frac{P^2}{Q}$$

F is the frequency spread of the spectrum, N is the number of spectral densities, p is the number of lines over which a moving average is taken.

For white noise, the ratios R_1 and R_2 should be equal to one.